

SYNTHESIS AND CHARACTERIZATION OF MAGNESIUM
TETRABORATE-BASED MULTIFUNCTIONAL FLAME RETARDANTS AND
THEIR APPLICATION FOR FLAME RETARDANCY OF POLYURETHANE

A THESIS SUBMITTED TO
THE GRADUATE SCHOOL OF NATURAL AND APPLIED SCIENCES
OF
MIDDLE EAST TECHNICAL UNIVERSITY

BY
MUZAFFER GENÇAY ÇELİK

IN PARTIAL FULFILLMENT OF THE REQUIREMENTS
FOR
THE DEGREE OF DOCTOR OF PHILOSOPHY
IN
CHEMISTRY

MARCH 2024

Approval of the thesis:

**SYNTHESIS AND CHARACTERIZATION OF MAGNESIUM
TETRABORATE-BASED COMPOSITES AND THEIR APPLICATION
FOR FLAME RETARDANCY OF POLYURETHANE**

submitted by **MUZAFFER GENÇAY ÇELİK** in partial fulfillment of the requirements for the degree of **Doctor of Philosophy in Chemistry, Middle East Technical University** by,

Prof. Dr. Naci Emre Altun
Dean, Graduate School of **Natural and Applied Sciences** _____

Prof. Dr. Ali Çırpan
Head of the Department, **Chemistry** _____

Prof. Dr. Ayşen Yılmaz
Supervisor, **Chemistry, METU** _____

Examining Committee Members:

Prof. Dr. Okan Esentürk
Chemistry, METU _____

Prof. Dr. Ayşen Yılmaz
Chemistry, METU _____

Prof. Dr. Mehmet Doğan
Textile Engineering, Erciyes University _____

Prof. Dr. Emren Nalbant
Chemistry, METU _____

Assoc. Prof. Ümit Tayfun
Department of Basic Sciences, Bartın University _____

Date: 04.03.2024

I hereby declare that all information in this document has been obtained and presented in accordance with academic rules and ethical conduct. I also declare that, as required by these rules and conduct, I have fully cited and referenced all material and results that are not original to this work.

Name Last name: Muzaffer Gençay Çelik

Signature:

ABSTRACT

SYNTHESIS AND CHARACTERIZATION OF MAGNESIUM TETRABORATE-BASED COMPOSITES AND THEIR APPLICATION FOR FLAME RETARDANCY OF POLYURETHANE

Çelik, Muzaffer Gençay
Doctor of Philosophy, Chemistry
Supervisor: Prof. Dr. Ayşen Yılmaz

March 2024, 171 pages

Boron compounds have low toxicity and diverse molecular structures, making them effective flame-retardant additives in polymer-based materials with various mechanisms of action. These additives are used alone or in combination with mineral fillers, intumescent systems, phosphorus, halogen, nitrogen, silicon, and carbon-containing additives. In this research, four different boron-containing materials such as magnesium tetraborate (MTB), magnesium tetraborate-hydroxyapatite core/shell (MTB@HAp), and melamine formaldehyde (MF) resin-encapsulated MTB and MF encapsulated MTB@HAp, used to improve the flame retardancy of polyurethane (PU). MTB is synthesized using the solid-state synthesis method. HAp coated MTB is prepared using the wet precipitation method. To enhance the flame retardancy performance of MTB, a combination of boron-based and nitrogen-based compounds, such as MF, can provide synergy. The novel MF microcapsulated MTB-MF and MTB@HAp with a double shell are prepared by in situ polymerization. The synthesized MTB-based materials are characterized by X-Ray Diffraction (XRD), Fourier Transform Infrared spectroscopy (FTIR), Thermogravimetric Analysis (TGA), and Differential Scanning Calorimeter (DSC). Polyurethane composites

containing MTB, MTB@HAp, MTB-MF, and MTB@HAp-MF with varying amounts were produced by isocyanate and polyether polyol reaction. The flame-retardant action of MTB, MTB@HAp, MTB-MF, and MTB@HAp-MF in PU are studied using Limiting Oxygen Index (LOI) and standard test method for measuring the comparative burning characteristics of solid plastics in a vertical position (UL-94V), Mass Loss Calorimeter (MLC) and TGA. In addition, the thermal behaviors of PU composites are characterized by TGA and TGA coupled FTIR and the morphologies of residues are investigated with Scanning Electron Microscopy (SEM). Results show that 10PHR-MTB and 15PHR-MTB@HAp core shell containing PU composites achieved 25% and 26.5% LOI values with V-2 of UL-94 rating, respectively. Besides, the peak Heat Release Rate of 10PHR-MTB and 15PHR-MTB@HAp containing PU composites were reduced by 28% and 20% with respect to the PHRR of neat PU. 5PHR-MTB-MF microcapsule (the mass ratio of MTB:MF-1:3) achieved the maximal LOI value of 27%, V-0 of UL-94 rating, and significantly decreased the peak heat release rate from 350 kW/m² to 70 kW/m² with respect to pure PU. The present work demonstrates MF microcapsules prepared with efficiency exhibit remarkable flame retardancy, making them a promising multifunctional composite for usage as a flame retardant in polyurethane applications.

Keywords: Thermoset Polyurethane Flame Retardancy, Magnesium Tetraborate, Melamine Formaldehyde Resin Microencapsulation, Magnesium Tetraborate Hydroxyapatite Core Shell, Flame Retardancy Mechanism.

ÖZ

MAGNEZYUM TETRABORAT BAZLI KOMPOZİTLERİN SENTEZİ, KARAKTERİZASYONU VE POLİÜRETAN ALEV GECİKTİRİCİLİĞİ İÇİN UYGULAMASI

Çelik, Muzaffer Gençay
Doktora, Kimya
Tez Yöneticisi: Prof. Dr. Ayşen Yılmaz

Mart 2024, 171 sayfa

Bor bileşikleri düşük toksisiteye ve farklı moleküler yapılara sahiptir, bu da onları çeşitli etki mekanizmalarına sahip polimer bazlı malzemelerde etkili alev geciktirici katkı maddeleri haline getirir. Bu katkı maddeleri tek başına veya mineral dolgular, şişen sistemler, fosfor, halojen, azot, silikon ve karbon içeren katkı maddeleri ile kombinasyon halinde kullanılmaktadır. Bu çalışmada Poliüretanın alev geciktiriciliğini arttırmak için magnezyum tetraborat (MTB), magnezyum tetraborat-hidroksiapatit (MTB@HAp) çekirdek/kabuk yapısı, melamin formaldehit (MF) reçine kapsüllü MTB ve MF kapsüllü MTB@HAp olmak üzere bor içeren dört farklı malzeme sentezlenmiştir. MTB, katı hal sentez yöntemi kullanılarak sentezlenmiş olup, HAp kabuğu ile kaplı MTB, çökeltme yöntemi kullanılarak hazırlanmıştır. MTB'nin alev geciktirme performansını arttırmak için, MF gibi azot içeren ve bileşiklerin bir kombinasyonu ile sinerji sağlanabilmektedir. MTB-MF ve çift kabuklu yeni MF mikrokapsüllü MTB@HAp, polimerizasyon yoluyla hazırlanmıştır. Sentezlenen MTB bazlı malzemeler, x-ışını kırınımı (XRD), fourier dönüşümü kızılötesi spektroskopisi (FTIR), termogravimetrik analiz (TGA) ve diferansiyel taramalı kalorimetre (DSC) ile karakterize edilmiştir. İzosiyanat ve

polieter polyol reaksiyonu ile farklı miktarlarda MTB, MTB@HAp, MTB-MF ve MTB@HAp-MF içeren poliüretan kompozitler üretilmiştir. PU'da MTB, MTB@HAp, MTB-MF ve MTB@HAp-MF'nin alev geciktirici etkisi, sınırlayıcı oksijen indeksi (LOI) ve katı plastiklerin dikey yanma testi (UL-94V), kütle kaybı kalorimetresi (MLC), termogravimetrik analiz (TGA) kullanılarak incelenmiştir. Ayrıca PU kompozitlerin termal davranışları ve kalıntıların morfolojileri TGA-FTIR ve taramalı elektron mikroskop (SEM) ile karakterize edilmiştir. Sonuçlar, PU kompozitleri içeren 10PHR-MTB ve 15PHR-MTB@HAp çekirdek kabuğunun, UL-94 derecesine ait V-2 ile sırasıyla %25 ve %26,5 LOI değerlerine ulaştığını göstermektedir. Ayrıca 10PHR-MTB ve 15PHR-MTB@HAp içeren PU kompozitlerin en yüksek Isı Yayılım Hızı (pHRR), saf PU'nun pHRR'sine göre %28 ve %20 oranında azaldığı görülmüştür. 5PHR MTB-MF mikrokapsülü (MTB'nin kütle oranı: MF=1:3), %27'lik maksimum LOI değerini, UL-94 derecelendirmesinin V-0'ını elde ederken ve tepe ısı salınım oranını saf PU'a göre 350 kW/m²'den önemli ölçüde düşürerek 70 kW/m²'ye kadar inmiştir. Mevcut çalışma, hazırlanan MF mikrokapsüllerinin dikkate değer bir alev geciktirici özelliği sergilediğini, bu da onları poliüretan uygulamalarında alev geciktirici olarak kullanım için umut verici çok işlevli bir kompozit haline getirdiğini göstermektedir.

Anahtar Kelimeler: Termoset Poliüretan Alev Geciktirme, Magnezyum Tetraborat, Melamin Formaldehit Reçine Mikrokapsülasyon, Magnezyum Tetraborat Hidroksiapatit Çekirdek Kabuk, Alev Geciktirme Mekanizması.

To My Mother Zehra and Father Faruk,
and My Beloved Wife Begüm

ACKNOWLEDGMENTS

First and foremost, I wish to express my deepest gratitude to my supervisor Prof. Dr. Ayşen Yılmaz for patience, guidance, advice, criticism, encouragements, and insight throughout the research.

Besides my advisor, I would like to thank the rest of my thesis committee: Prof. Dr. Okan Esentürk, and Prof. Dr. Mehmet Doğan for their encouragement, insightful comments, and hard questions through these years.

A very special thanks to Prof. Dr. Mehmet Doğan and Assoc. Dr. Ümit Tayfun for helping to meticulously check my work, pointing out new directions for research and guiding me to a stronger conclusion.

I am thankful to all Ayşen Yılmaz Research Group members, old and new.

I would like to thank my friends Hakan Ünay, Özde Ceren Hızal, Yusuf Samet Aytekin, Perihan Öztürk, Dilara Gündoğdu, Emre Ataoğlu and Nurzhan Beksultanova for all their help and solidarity.

I am grateful to ROKETSAN for providing me with the opportunity to conduct part of my research in the facility and for all the resources and support. I would like to extend a special thanks to Dr. Başak Yiğitsoy Kamışlı who supports me to finish my study.

I also express my sincere appreciation to all the members of Roketsan Propellant Technologies Department for their friendship. Special thanks go to my friend, Ali Sait Güllü for his solidarity and friendship in my absence from the office.

I would like to express my gratitude to TÜBİTAK (120Z954) for financial support. I also would like to thank İrfan Selim Bozdoğan for assistance in SEM experiments and Deniz Demirkıran for assistance in TGA-FTIR experiments. Also, I am thankful to Prof. Dr. Özdemir Doğan for Conic Calorimeter experiments.

Lastly, I want to express my deepest gratitude to my wife. Thank you for always being my inspiration, accompanying me through the highs and lows of this academic journey. Her support and belief in me have been a source of strength and motivation.

TABLE OF CONTENTS

ABSTRACT	v
ÖZ.....	vii
ACKNOWLEDGMENTS	x
TABLE OF CONTENTS	xii
LIST OF TABLES	xvi
LIST OF FIGURES	xvii
LIST OF ABBREVIATIONS	xxii
CHAPTERS	
1 INTRODUCTION	1
1.1 Polyurethane Types and Synthesis Methods	1
1.2 Polyurethanes as Technological Material	4
1.2.1 Polyurethanes in Solid Propellant Rocket Technology	4
1.3 Flammability of PUs	7
1.4 Thermal Stability of PUs	8
1.4.1 Thermal Degradation Process of PUs.....	9
1.5 Flame Retardancy of Polymers.....	11
1.5.1 Mechanisms of Action of Flame Retardants	12
1.5.2 Classification of Flame Retardants.....	17
1.6 Standard Fire Tests to Understand Thermal Degradation Mechanism.....	34
1.6.1 TGA, Pyrolysis–GC/MS, TGA-MS and TGA-FTIR analysis	34

1.6.2	Cone Calorimetry	35
1.6.3	Limiting oxygen index (LOI).....	37
1.6.4	Standard Test Method for Measuring the Comparative Burning Characteristics of Solid Plastics in a Vertical Position (UL-94 V).....	39
2	AIM OF THE STUDY.....	41
3	MATERIALS AND METHODS.....	45
3.1	Materials and Chemicals	45
3.2	Equipment and Characterization Methods	46
3.2.1	Powder X-Ray Diffractometer (XRD).....	46
3.2.2	Fourier Transform Infrared Spectrometer (FT-IR)	46
3.2.3	Furnace.....	47
3.2.4	Simultaneous Thermal Analyzer (STA:TGA+DSC).....	47
3.2.5	Thermogravimetric Analysis (TGA) coupled with FTIR	47
3.2.6	Scanning Electron Microscopy (SEM)	47
3.2.7	Transmission Electron Microscopy (TEM)	48
3.2.8	Conic Calorimeter (CC).....	48
3.2.9	Standard Test Method for Measuring the Minimum Oxygen Concentration to Support Candle-Like Combustion of Plastics, Limiting Oxygen Index (LOI)	49
3.2.10	Standard Test Method for Measuring the Comparative Burning Characteristics of Solid Plastics in a Vertical Position (UL-94 V).....	50
3.3	Experimental	51
3.3.1	Synthesis of Magnesium Tetraborate, (MTB)	51
3.3.2	Synthesis of Magnesium Tetraborate as Core, Hydroxyapatite as Shell Structure (Inorganic-Inorganic Core Shell Model).....	52

3.3.3	Microencapsulation of MTB and MTB/HAp Core Shell	52
3.3.4	Preparation of Flame Retarded Thermoplastic Polyurethane Composites	55
4	RESULTS AND DISCUSSION.....	59
4.1	Characterization of Synthesized Flame Retardants	59
4.1.1	X-Ray Diffraction Analysis.....	59
4.1.2	FTIR Analysis	63
4.1.3	Scanning Electron Microscopy (SEM)-Energy Dispersive X-Ray Spectroscopy (EDS) Analysis	67
4.1.4	Transmission Electron Microscopy (TEM) Analysis.....	72
4.1.5	Thermal Analysis of Synthesized Flame Retardants.....	75
4.1.6	TGA-FTIR Analyses of MF Resin	84
4.2	Characterization of Flame Retardancy Properties of PU Composites	85
4.2.1	TGA and TGA-FTIR Analyses of PU Composites.....	85
4.2.2	LOI and UL-94 Analyses of PU Composites	111
4.2.3	Cone Calorimeter Analyses of PU Composites.....	117
4.3	Flame Retardant Mechanisms of PU Composites.	140
4.3.1	Non-Oxidative Thermal Degradation Mechanism of Neat PU	140
4.3.2	Proposed Flame Retardancy Mechanism of MTB and MTB@HAp 142	
4.3.3	Proposed Flame Retardancy Mechanism of MF encapsulated MTB and MTB@HAp-PU.....	144
5	CONCLUSIONS	147
	REFERENCES	149
	APPENDICES	165

A.	Flame Retardancy Performance of HAp-PU Composite	165
B.	Flame Retardancy Performance of B-HAp-PU Composites.....	166
C.	Flame Retardancy Performance of MTB-MF1:1-PU Composites.....	167
D.	Flame Retardancy Performance of MTB-MF1:3-PU Composites.....	168
E.	Flame Retardancy Performance of MTB@HAp-MF1:1-PU Composites 169	
F.	Flame Retardancy Performance of MTB@HAp-MF1:3-PU Composites 170	
	CURRICULUM VITAE.....	171

LIST OF TABLES

TABLES

Table 1. Some of types of FRs may be used in PU composites.	18
Table 2. Some mineral fillers and physical properties.	23
Table 3. Most common boron-based flame retardants used in polymers.....	26
Table 4. Hydrated and Anhydrous Magnesium Borate Types.	30
Table 5. Test Criteria for Vertical Burning Classification.	40
Table 6. A varying amount of encapsulated MF versus Core Materials	55
Table 7. Polyurethane formulation	56
Table 8. Formulation of flame retarded PU composites.....	58
Table 9. Results of thermogravimetric analysis of MTB and MTB-MF microcapsules.	81
Table 10. Results of thermogravimetric analysis of MTB@HAp and MTB@HAp- MF microcapsules.	84
Table 11. TGA Data of neat PU and MTB-PU Composites sample	87
Table 12. DTGA data of neat PU and MTB-PU composites.	90
Table 13. TGA Data of neat PU and MTB@HAp-PU Composites sample.....	91
Table 14. DTGA data of neat PU and MTB@HAp-PU composites.....	93
Table 15. TGA Data of neat PU and MF-PU Composites sample.....	95
Table 16. DTGA data of neat PU and MF-PU composites.	96
Table 17. TGA Data of neat PU and MTB-MF-PU Composites sample.....	97
Table 18. DTGA data of neat PU and MTB-MF-PU composites.	99
Table 19. TGA Data of neat PU, MTB@HAp and MTB@HAp-MF-PU Composites sample.....	101
Table 20. DTGA Data of PU, MTB@HAp-PU and MTB@HAp-MF composites.	102
Table 22. LOI value and UL 94 rating of PU samples.....	117
Table 23. Cone calorimeter data of PU composite samples.....	118

LIST OF FIGURES

FIGURES

Figure 1. Basic reaction scheme for urethane formation	2
Figure 2. (a) Molecular structure of thermoplastic resin, (b) Molecular structure of thermoset resins, (c) the tensile stress–strain curves for thermoset (A) and thermoplastic (B)	3
Figure 3. Cross-section of a solid rocket motor consists of various components.....	5
Figure 4. A-End burning solid rocket propellant (cartridge type), B-Cross-section view of end burning solid rocket propellant.	7
Figure 5. Thermal degradation of mechanism of (a and b) the urethane segment and (c) N-substituted PUs	11
Figure 6. Char layer formation during dehydration of flame retardants.....	13
Figure 7. The effect of the "labyrinth effect" on the transfer of heat and mass within a material.....	14
Figure 8. Unit cell representation of Magnesium Tetraborate	30
Figure 9. The cone calorimetry curve shows key parameters such as time of ignition, extinction, PHRR, and THR	36
Figure 10. Illustration of typical Mass Loss Cone Calorimeter.....	37
Figure 11. LOI test apparatus.....	38
Figure 12. Radiant heat transfer to polymer with oxygen concentration decreasing 40 to 20%	39
Figure 13. Representation of the UL94 vertical burning test set up	40
Figure 14. Teflon made Conic Calorimeter test specimen mold.	49
Figure 15. Teflon made LOI specimen mold.....	50
Figure 16. Teflon made Vertical burning test (UL-94V) specimen mold.	51
Figure 17. The reaction scheme of the formation of MF prepolymer and MF resin	53
Figure 18. The preparation route of microcapsule with melamine-formaldehyde of MTB.....	54

Figure 19 Reaction schematic of surface-microencapsulated MTB/HAp core shell by melamine–formaldehyde resin.	55
Figure 20. Polyol and Diisocyanate reaction mechanism	56
Figure 21. Casting process and curing process of PU test specimens.....	57
Figure 23. XRD Pattern of Synthesized Magnesium Tetraborate and JCPDS Card:31-0787 lines.	60
Figure 24. XRD patterns of MgB ₄ O ₇ denoted as MTB, and Core/Shell structure of MgB ₄ O ₇ @HAp denoted as MTB@HAp.....	61
Figure 25. XRD Patterns of Microencapsulated MTB with Melamine-Formaldehyde Resin.	62
Figure 26. XRD Patterns of Microencapsulated MTB@HAp with Melamine-Formaldehyde Resin.....	63
Figure 27. FTIR spectra of synthesized MTB, HAp and MTB@HAp.	64
Figure 28. FTIR Spectrum of MTB and Microencapsulated MTB with MF.....	65
Figure 29. FTIR spectra of MTB@HAp and Microencapsulated MTB@HAp with MF.	66
Figure 30. SEM micrographs of synthesized MTB; a-Overview, b-close view, and MTB@HAp; c-overview, d-close view.....	67
Figure 31. EDS analysis of MTB and detected elements.....	68
Figure 32. EDS analysis of MTB@HAp and detected elements.	68
Figure 33. SEM micrographs of Microencapsulated MTB with MF resin, a-b, MF ratio 1:1, c-d, MF ratio 1:3.	69
Figure 34. EDS analysis of Microencapsulated MTB with 1:1 MF and detected elements.....	70
Figure 35. EDS analysis of Microencapsulated MTB with 1:3 MF and detected elements.....	70
Figure 36. SEM micrographs of Microencapsulated MTB@HAp with MF resin, a-b, MF ratio 1:1, c-d, MF ratio 1:3.....	71
Figure 37. EDS analysis of Microencapsulated MTB@HAp with 1:1 MF and detected elements.....	72

Figure 38. EDS analysis of Microencapsulated MTB@HAp with 1:3 MF and detected elements.	72
Figure 39. TEM images of synthesized MTB.....	73
Figure 40. TEM images of synthesized MTB@HAp.	73
Figure 41. TEM images of synthesized MTB-MF microcapsules, A: MTB-MF-1:1, B: MTB-MF-1:3.....	74
Figure 42. TEM images of synthesized MTB@HAp-MF microcapsules, A:MTB@HAp-MF-1:1, B: MTB@HAp-MF-1:3.	75
Figure 43. TGA/DSC curves of MTB.....	76
Figure 44. TGA/DSC curves of MTB@HAp.	77
Figure 45. TGA curves of MTB-MF (1:1), MTB-MF (1:3) microcapsule, MF Resin.	78
Figure 46. DCS curves of MTB-MF (1:1) microcapsule, MTB-MF (1:3) microcapsule, MF resin.....	78
Figure 47. TGA curves of MTB@HAp-MF (1:1) microcapsule, MTB@HAp-MF (1:3) microcapsule, MF resin.	81
Figure 48. DSC curves of MTB@HAp-MF (1:1) microcapsule, MTB@HAp-MF (1:3) microcapsule, MF resin.	82
Figure 49. TGA/DTGA Curve and FTIR of MF Resin at different temperatures. .	84
Figure 50. TGA curves of Neat PU and MTB-PU compositions.	87
Figure 51. First derivative (DTG) curves of neat PU and MTB-PU composites.....	89
Figure 52. TGA curves of MTB@HAp-PU compositions.	90
Figure 53. First derivative (DTG) curves of neat PU and MTB@HAp-PU composites.....	92
Figure 54. TGA curves of neat PU and MF-PU compositions.	94
Figure 55. First derivative (DTG) curves of MF-PU composites.	95
Figure 56. TGA curves of MTB and MTB-MF-PU compositions.	97
Figure 57. First derivative (DTG) curves of Neat PU and MTB-MF-PU composites.	99

Figure 58. TGA curves of PU, MTB@HAp and MTB@HAp-MF-PU composites.	101
Figure 59. First derivative (DTG) curves of Neat PU and MTB@HAp-MF-PU composites.	102
Figure 60. TGA/DTGA and FTIR of neat PU at different temperatures.	103
Figure 61. TGA/DTGA and FTIR of 10-MTB-PU composite at different temperatures.	105
Figure 62. TGA/DTGA and FTIR of 15-MTB@HAp-PU composite at different temperatures.	106
Figure 63. TGA/DTGA and FTIR of 2.5-MF-PU composite at different temperatures.	107
Figure 64. TGA/DTGA and FTIR of 5-MTB-MF1:3-PU composite at different temperatures.	109
Figure 65. TGA/DTGA and FTIR of 5-MTB@HAp-MF1:3-PU composite at different temperatures.....	110
Figure 66. LOI and UL-94 rating of MTB containing PU composites.	112
Figure 67. LOI and UL-94 rating of MTB@HAp containing PU composites.....	113
Figure 68. LOI and UL-94 rating of MF containing PU composites.	114
Figure 69. LOI and UL-94 rating of MTB-MF microcapsule containing PU composites.	115
Figure 70. LOI and UL-94 rating of MTBMTB@-MF microcapsule containing PU composite.....	116
Figure 71. HRR curves of MTB-PU composites.....	120
Figure 72. HRR curves of MTB-MF-PU composites.	120
Figure 73. HRR curves of MTB@HAp-PU composites.	121
Figure 74. HRR curves of MTB@HAp-MF-PU composites.	122
Figure 75. Images of residual chars from PU composites; A:5-MTB-PU, B:10-MTB- PU, C:15-MTB-PU, D: 20-MTB-PU.	124
Figure 76. SEM images and EDS results of residual chars from 20-MTB-PU sample.	125

Figure 77. Images of residual chars from PU composites; A:5-MTB@HAp-PU, B:10-MTB@HAp-PU, C:15-MTB@HAp-PU, D: 20-MTB@HAp-PU.	127
Figure 78. SEM images and EDS results of residual chars from 20-MTB@HAp-PU sample.	128
Figure 79. Images of residual chars from PU composites; A:5-MTB@HAp-MF 1:1-PU, B:5-MTB@HAp-MF 1:3-PU.....	129
Figure 80. SEM images and EDS results of residual chars from A: 5-MTB@HAp-MF 1:1-PU and B: 5-MTB@HAp-MF 1:3-PU samples.....	130
Figure 81. Images of residual chars from PU composites; A:5%MTB-MF 1:1-PU, B:5%MTB-MF 1:3-PU.	131
Figure 82. SEM images and EDS results of residual chars from A: 5-MTB-MF 1:1-PU and B: 5-MTB-MF 1:3-PU samples.	133
Figure 83. XRD patterns of residual chars from the PU samples.....	134
Figure 84. XRD patterns of residual chars from the PU samples.....	135
Figure 85. XRD patterns of residual chars from the PU samples.....	136
Figure 86. XRD patterns of residual chars from the PU samples.....	137
Figure 87. FTIR spectra of residual chars from the PU samples.	137
Figure 88. FTIR spectra of residual chars from the PU samples.	138
Figure 89. FTIR spectra of residual chars from the PU samples.	139
Figure 90. FTIR spectra of residual chars from the PU samples.	140
Figure 91. Thermal degradation steps of PU	140
Figure 92. Primary degradation steps of urethane linkage.....	141
Figure 93. Proposed Flame retardancy mechanism of MTB and MTB@HAp in condensed Phase.	144
Figure 94. Proposed reaction of amine group and Isocyanide in TDI.	146
Figure 95. Proposed Flame retardancy mechanisms of MF-MTB and MF-MTB@HAp in condensed and gas phases.....	146

LIST OF ABBREVIATIONS

ASTM	American Society for Testing Materials
APB	Ammonium Penta Borate
ATO	Aluminum Trioxide
CTAB	Hexadecyltrimethylammonium bromide
CC	Cone Calorimeter
CE	Chain Extender
CO	Carbon Monoxide
CO ₂	Carbon Dioxide
DDI	Dimeryl Diisocyanate
DI	Deionized Water
DSC	Differential Scanning Calorimeter
DTGA	Differential Thermogravimetric Analysis
EDS	Energy-dispersive X-ray spectroscopy
FA	Formaldehyde
FTIR	Fourier Transform Infrared Spectrophotometer
HAp	Hydroxyapatite
HRR	Heat Release Rate
HSM	Heat Shielding Material
HS	Hard Segment
HTPB	Hydroxy Terminated PolyButadiene
IPDI	Isophorone Diisocyanate
ISO	International Organization for Standardization
JCPDS	Joint Committee on Powder Diffraction Standards
LOI	Limiting Oxygen Index
MDI	Methylene Diphenyl Diisocyanate
MF	Melamine Formaldehyde Resin
MLC	Mass Loss Calorimeter
ML	Mass Loss
MTB	Magnesium Tetraborate

MTB@HAp	Core-Shell Magnesium Tetraborate/Hydroxyapatite
MTB-MF	Melamine Formaldehyde encapsulated Magnesium Tetraborate
MTB@HAp-MF	Melamine Formaldehyde encapsulated Magnesium Tetraborate- Hydroxyapatite
NCO	Isocyanate
OH	Hydroxyl
PHRR	Peak Heat Release Rate
PU	Polyurethane
PVC	Polyvinyl Chloride
PVP	Polyvinylpyrrolidone
SEM	Scanning Electron Microscopy
SRM	Solid Rocket Motor
SS	Solid State-Soft Segment
TDI	Toluene diisocyanate
TEM	Transmission Electron Microscopy
TGA	Thermogravimetric Analysis
THE	Total Heat Evolved
THR	Total Heat Release
TPS	Thermal Protection System
TPU	Thermoplastic Polyurethane
TTI	Time To Ignition
UL-94	Vertical Burning Test
XRD	X-Ray Diffraction

CHAPTER 1

INTRODUCTION

Polyurethane was first described by Bayer in 1937. The first polyurea was made by reacting hexane-1,6-diamine with hexane-1,6-diisocyanate. At that time, 4,4-diphenylmethane diisocyanate and 1,5-naphthalene diisocyanate were the two diisocyanates used, which are still key products in polyurethane chemistry today. The initial use of polyurethanes was for foams, coatings, and cast elastomers [1]. Polyurethanes are commonly used in different industries due to their customizable features. Around half of the polyurethane market is made up of coatings, adhesives, sealants, and elastomers, whereas the rest of flexible and rigid forms. The mechanical attributes of polyurethane, such as tensile or compressive strength, brittleness, hardness, and resilience, as well as their physico-chemical traits like density and thermal conductivity coefficient, and flammability, determine their application requirements [2]. In various applications, there is a high demand for polyurethane to possess flame-retardant properties in order to prevent potential fire hazards. The wide range of applications for polyurethane prompts us to create and analyze new composite materials that exhibit significantly improved properties compared to their original and individual component materials. These materials provide superior mechanical properties, such as greater elasticity, strength, hardness, impact resistance, and shock resistance, as well as improved thermal properties [3].

1.1 Polyurethane Types and Synthesis Methods

Polyurethane (PU) is created by combining three main ingredients: polyisocyanate, polyester or polyether polyol, and a chain extender like diol or diamine. In this process, isocyanate is the most reactive component because of its -NCO groups.

Achieving the desired properties of the PU product involves carefully balancing the ratio of -NCO to -OH groups. If the amount of -NCO groups is too little or too much, allophanate or biuret compounds will form, which have different properties. It is worth noting that urea and isocyanurate linkages are more thermally stable than polyurethanes [4]. The reaction of an isocyanate (-NCO) with an alcohol (-OH) forms the urethane linkage in PUs. The general reaction of urethane is shown in Figure 1.

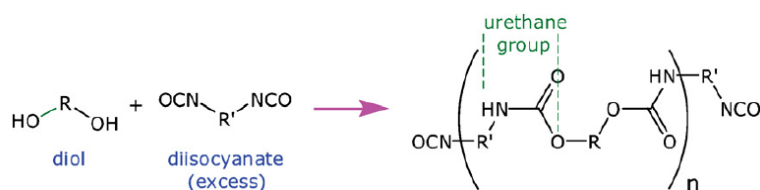


Figure 1. General reaction scheme for urethane formation[5].

Step-growth polymerization (polyaddition) produces them from macro-diols (macrotriols), diisocyanates (polyisocyanates), and chain extenders or cross-linkers [6]. Polyurethanes (PUs) typically consist of repeating urethane groups, but they may also contain other moieties such as urea, ester, ether, and aromatic. The versatility of PU production lies in the ability to select raw materials such as di-/tri-isocyanates, polyols, and chain extenders, which can be tailored to meet specific requirements. Common polyols include polyethers, polyester polyols, and acrylic polyols. Popular diisocyanates used in PU formulations include methylene diphenyl diisocyanate (MDI), hydrogenated MDI (H12MDI), toluene diisocyanate (TDI), isophorone diisocyanate (IPDI), xylene diisocyanate (XDI), and 1,5-naphthalene diisocyanate (NDI).

Polyurethanes (PUs) come in both thermoplastic and thermoset varieties. The thermoplastic type, known as TPUs, are composed of linear, segmented copolymers that alternate between hard segments (HSs) and soft segments (SSs). HSs are made up of diisocyanate and short-chain extender (CE) molecules, such as diols or

diamines. These segments are rigid and highly polar, with significant inter-chain interaction thanks to hydrogen bonding between urethane/urea groups. This bonding acts as a reinforcing filler for the soft matrix. In contrast, SSs are formed from linear long-chain diols or polyols, making them flexible and weakly polar. Thermoset PUs, on the other hand, can be created using one or a combination of the following methods:

- utilizing polyols with functionalities greater than 2,
- substitution of a trifunctional hydroxyl compound in place of the normal glycol CE,
- utilizing isocyanates with functionalities greater than 2,
- utilizing NCO:OH ratios greater than 1,
- introduction of a crosslinker into the HS, SS or CE [5].

Figure 2 shows the thermoplastic and thermoset resin molecular structure. Thermoset resins containing crosslinking forms an irreversible chemical bond by comparing thermoplastic and thermoset structures. The crosslinking structure prevents the risk of remelting when heat is applied. Therefore, thermoset resin cannot be softened upon reheating and hardened upon cooling after undergone the chemical reaction [7].

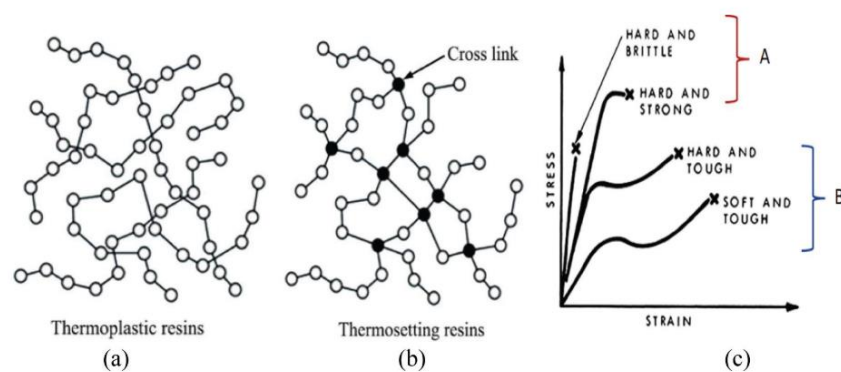


Figure 2. (a) Molecular structure of thermoplastic resin, (b) Molecular structure of thermoset resins, (c) the tensile stress–strain curves for thermoset (A) and thermoplastic (B)[7].

Despite being widely used in households and industries, PUs have some drawbacks that hinder their application. The most significant issue with PUs is their high flammability, which leads to the emission of extremely toxic and combustible gases (such as CO and HCN) and smoke [8].

1.2 Polyurethanes as Technological Material

Rigid polyurethane (PU) is a versatile group of polymers that possess a range of desirable properties, including excellent thermal insulation, chemical resistance, and toughness, as well as good flexibility at low temperatures. As a result, they have become widely utilized in various industries, particularly in construction, where they are used for thermal insulation purposes, as well as in household appliances and refrigerators. Additionally, they have found use in transporting liquefied natural gas and insulating cryogenic space launchers, as ablative material in space shuttles, as binder and inhibitor material in solid rocket propulsion systems [9, 5, 10].

1.2.1 Polyurethanes in Solid Propellant Rocket Technology

Figure 3 shows typical cross-section of a solid rocket motor consists of various components. A solid rocket motor is essentially comprised of a pressurized container that houses a mass of solid propellant, referred to as the propellant grain. The propellant grain is composed of Polyurethane (Hydroxy Terminated Polybutadiene, HTPB based PU) and is meticulously designed to generate the desired pressure (thrust) over time and to create an internal space for the combustion products in the combustion chamber [11, 12]. In order to protect against significant convective and radiative heat exposure, the motor case has been designed to include an internal wall that is reinforced with a pressure tank and thermal insulation. This insulation is made from non-combustible materials and serves as a liner, utilizing HTPB based PU to bond the propellant to the insulation, while also functioning as a stress transfer

agent[13][14]. Additionally, specific sections of the propellant grain may be coated with PU-based inhibitors, allowing for the desired pressure-time curve to be achieved [15].

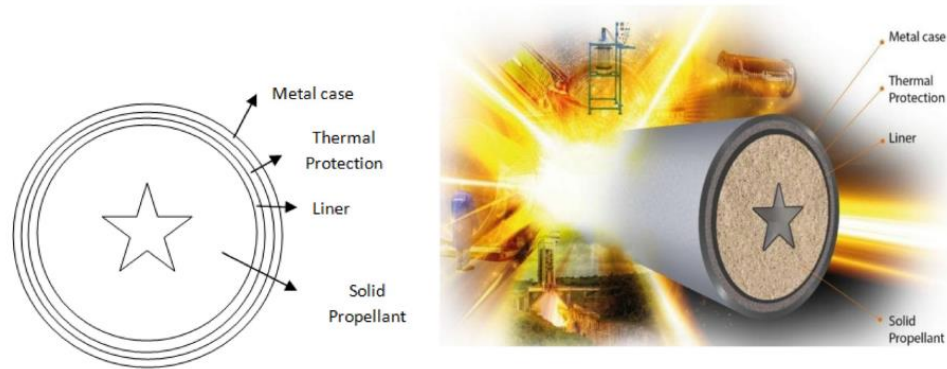


Figure 3. Cross-section of a solid rocket motor consists of various components[16].

1.2.1.1 Polyurethane Binder Systems

In the early 1950s, the manufacturing of polyurethane binder systems was initiated, and they were discovered to offer a consistent, uncontaminated cure. High molecular weight glycols that have hydroxyl groups at both ends were employed to produce polyethers, which were then treated with diisocyanates to cure them. In the past, polyurethane propellant binders faced numerous issues such as low-temperature crystallization, moisture sensitivity, and non-ideal aging properties. However, these problems were resolved by incorporating certain chemicals like plasticizers, bonding agents, and antioxidants. In the 1960s, hydroxy-terminated polybutadiene (HTPB) was developed which proved to be beneficial for rocket motors' tests in 1972. It exhibited higher strain capacity even at low temperatures and better aging properties. Over time, HTPB has become the most commonly used polymer in polyurethane propellant binders [17].

1.2.1.2 Polyurethane as Thermal Protective Material

Thermal protection systems (TPS) are materials specifically designed to protect the metallic or composite casing of rocket engines. These systems undergo a process called ablation, which is the thermal decomposition of organic constituents that form the char layer under high temperature (pyrolysis). The ablated layer serves as a protective shield against the intense mass and heat transfer that occur during solid propellant combustion. The elevated temperatures that arise during Solid Rocket Motors (SRM) combustion have been known to rapidly deteriorate even the most robust metallic alloys. Without suitable protection, the case may be subjected to severe conditions that cause explosions [16, 10].

Polymeric ablatives, including rigid and elastomeric fiber-reinforced options, heat shielding materials, lightweight ceramic ablators, and nanostructured alternatives, serve as effective thermal insulators. The potential of PU nanocomposite as heat shield material (HSM) was explored and deemed suitable for SRM with the inclusion of various fillers and reinforcements. Flame retardancy was evaluated through the examination of melamine phosphate and PU encapsulated with melamine phosphate/polyoxymethylene [14, 18].

1.2.1.3 Polyurethane-based inhibitors

In the field of rocket propellant technology, the term 'inhibition' is utilized with regards to the stable combustion of solid propellants. When employed in rocket motors, propellant grains necessitate the use of an inert substance known as an 'inhibitor' on their surface to ensure a desired burning pattern and to decrease the likelihood of the propellant igniting at its outer surface closest to the motor casing shown Figure 4. This, in turn, minimizes the likelihood of the propellant burning in a cone shape [19, 20, 21]. The effectiveness of a rocket is not only dependent on the propellant grains but also heavily relies on efficient inhibition. Several polymeric materials have been identified as inhibitors for a composite propellant. These

materials include polyurethanes, epoxy resin, phenolic resin, melamine formaldehyde resin, chloro sulfonated polyethylene, thiokol rubber, and nitrile rubber, among others. Among the available materials, polyurethanes are the optimal inhibiting substance due to their ability to align readily with the fundamental composition of the HTPB-based composite propellant [15].

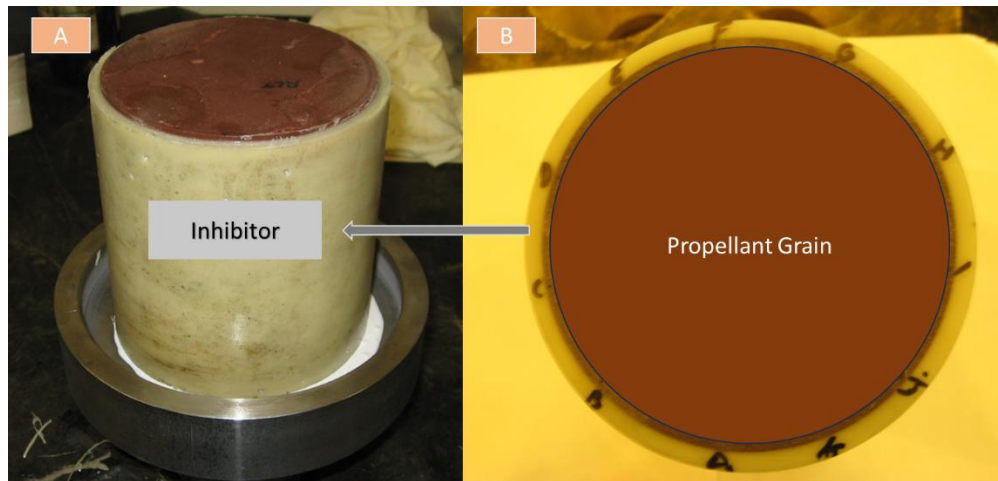


Figure 4. A-End burning solid rocket propellant (cartridge type), B-Cross-section view of end burning solid rocket propellant.

1.3 Flammability of PUs

The degree of flammability in polymer materials is a key factor in determining their susceptibility to combustion, including glowing, smoldering, and smoking. Combustion is a complex process that involves the thermal destruction of the polymer, ignition of gaseous mixtures, propagation of flames, emission of heat and radiation, release of toxic gases, and self-extinguishing reactions [22]. Numerous factors affect the phenomenon of polymer combustion, including composition, chemical structure, and density.

There are three types of combustion based on the phase state of the reactants: homogeneous, heterogeneous, and mixed. Homogeneous combustion occurs when

there is no separation between the reactants and takes place in the gas phase above the combustible material. This produces a visible flame as a result of evaporation, sublimation, or pyrolysis which releases large amounts of flammable products. However, heterogeneous combustion takes place at the phase boundary and is located on the surface of the combustible solid. This type of polymer combustion typically involves both homogeneous and heterogeneous combustion, resulting in smoldering, embers, and light without visible flames [23].

1.4 Thermal Stability of PUs

Thermal stability is a crucial factor in determining the resilience of a polymer when subjected to high temperatures. It encompasses various characteristics like heat resistance, durability, melting point, softening point, and thermal decomposition. Polymers that exhibit superior thermal stability display a higher heat deflection temperature under load and minimal mass loss when exposed to elevated temperatures. These properties ensure that the polymer retains its efficacy and functionality, even in the most extreme temperature conditions [4]. The stability of a polymer under high temperatures is a crucial aspect that determines its performance. Thermal stability comprises various attributes, including heat resistance, durability, melting point, softening point, and thermal decomposition [23].

Polyurethanes (PUs) possess unique properties due to their microstructure, which is comprised of two distinct phases: hard and soft segments. The soft segments (SS) consist of polyols and exhibit low glass transition temperatures, while the hard segments (HS) are created from diisocyanates and chain extenders and have high glass transition temperatures. PUs can be viewed as a block copolymer, where soft and hard segments alternate along the macromolecule chain. The soft segments offer flexibility to the PU, while the hard segments, containing urethane and aromatic rings, cluster into microdomains through hydrogen bonding. These domains serve as physical cross-linking points for the material [3]. The breakdown of PUs due to heat

(known as thermal decomposition) is a significant occurrence that holds importance in both fundamental and technological aspects. By studying the degradation process, we can identify the best conditions for designing and processing PUs, resulting in high-performance polymers with enhanced thermal stability [5]. Fundamental research has shown that the thermal decomposition of polyurethanes (PUs) is a complex process consisting of multiple partial decomposition reactions. The thermal stability of a material refers to the temperature or time limit within which it can be used without significant loss of properties. Regarding commercial applications, the study of thermal decomposition processes entails two critical considerations. Firstly, it involves stabilizing a polymer to generate innovative materials that possess the desired level of thermal stability and flame resistance. This is essential to meet the current demands of materials engineering. Secondly, the process aims to gain an in depth understanding of material performance and obtain characteristic thermal decomposition data for further analysis. For example, the effectiveness of various PU materials is largely contingent on their ability to withstand thermal, oxidative, and fire-related stresses [5].

1.4.1 Thermal Degradation Process of PUs

When PU chains are heated up, their covalent bonds vibrate and rotate in a complex manner within their immediate area. If the heat is increased, these bonds can break, resulting in the formation of many different fragment radicals or small molecules. These fragments may then combine with each other or break apart even further. Afterwards, the fragments that may be turned into vapor, spread out, or turned into carbon. The process of breaking down ends when all of the materials that can turn into gas are gone, and char (a complicated, insoluble substance) is formed. This substance will not change anymore once it reaches a certain temperature. Depending on the structure of the PU, the structure of char is composed of both crystalline and amorphous regions. It is comprised of polynuclear aromatic carbon compounds that contain heteroatoms such as oxygen (O), nitrogen (N), phosphorus (P), and sulfur

(S). In addition to the carbonaceous (char) residue, there might be inorganic residue present, which comes from heteroatoms within the PU structure or added as an additive. The thermal stability of PU is mainly determined by the nature of starting materials and the conditions of polymer preparation [24]. Thermal stability measures molecular rigidity directly, as the degradation and chemical reaction rely on macromolecular chain movement and excitation gained from thermal energy exposure at high temperatures. The decomposition process is influenced by both the sample's properties and its surroundings. In Figure 5, polyurethane (PU) breaks down through a combination of different processes, primarily random-chain scission, and crosslinking. Chain-end scission, also known as unzipping, is another potential route. However, crosslinking and random chain scission are the most common ways for PUs to decompose. For crosslinked PUs, breaking the bonds within the polymeric matrix requires a significant amount of heat energy. As a result, the thermal decomposition of crosslinked PUs begins with the degradation of side chains[5]. During the decomposition of polyurethane, the resulting products are primarily hydrogen cyanide and carbon monoxide. However, other compounds such as nitric oxides, nitriles, hydrogen chloride, and carbon dioxide may also be present. At temperatures above 800 °C, the simplest compounds are formed as a result of the defragmentation of previously decomposed products [23].

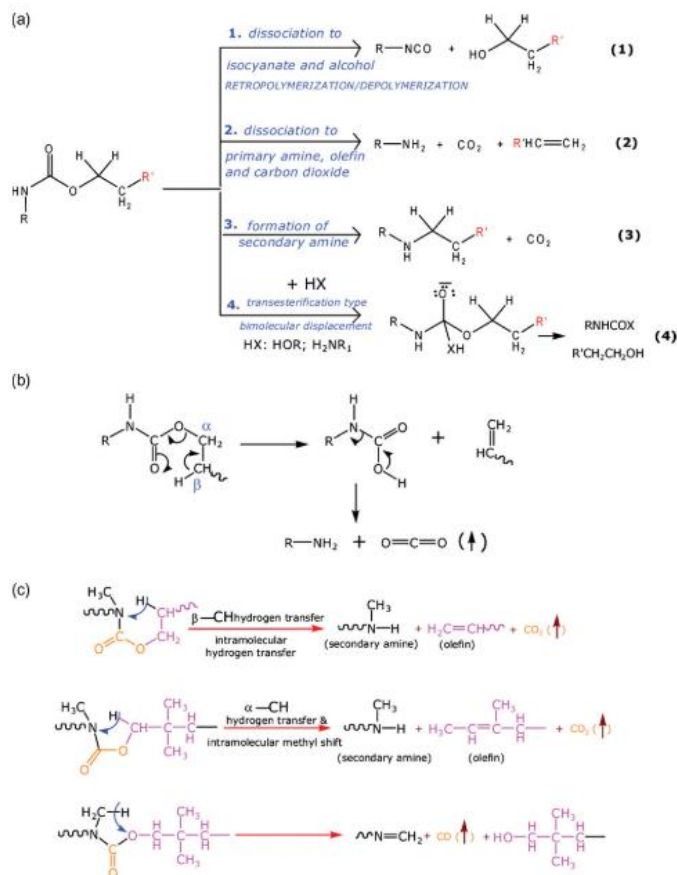


Figure 5. Thermal degradation of mechanism of (a and b) the urethane segment [19] and (c) N-substituted PUs [5].

1.5 Flame Retardancy of Polymers

There are various ways to decrease the flammability of polymers, such as adding non-flammable agents to the reaction mixture. Flame retardants can also be added during the processing of macromolecular compounds (as additive flame retardants) or during the synthesis of foam components (as reactive flame retardants) to prevent combustion through chemical activity [23].

1.5.1 Mechanisms of Action of Flame Retardants

Flame retardants are classified into two categories based on their nature and potential interactions with the polymer matrix: reactive and additive. Reactive flame retardants react with the polymer and are used to chemically modify plastics by incorporating flame-retardant elements into the macromolecular structure. These types of flame retardants have the advantage of forming permanent bonds with the polymer, which greatly reduces volatilization during use. The chemical bonds also prevent migration to the plastic's surface. Reactive flame retardants do not function as plasticizers, nor do they negatively impact the composite's thermal stability. Examples of reactive flame retardants include tetrabromodiene, pentabromophenol, and hexabromophthalate, which are primarily used in thermosetting plastics such as polyester resins, epoxy resins, and polyurethanes [8]. These flame retardants can be introduced into the polymer chain during polymerization. On the other hand, additive flame retardants are incorporated into macromolecular compounds during the processing stage. In this instance, there is no chemical bonding occurring between the atoms of the polymer's molecular structure. These substances are also capable of acting as plasticizers or fillers. It is essential for them to be compatible with the polymer, allowing for a uniform distribution throughout the polymer matrix and ultimately resulting in consistent material performance. During the thermal destruction stage of the polymer, the flame retardant is anticipated to be activated. Flame retardants operate through two mechanisms: chemical and physical. Both approaches share the common goal of reducing the formation rate of volatile, flammable, pyrolysis products [25].

1.5.1.1 Chemical Mechanism

Flame retardants have two main chemical mechanisms: reactions in condensed phase and in gas phase. The first group generates a char layer on the burning polymer's surface. This is achieved through flame retardant dehydration, cross-linking, or other

reactions, as shown in Figure 6. These reactions increase the molten polymer's viscosity on the surface of burning material, which reduces the heat and mass transfer, thus preventing the spread of the flame. Additionally, the formation of a char layer helps stabilize the polymer structure and protects the burning material's interior.

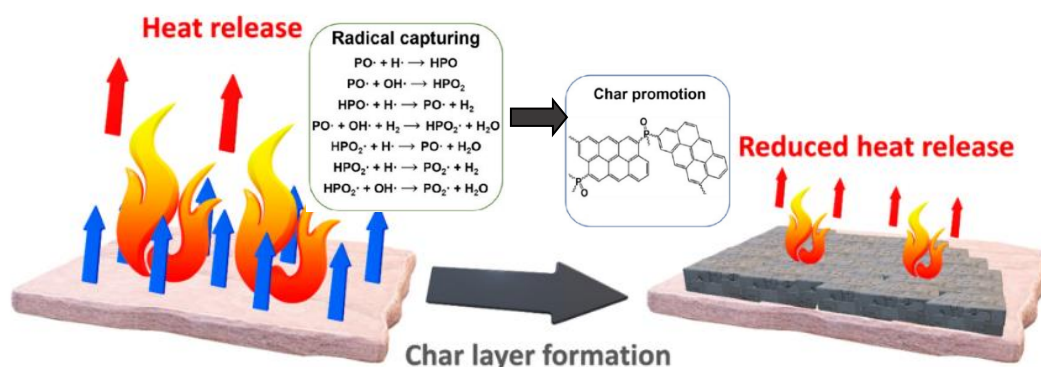


Figure 6. Chemical mechanism for char layer formation of phosphorus type flame retardants.

Considering the gas phase, chemical flame retardancy relies mainly on stopping the combustion process by scavenging free radicals. Flame retardants break down into products that combine with highly reactive H and OH radicals, which play a crucial role in fire propagation. This leads to the creation of inactive molecules or less reactive radicals, which ultimately inhibits the combustion process. This mechanism is particularly important when halogen flame retardants are used [23, 26].

1.5.1.2 Physical Mechanism

The addition of flame retardants can enhance the ability of polymers to withstand fire by altering the material's thermal properties. By incorporating flame retardants with high thermal conductivity, heat from flames can be evenly distributed throughout the material, which can help delay the pyrolysis process and prevent the temperature from rising too quickly on the material's surface [27]. Furthermore,

additives with a moderate decomposition temperature can break down in an endothermic process and remove heat from the combustion system. Another method is to decrease the level of thermo-oxidative decomposition in macromolecular compounds by reducing the amplitude of thermal fluctuations in their macromolecules. Flame inhibitors create barrier layers that hinder or prevent the transfer of energy and mass between the combustion zones (solid and gaseous) [28]. Layered clays are often used to create a physical barrier layer due to their flake-like shape. This results in the "labyrinth effect" shown in Figure 7. Flame retardants can have a significant impact on the release of non-flammable gases, such as CO₂, H₂O, NH₃, and SO₂, during their thermal decomposition. These gases can dilute the combustible gases, resulting in a poor combustion mixture that contains a lower concentration of oxygen and poor spontaneous ignition or sustained combustion [29].

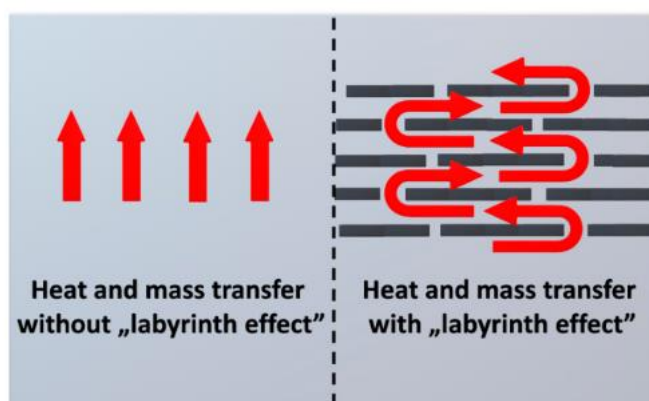


Figure 7. The effect of the "labyrinth effect" on the transfer of heat and mass within a material[23].

1.5.1.3 Synergistic and Antagonistic Effects of Flame Retardants

Synergism is a commonly discussed phenomenon in literature focused on flame retardancy of polymers [30, 31]. These effects can be observed in both vapor-phase and condensed phase-active FR systems. The various modes of action involve a wide array of interactions among all three components: polymer, FR additive, and

synergist, which include chemical interactions between the FR additive and the synergist or the FR additive and the polymer. Synergies can also occur among two synergists and the FR additive, or even between two polymers in a polymer mixture. In some instances, the synergist may not be a flame retarding agent and only becomes active in the presence of an FR additive, such as with halogen-based additives and antimony trioxide. Other cases, such as bromine-phosphorus synergism, involve both additives acting as active flame retardants. However, some formulations may have antagonistic effects, leading to a reduction in flame retardancy parameters, as seen with the application of phosphorus derivatives together with nitriles. In the following sections, we will briefly discuss and compare some of the synergistic systems [32].

1.5.1.3.1 Halogen-Antimony Synergism

The synergy observed in this process is influenced by both activities in the condensed and vapor phases [33]. Sb_2O_3 primarily affects the gas phase. The antimony halides react with atomic hydrogen, resulting in the production of HX, SbX, SbX_2 , and Sb, which in turn react with atomic oxygen, water, and hydroxyl radicals to produce SbOH and SbO. These compounds then scavenge H atoms. Water also reacts with SbX_3 to produce SbOH and HX. Additionally, fine solid dispersions of SbO and Sb are produced in the flame and catalyze H recombination. Antimony halides are also believed to delay the escape of halogen from the flame, increasing its concentration while also diluting the flame [32].

1.5.1.3.2 Bromine-Ammonia Synergism

The synergistic effect is caused by the NH_4Br molecule having a low dissociation energy to HBr and NH_3 , which is much lower than the dissociation energy of the C-Br bond. At 320°C , the degree of dissociation is 38.7%, meaning that a significant amount of HBr is available when polymer begins to decompose. While the

possibility of synergism between HBr and NH₃ in the gaseous phase cannot be ruled out, both compounds are formed at the same time and reach the flame simultaneously. While HBr acts primarily as a radical scavenger, ammonia is believed to act as a flame diluent. Little is known about the behavior of ammonia in the flame, particularly in the presence of H, Br, OH, and O radicals [32].

1.5.1.3.3 Phosphorus-Nitrogen Synergism

Phosphorus-based flame retardants possess a greater degree of specificity with regards to polymer chemistry when compared to halogen-based alternatives. They exhibit optimal efficacy when used in oxygen- or nitrogen-containing polymers, as they require a reaction with the polymer itself typically through phosphorylation in order to form a char. This char serves to inhibit the transfer of heat flux to the polymer surface and slows down the diffusion of volatile pyrolysis byproducts into the flame. P-N bonds are more reactive compared to P-O bonds when it comes to phosphorylation. This is relevant when considering intumescence in P-N systems during pyrolysis and combustion, as the effect is the same regardless of when it occurs. Ultimately, phosphorylation results in increased fire retardancy effectiveness due to higher rates and yields. This is because phosphorylation enhances dehydration, crosslinking of the polymer, and char formation, making it more efficient [32].

1.5.1.3.4 Synergism in Intumescent Systems and Catalytic Effect of Melamine

Intumescence is a specific type of mechanism within a condensed phase. It does not involve any activity in the gaseous phase. When combustion occurs in intumescent systems, foamed char is formed instead of combustible gases. This char plays an important role by acting as a barrier in two ways. Firstly, it hinders the passage of combustible gases and molten polymer to the flame. Secondly, it shields the polymer from the heat of the flame. The amount and properties of the char determine the

effectiveness of the system. Synergistic effects can improve the performance of the char in a particular system. All intumescent systems use three basic ingredients: a catalyst, a charring agent, and a blowing agent. On the other hand, diverse roles of melamine include undergoing endothermic decomposition, causing the release of non-combustible gases like water, CO₂, and ammonia, and further destabilizing the flame by diluting the combustible decomposition products of the polymer matrix. While this reaction is not heavily dependent on the polymer matrix, effectiveness of melamine as a flame retardant may vary depending on the polymer it is used with. Thus, the assumption that effectiveness of melamine is solely due to its endothermic decomposition, intumescence, and dilution of combustible gases is only partially accurate, as it also depends on the specific polymer class it is used with [32].

1.5.2 Classification of Flame Retardants

The practice of adding chemicals to materials to slow down fire spread or prevent ignition has been around for centuries. Even in ancient times, people would add simple substances like alum and vinegar to wood to make it less susceptible to flames. While flame retardant chemistry has come a long way since then, many of the fundamental chemistries in use today have been around for decades. There are seven known classes of flame-retardant chemistries [31, 34], but only the first five are commonly used in commercial products due to their cost and effectiveness [35]. Table 1 provides a summary of some of the most widely used FRs today.

The five classes of flame-retardant chemistry are:

- Halogen-based,
- Phosphorus-based,
- Nitrogen-based,
- Polymer nanocomposites,
- Inorganic-based.

Table 1. Some of types of FRs may be used in PU composites[8].

Halogen-Containing FRs	Phosphorous-Containing FRs	Nitrogen-Containing FRs	Other FRs
Cycloaliphatic compounds (e.g., HET acid, TCPA, HCCPD, HBCDD, HBCD, TBPA)	Elemental red phosphorous	Melamine and its derivatives (e.g., MCA, melamine homologs)	Metals hydroxides (e.g., ATH, MDH)
Esters/ethers (PBDEs, DECA, DBDPO)	Inorganic phosphates (e.g.,APP)	Inorganic compounds (e.g., APP, ammonium bibo- rate/pentaborate)	Metals salts (e.g., zinc borate, zinc stannate, zinc hydroxystannate, zinc carbonate, calcium carbonate, manganese carbonate, ammonium carbonate, antimony trioxide, arsenic oxide, calcium sulfate)
Derivatives of aromatic compounds (e.g., TBBPA, TBP, pentachlorophenol)	Organic phosphates, (including aryl phosphates (e.g., TPP)	Organic compounds (e.g., urea, EUF)	Expandable graphite
Other organic compounds (e.g., halogen-containing polyols and isocyanates, aliphatic compounds, polymers, paraffins)	Chlorinated phosphates (e.g., TCEP, TCPP, TDCP)		Carbon nanomaterials
			Clays (e.g., montmorillonite, kaolinite)

1.5.2.1 Halogen-based Flame Retardants

Halogen-containing compounds were historically the first FRs used on PUs. However, their usage led to deterioration of PU mechanical properties and environmental issues. As a result, halogen-free FRs based on phosphorus and nitrogen organic and inorganic compounds have emerged [8]. The action of flame retardants applies to both gas and condensed phases due to synergistic systems [23]. Flame retardants function by releasing hydrogen halides (HCl and HBr) when the polymer decomposes thermally. When a fire occurs, various chemical halide intermediates are produced during the intricate reactions of polymer decomposition

and pyrolysis. These halide species are transported into the flame front of the burning polymer, where they inhibit vital free-radical reactions of combustion. Consequently, the flames become unstable and extinguish, resulting in reduced heat release. However, the hindrance of combustion chemistry often leads to the creation of more smoke and toxic gases (hydrogen chloride, bromine) during fires, as the halides prevent complete combustion of carbon-containing species in the flame [36].

1.5.2.2 Phosphorus-based Flame Retardants

Phosphorus-based flame retardants are available in both inorganic and organic forms. Inorganic options include ammonium phosphates, ammonium polyphosphates, and red phosphorus, while organic choices consist of organophosphates, organophosphonates, polyphosphonates, and hybrid metal phosphonate salts. Interestingly, even DNA has been found to have flame retardant properties due to its phosphorus content. The process by which phosphorus imparts flame retardancy to polymers is intricate and varies depending on the specific polymer in question. However, when combined with polymers containing oxygen and nitrogen heteroatoms, phosphorus can produce a highly cross-linked material that reduces heat release rate and slows mass loss during burning. Furthermore, certain phosphorus compounds are capable of forming glassy structures with high thermal stability that can offer greater protection than carbon-based chars [36].

1.5.2.3 Nitrogen-based Flame Retardants

Melamine (2,4,6-triamino-1,3,5-triazine, $C_3N_6H_6$) and its derivatives are widely recognized as the most important nitrogen-based flame retardants for polyurethanes [37]. Melamine's exceptional effectiveness in diminishing the flammability of polymer materials is owing to its complicated mode of action. When heated, melamine absorbs heat and generates non-combustible nitrogen-based gases, such as ammonia, which act as a diluent [38]. The incorporation of melamine into the polyurethane

material increases the material's heat capacity and combustion system, effectively reducing its surface temperature and inhibiting ignition. As the temperature rises above 250 °C, melamine degrades into various oligomeric and polymeric products, such as melam, melem, or melon, which are more stable than melamine (with stability levels of approximately 350, 450, and 600 °C, respectively). The final stage of decomposition and deamination generates graphitic carbon nitride, which creates a protective layer for polyurethane. In summary, melamine and its derivatives have been widely studied as effective flame retardants for polyurethane materials [39].

1.5.2.4 Polymer Nanocomposite Flame Retardants

Nanocomposites are in high demand due to their unique combination of properties, which can greatly enhance the resulting system. Their improved mechanical properties and ability to maintain flame retardant performance make them a desirable choice. Additionally, they offer the opportunity to create flame retardant materials with superior qualities while reducing the need for fire retardant chemicals. The role of polymer nanocomposites is well-understood, as they form a nanoparticle-rich barrier that effectively slows down the mass loss rate and heat release rate [36, 35].

1.5.2.4.1 Carbon nanomaterials

Expandable graphite is an exceptional material that serves as a flame retardant for a variety of materials. Its composition comprises of graphite flakes intercalated with sulfuric acid or other potent oxidizers. When exposed to heat sources like fire, it expands hundreds of times, which resulting a carbonaceous layer that protects the surface of the material. This protection occurs due to limited heat and mass transfer, which restricts the spread of fire [40]. When it combusts, both carbon and sulfur undergo oxidation, resulting in a non-flammable gas mixture of water vapor, sulfur, and carbon dioxide. This oxidation process consumes a significant amount of oxygen from the atmosphere, which naturally prevents fires. However, to achieve

satisfactory outcomes, it must be applied in relatively high concentrations, sometimes exceeding 20 wt%. This concentration can impact the processing and mechanical performance of PUs. Thus, it can be effectively combined with other types of flame retardants, primarily phosphorus-based, to reduce its loading and enhance the mechanical aspects of the material, providing a synergistic effect that focuses on flammability [41, 23, 42, 43].

1.5.2.4.2 Clays

Initially, nanofillers were intended to boost the mechanical properties of composites, much like their larger-scale counterparts. However, research has revealed that the inclusion of nanofillers in composites also yields benefits with regards to their flammability and fire behavior. Aluminosilicate nanofillers are employed as compounds to curtail dripping in composites that are flame-retarded with conventional flame retardants. Furthermore, they have been found to enhance the composite's char formation during combustion [30].

The addition of titanium dioxide nanoparticles, carbon nanotubes, nanosilica, and silsesquioxanes materials to composites led to a reduction in flammability compared to pure plastics. This also resulted in improved physical, mechanical, and barrier properties of the composites, showing a significant advantage of nanofillers over traditional flame retardants [23].

Polymer matrices that contain organically modified clay, known as organic-inorganic nanocomposites, have become increasingly popular due to their high efficiency at low concentrations of 5% w/w or less [44]. To improve the flame retardancy of polymers, including polypropylene, various non-compounds such as modified montmorillonites, TiO_2 , Sb_2O_3 , and boroxosiloxanes can be utilized. Among these options, the most used is sodium cation exchanged montmorillonite due to its affordability [45]. However, before it can be dispersed in an organic polymer, the typical sodium cations found in montmorillonite, which is a classic

aluminosilicate material, must be replaced by organophilic cations. This typically involves using an ammonium or phosphonium salt that contains at least one 14-16 carbon alkyl chain. The other substituents on the 'onium' salt can be selected based on the specific properties required for the nanocomposite [46].

1.5.2.5 Inorganic Flame Retardants

Inorganic-based flame retardants are a highly diverse group of materials. They are composed mainly or completely of inorganic substances and contain active elements from the periodic table that are not halogen, phosphorus, mineral filler, or nitrogen-containing. These chemicals offer a wide range of specific flame-retardant capabilities and are commonly combined with other flame retardants to maximize their effectiveness, rather than being utilized independently [36]. Some of mineral fillers are given in Table 2 with their physical properties.

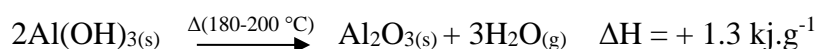
When a non-combustible filler is added to a polymer, its flammability decreases. This occurs because the filler diminishes the amount of fuel in the polymer, slows down the diffusion of oxygen in and out of the polymer, and increases its heat capacity, thermal conductivity, reflectivity, and emissivity. Additionally, the filler may have catalytic or other effects on the polymer's surface and its melt rheology. Some inorganic materials can be decomposed endothermically, generating inert gases or vapor that enhances the fire retardant effect. For this to work effectively, the decomposition must occur within a narrow temperature range above the polymer processing temperature, but at or below its decomposition temperature. Usually, the most effective materials are group II or III carbonates or hydroxides, which have three fire retardant effects in addition to the effects of the inert fillers.

1. Endothermic decomposition absorbs heat and therefore keeps the surrounding polymer cooler, which raises the temperature of the composition to the pyrolysis level, due to the high heat capacity of the fillers.

2. During flaming reactions, a critical concentration of free radicals is required to sustain the reaction. Flame extinction can occur if this concentration falls due to the release of water or carbon dioxide due to dilution of gaseous phase by water vapor-decrease of amount of fuel and oxygen in the flame [32].

3. A layer of inert material builds up on the surface of the decomposing polymer, providing protection against incoming radiation and creating a barrier that prevents oxygen from reaching the fuel, flammable pyrolysis products from reaching the gas phase, and radiant heat from reaching the polymer [35].

An example of this is aluminum hydroxide, which is widely utilized as a fire retardant and often called alumina trihydrate, despite not technically being an alumina or hydrate. Once it undergoes decomposition, it discharges water and produces alumina (Al_2O_3), which effectively diminishes the radicals in the flame by breaking down in an endothermic reaction and generating water vapor. Furthermore, the resulting alumina deposit forms a barrier to provide added protection.



Equation 1. Thermal decomposition of aluminum hydroxide.

It is worth noting that organic polymers have a varying heat capacity range of 0.9 to 2.1 $\text{J K}^{-1}\text{g}^{-1}$ [32]. As a result, the decomposition enthalpy of a fire retardant mineral filler is 1000 times greater than that of 1 g of $\text{Al}(\text{OH})_3$.

Table 2. Some mineral fillers and physical properties[8].

Filler	Formula	T _{decomp} /°C	ΔH _{decomp} /kJ g ⁻¹
Aluminum Hydroxide	Al ₂ O ₃ .3H ₂ O	180-200	1300
Magnesium Hydroxide	Mg(OH) ₂	300-320	1450
Calcium Hydroxide	Ca(OH) ₂	430-450	1150
Nesquehonite	MgCaO.3H ₂ O	70-100	1300
Huntite	Mg ₃ Ca(CO ₃) ₄	400	980
Ultracarb	Hydromagnesite/Huntite	220-400	1172

1.5.2.5.1 Borates as Inorganic Flame Retardants

Boron-based compounds, including zinc borates, calcium borate, melamine borate, boron phosphate, ammonium pentaborate, and borosiloxane, are highly effective in suppressing flames and smoke, reducing afterglow, and preventing tracking in both halogen-containing and halogen-free polymers [47]. This section will specifically focus on the use of boron-based flame retardants in non-halogen polymer systems. Although boric acid and sodium borates are commonly used in cellulosic products, the boron compounds we mentioned above are the preferred choice for flame retardation in plastics and elastomers. Most common boron-based flame retardants are shown in Table 3.

Multifunctional flame retardants based boron compounds provides many useful properties listed below.

- Enhance char/residue formation.
- Form stable char and prevent dripping.
- Inhibit oxidation of the char (afterglow suppression).
- Form stable char by forming glassy barrier.
- Release significant amounts of water to provide flame retardancy.
- Promotes sintering between filler particles.
- Display synergy with nitrogen, phosphorus, silicon compounds in fire test performances.

- Increases suppress smoke and carbon monoxide formation.
- Provide cross-linking between OH groups and thus char formation.
- React with OH group in hydrocarbon and stabilize the alpha-protons.
- Buffer the fire-retardant system and stabilize the package during processing [48].

Boron compounds are used as multifunctional flame-retardant additives in various polymeric materials. They have different modes of flame-retardant action in the condensed and gas phases, depending on the type and amount of boron compound, polymer, and other flame retardant additives. In the condensed phase, char formation increases, and the resulting char is stabilized through physical and chemical routes. This hinders dripping and improves the barrier effect of the char, which also acts as a sintering and fluxing agent. Most inorganic boron compounds decompose endothermically, absorbing heat and releasing water, which are common physical flame-retardant actions in the gas phase [31]. Some organoboron compounds not only act as flame retardants but also inhibit flames and release noncombustible gases instead of water. Furthermore, boron containing additives have diverse action modes, functioning as flame retardants, smoke suppressants, afterglow suppressants, anti-tracking agents, anti-arching agents, and fluxing agents. So, boron compounds are used in commercial applications as flame retardants either alone or in combination with other polymers [49]. Boron compounds are often utilized in commercial applications to enhance the fire resistance of products made from cellulose (like cotton, wood, and paper) and polyvinyl chloride (PVC). They can partially replace antimony trioxide (ATO) or mineral fillers. Additionally, boron compounds can be used as a synergistic filler alongside mineral and phosphorus-based flame retardant additives [50].

Table 3. Most common boron-based flame retardants used in polymers[51].

Chemical Name	Formula (Typical B ₂ O ₃ wt.%)	Starting dehydration temp. (°C)	Water solubility (wt.%, ~25 °C)	Applications
Borax Pentahydrate	Na ₂ O.2B ₂ O ₃ .5H ₂ O (49.0%)	65	4.4	Wood/cellulose/cotton, urethane, coating
Borax Decahydrate	Na ₂ O.2B ₂ O ₃ .10H ₂ O (37.5%)	~45	5.8	Wood/cellulose
Boric Acid	B ₂ O ₃ .3H ₂ O (56.6%)	70	5.5	Wood/cellulose/cotton, urethane, coating, PS foam, phenolic foam
Boric Oxide	B ₂ O ₃ (98.5%)	-	3.1	Engineering plastics
Anhydrous Borax	Na ₂ O.2B ₂ O ₃ (68.8%)	-	3.1	Urethane, wire & cable
Disodium Octaborate Tetrahydrate (Polybor)	Na ₂ O.4B ₂ O ₃ .4H ₂ O (67.3%)	40	97	Wood products, cotton
Calcium Borate	2CaO.3B ₂ O ₃ .5H ₂ O (44-48%)	290	0.2	Rubber modified asphalt, roofing membrane
Zinc Borates Firebrake ZB Firebrake'500 Firebrake'415	2ZnO.3B ₂ O ₃ .3.5H ₂ O (48%) 2ZnO.3B ₂ O ₃ (54%) 4ZnO.3B ₂ O ₃ .H ₂ O (17%)	290 Anhydrous ~415	200 <0.28	Various polymers, elastomers, coatings, sealants/caulking
Ammonium Pentaborate	(NH ₄) ₂ O.4B ₂ O ₃ .4H ₂ O (64.6%)	120	10.9	Epoxy, urethane, coating
Melamine diborate	(C ₃ H ₈ N ₆)O.B ₂ O ₃ .2H ₂ O (22.0%)	130	0.7	Epoxy intumescent coating, cotton textile
Boron Phosphate	BPO ₄ (18.7% as B)	NA	low	PPE/polyamide
Hexagonal Boron Nitride	BN (43.1% as B)	NA	Insoluble	Thermosets, thermoplastics

1.5.2.5.1.1 Zinc Borate (ZnB)

Zinc borate (ZnB) compounds are known to be highly effective in providing fire retardancy for polymers used in a wide range of applications, including electronic products, transportation packages, and buildings. Shen's research indicates that the boric oxide (B_2O_3) component of ZnB plays a key role in suppressing heat and stabilizing the char, while the zinc oxide component promotes its formation. It is worth noting, however, that a substantial amount of ZnB compounds must be used to achieve the desired level of fire retardancy [52, 53].

1.5.2.5.1.2 Ammonium Pentaborate (APB)

APB, also known as ammonium pentaborate, is a highly beneficial additive for thermoplastic polyurethanes. When utilized at levels exceeding 33 weight percent in a non-flame-retardant material, it generates intumescent chars that can withstand high temperatures for prolonged periods. A TPU/APB coating with a thickness of 0.18 cm, when exposed to $800^\circ C$, can offer thermal protection for a duration of 7-10 minutes. Upon thermal decomposition, APB emits considerable quantities of water vapor and ammonia.



In the Decomposition process of APB, given in Equation 2, a boric oxide glass is formed when APB functions as both an inorganic blowing agent and a glass-forming compound. These features contribute to the overall effectiveness of APB [54].

1.5.2.5.1.3 Layered Hexagonal Boron Nitride (h-BN) Flame Retardants

The unique properties of hexagonal boron nitride (h-BN) have garnered significant attention in various fields. With its high-temperature stability, exceptional thermal conductivity, and outstanding chemical inertness, h-BN offers remarkable versatility

[50]. Its stable layered structure also suggests its potential as a rigid barrier to prevent the transfer of decomposed fragments, improving the fire safety of polymers. However, the challenge lies in homogeneously dispersing h-BN nanoplates in a polymer matrix, given its chemically inert surface and strong van der Waals interaction, which can impede the formation of a continuous barrier network [42].

1.5.2.5.1.4 Borax and Boric Acid

A blend of borax and boric acid is a widely used method for fire prevention. When exposed to heat, boric acid undergoes a two-step breakdown process. First, it releases water at temperatures ranging from 130-200°C to form H_3BO_3 , and then again at approximately 265°C to B_2O_3 . This blend dissolves in its own water of hydration, effervesces, and ultimately solidifies into a coating. In a similar manner to phosphoric acids present in phosphate esters, boric acid eliminates oxygen from polymers that contain oxygen, resulting in the creation of a solid residue. This residue, along with the protective coating, protects the substrate from heat and oxygen. Borates are also effective in preventing glowing [55]. Furthermore, Sodium borates, such as Borax Decahydrate ($Na_2O \cdot 2B_2O_3 \cdot 10H_2O$) and Borax Pentahydrate ($Na_2O \cdot 2B_2O_3 \cdot 5H_2O$), are commonly used as flame retardants in cellulose insulation, wood timber, textiles, urethane foam, and coatings. However, their effectiveness is limited to surface flammability due to their low dehydration temperature and water solubility, except for anhydrous sodium borate [49]. While borax pentahydrate and decahydrate can effectively prevent fires in wood and cellulosic materials, they can promote smoldering combustion in cellulose because of the Na_2O component. Therefore, they are often paired with boric acid, an effective smoldering inhibitor, in cellulosic materials and wood products. Combining boric acid and sodium borate can also significantly increase water solubility [31].

1.5.2.5.1.5 Alkaline Earth Metal Borates

Calcium borates with lower dehydration temperatures, such as Calcium Borate ($x\text{CaO}\cdot y\text{B}_2\text{O}_3\cdot z\text{H}_2\text{O}$), have been utilized in fire retardant grade sealants and caulks. The study has been also reported as the use of synthetic calcium borate ($2\text{CaO}\cdot \text{B}_2\text{O}_3\cdot \text{H}_2\text{O}$) in epoxy filled with silica for semiconductor encapsulation. This calcium borate's dehydration temperature falls between 200-400°C [56]. Additionally, calcium metaborate is believed to be advantageous as a fire retardant for fire doors, especially for those based on sodium silicate. It is thought that heating this composition will result in the formation of calcium borosilicate [57].

Magnesium Borate ($x\text{MgO}\cdot y\text{B}_2\text{O}_3\cdot z\text{H}_2\text{O}$) has a unique property where its high charge to size ratio attracts water to its coordination sphere. This means that most synthetic magnesium borates contain non-hydroxyl water, resulting in low dehydration temperatures. However, to be used in plastics, these magnesium borates must be fully or partially pre-dehydrated. Magnesium borates can come in hydrated or dehydrated forms, as they may include crystal waters and/or hydroxyl groups. In Table 4, some common examples of identified magnesium borates and their respective crystal systems [48].

The molecular composition of magnesium borate directly influences its properties [58]. Essentially, magnesium borates are a class of chemical compounds characterized by the presence of borate anions (B(3)-O and B(4)-O) that are coordinated with magnesium atoms, as depicted in Figure 8. By utilizing Fourier-transform infrared spectroscopy (FT-IR), it is possible to discern the symmetric and asymmetric stretching of a given magnesium borate molecule [59].

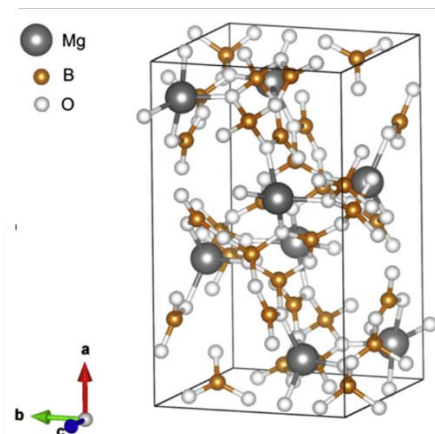


Figure 8. Unit cell representation of Magnesium Tetraborate[60].

Table 4. Hydrated and Anhydrous Magnesium Borate Types[48].

Type	Mineral name	Chemical formula	Crystal system
Hydrated	Admontite	$\text{MgB}_6\text{O}_{10} \cdot 7\text{H}_2\text{O}$	Monoclinic
	Aksaite	$\text{Mg}[\text{B}_6\text{O}_{10}(\text{OH})_6] \cdot 2\text{H}_2\text{O}$	Orthorhombic
	Halurgite	$\text{Mg}_4[\text{B}_8\text{O}_{13}(\text{OH})_2]_2 \cdot 7\text{H}_2\text{O}$	Monoclinic
	Hungchaoite	$\text{MgB}_4\text{O}_7 \cdot 9\text{H}_2\text{O}$	Triclinic
	Hydroxylborite	$\text{Mg}_3(\text{BO}_3)(\text{OH})_3$	Hexagonal
	Inderite	$\text{MgB}_3\text{O}_3(\text{OH})_5 \cdot 5\text{H}_2\text{O}$	Monoclinic
	Kurnakovite	$\text{MgB}_3\text{O}_3(\text{OH})_5 \cdot 5\text{H}_2\text{O}$	Triclinic
	Mcallisterite	$\text{Mg}_2[\text{B}_6\text{O}_7(\text{OH})_6]_2 \cdot 7\text{H}_2\text{O}$	Trigonal
	Pertsevite-(OH)	$\text{Mg}_2(\text{BO}_3)(\text{OH})$	Orthorhombic
	Pinnoite	$\text{Mg}[\text{B}_2\text{O}(\text{OH})_6]$	Tetragonal
	Preobrazhenskite	$\text{Mg}_3\text{B}_{11}\text{O}_{15}(\text{OH})_9$	Orthorhombic
	Szaibelyite	$\text{MgBO}_2(\text{OH})$	Monoclinic
	Wightmanite	$\text{Mg}_5(\text{BO}_3)\text{O}(\text{OH})_2 \cdot 2\text{H}_2\text{O}$	Monoclinic
	Dehydrated	Kotoite	$\text{Mg}_3[\text{BO}_3]_2$
Suanite		$\text{Mg}_2[\text{B}_2\text{O}_5]$	Monoclinic

The thermal properties of magnesium borates are affected by the presence of hydrate groups within the structure. Hydrated magnesium borates undergo a thermal decomposition process that begins with the removal of crystal water ($x\text{H}_2\text{O}$) and continues with the separation of hydroxyl anions (OH^-) as a water molecule in a process called dihydroxylation [61]. As temperature increases, phase changes may also occur. On the other hand, dehydrated magnesium borate is relatively stable and may undergo only phase changes. This stability is likely attributed to high temperature solid state reaction temperature [48].

- Production of Magnesium Borates

When conducting experiments, it is crucial to prioritize cost-effectiveness and minimize the formation of by-products. The experiment's design can be customized to achieve desired particle features, and the synthesis procedures can be classified as liquid-state, solid-state, or hybrid synthesis based on advancements in production technologies. To synthesize magnesium borates using solid-state (thermal) synthesis, raw material powders are mixed without any liquid component, and the reaction of solid powders occurs with the impulsive effect of a temperature increase in high-temperature furnaces. Magnesium hydroxide ($\text{Mg}(\text{OH})_2$) and MgO are commonly preferred magnesium sources for this synthesis method. The reaction usually occurs in an air atmosphere, and the resulting sample is typically in the micron-scale at heterogeneous morphology. The phase diagram of Liu et al. indicates that the reaction commonly occurs at temperatures higher than 800°C [62]. The main drawback of the solid-state synthesis procedure is the requirement of grinding and sieving processes after the reaction. However, Chen et al. eliminated these extra processes of the solid-state synthesis procedure by adding a capping agent of $\text{Ni}(\text{NO}_3)_2$ [63]. Notable combinations of dehydrated magnesium borates include $\text{Mg}_2\text{B}_2\text{O}_7$, MgB_4O_7 , and $\text{Mg}_3\text{B}_4\text{O}_6$ [58].

1.5.2.5.1.6 Nitrogen-Containing Borates

Melamine Diborane, also referred to as melamine borate in the fire retardant industry, is a white powder that can be effortlessly produced by combining melamine and boric acid. It has limited solubility in water and serves as an afterglow suppressant and char promoter in cellulosic materials. According to Shen, a blend of 1:1 ammonium polyphosphate and MB (10-15%) is suitable for phenolic-bound non-woven cotton fibers. MB is commonly employed as a char promoter in intumescent systems for various types of polymers, including polyolefins and elastomers [64]. However, its low dehydration temperature, which is approximately 130°C, makes it unsuitable for use in thermoplastics processed at temperatures above 130°C. Additionally, MB can suppress afterglow combustion in flame-proofing textiles when combined with ammonium polyphosphate or monoammonium phosphate [48].

1.5.2.6 Multicomponent FR Systems

In recent years, flame retardant systems for commercial use have become simpler in terms of composition. They typically consist of a single primary flame retardant, sometimes accompanied by a synergist. Examples of such systems include halogen X, Sb_2O_3 and phosphorus nitrogen systems such as ammonium polyphosphate/melamine. However, there has been a growing trend towards multi-component systems that incorporate three or more flame retardants to further enhance the system's flame retardancy or to address multiple mechanisms at once. In some cases, these combinations are based on proven chemical concepts where various additives work together. For instance, adding a char-enhancing inorganic material to an intumescent formulation. However, in other cases, the combinations used may seem counterintuitive [36].

1.5.2.6.1 Noval Core-Shell Structures of FRs

1.5.2.6.1.1 Organic Microencapsulation by Melamine Formaldehyde

Designers often enhance the efficacy of flame retardants by either developing new ones or incorporating catalysts/synergists into existing systems. Among these methods, core-shell nanoarchitectures have gained popularity as they are key components in advanced materials for catalysis, electrochemistry, optics, and flame retardancy. These materials possess diverse functionalities that can be modified by adjusting their core-shell compositions and other structural properties. Unlike their halogen-based counterparts, halogen-free flame retardants are non-toxic, eco-friendly, and safe for use. As such, researchers are devoting significant efforts to developing effective halogen-free flame retardants for polymeric materials [46].

Microcapsules refer to tiny particles that comprise of core materials wrapped in coatings or shells. These particles come in a range of sizes, from nano- to micrometers. The core materials can be in the form of solids, liquids, or gases, and a broad spectrum of materials can be encapsulated, such as pigments, dyes, monomers, catalysts, curing agents, flame retardants, plasticizers, and nanoparticles, depending on their intended purpose [65].

Microencapsulation is a proven method for protecting substances that are reactive, sensitive, or volatile. This technology involves creating microcapsules of different sizes, ranging from nanometers to micrometers, which create a barrier around the material and prevent its deterioration or volatilization [66]. Melamine-formaldehyde resins, specifically amino resins, are often used for shell material as they are impermeable. In-situ polymerization is the preferred method for creating microcapsules as it results in better mechanical properties and thermal stability, particularly for those with water-immiscible dispersed phases. This technique is frequently mentioned in patent literature [67]. Even though it may not react with the core compound, it can adhere to the core's surface through electrostatic interaction

and combine with melamine to form a shell that covers the surface [68]. This method is incredibly efficient, has a high yield, and is environmentally sound. The core becomes highly effective with excellent thermal stability, while the shell and core together form a synergetic system that provides better flame retardancy than other capsule materials. Furthermore, the synergetic system's decomposition creates a protective layer through an endothermic process, which inhibits oxygen and heat from entering the bulk material. The good compatibility between polymers and MF also helps improve the physical properties of the composites [46].

1.5.2.6.1.2 Inorganic Coating of Flame Retardants

Calcium hydroxyapatite, or HAp, is a ceramic biomaterial with the chemical formula $\text{Ca}_{10}(\text{PO}_4)_6(\text{OH})_2$. This versatile substance has found widespread use in medical and biomaterial applications, from bone grafts to metal orthopedic implants and coating processes [69]. HAp also has the potential to act as a synergistic flame retardant, enhancing the fire resistance of materials. By impeding thermo-oxidation during early stages of degradation, HAp-coated FR composites exhibit improved thermal properties [70].

1.6 Standard Fire Tests to Understand Thermal Degradation Mechanism

1.6.1 TGA, Pyrolysis–GC/MS, TGA-MS and TGA-FTIR analysis

Thermogravimetric analysis (TGA) is a precise method of studying materials, which involves tracking the weight of a small sample of polyurethane (usually 10mg or less) over time or temperature. This provides valuable information on the material's thermal stability and the amount of residue it produces. The analysis can be performed in an atmosphere such as N_2 /helium/argon or in air, O_2 , to assess the material's thermal stability in a neutral atmosphere or its thermo-oxidative stability in an oxidizing atmosphere. TGA experiments can be conducted using isothermal or

non-isothermal (dynamic) weight-loss measurements. Isothermal methods require the polymer sample to be rapidly heated to the desired temperature and held steady for a specific period, while non-isothermal methods involve gradually increasing the sample temperature over time using a programmed linear increase [35]. In addition to the TGA thermogram, to gain a deeper understanding of sample thermal degradation, it is possible to utilize differential thermogravimetric analysis (DTG) in conjunction with TGA thermography. DTG provides insight into the derivative weight loss curve and can assist in determining the temperature at which decomposition begins, the temperature at which decomposition is at its most rapid, the temperature at which decomposition ends, and the number of steps engaged in the degradation process. Each weight loss step corresponds to a peak in the DTG curve, which could be a result of one or several degradation processes taking place within a specific temperature range. Analyzing these peaks may necessitate additional processing of overlapping peaks due to the complexity of the process [5]. The integration of a TGA instrument with an evolved gas analyzer, such as an FTIR or a mass spectrometer, yields a powerful analytical method that offers both thermal balance and compositional data from the spectrometer simultaneously. By utilizing TGA-MS or TGA-FTIR analysis, the detection of volatile products released during thermal degradation is made possible, providing valuable insights into the fundamental nature and mechanism of thermal decomposition [35].

1.6.2 Mass Loss Calorimetry

MLC test is a widely used method for evaluating the fire behavior of materials, particularly fire-retardant polymers. It is considered one of the most advanced methods available. The test apparatus, illustrated in Figure 9, consists of an electric heater, an ignition source, and a gas collection system. The intensity of the applied radiation influences the thermal response of the sample, which is measured by monitoring the concentration of oxygen in the combustion gases. The MLC test yields important information such as ignition time, heat release rate, mass loss,

specific extinction area, ignitability, combustibility, smoke production, and production of toxic gases. The heat intensity applied to the test sample is similar to that of a real fire (25-75 kW/m²), allowing for accurate measurement of its ignition, heat release, and smoke release characteristics. This test enables quantitative analysis of flammability research, providing key measurements such as heat release rate, time to ignition, total heat release, and mass loss rate. Moreover, it can also measure and quantify smoke output, as well as CO/CO₂ release rates with proper configuration. Mass Loss calorimeter tests can be conducted in accordance with national standards international standards including BS 476 (Part 15), ASTM 1356-90, ASTM E1354 and ASTM E1474, ISO 5660[5]. Different types of polymers and polymer composites display distinct burning characteristics, which are discernable from their individual HRR vs. time graph. The configuration of this graph offers valuable information about the material's burning traits. Typical HRR vs. time curve is displayed in Figure 9 [71].

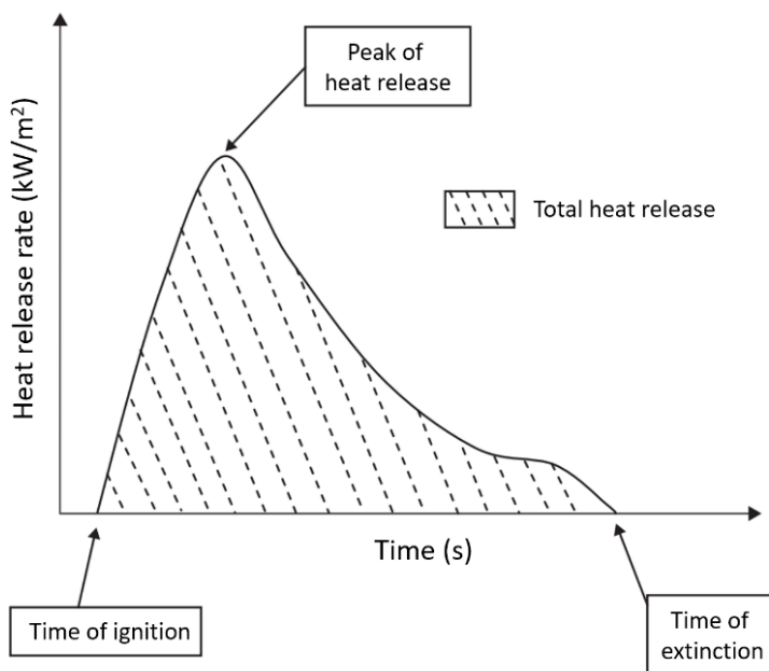


Figure 9. The cone calorimetry (Mass Loss Calorimetry) curve shows key parameters such as time of ignition, extinction, PHRR, and THR[72].

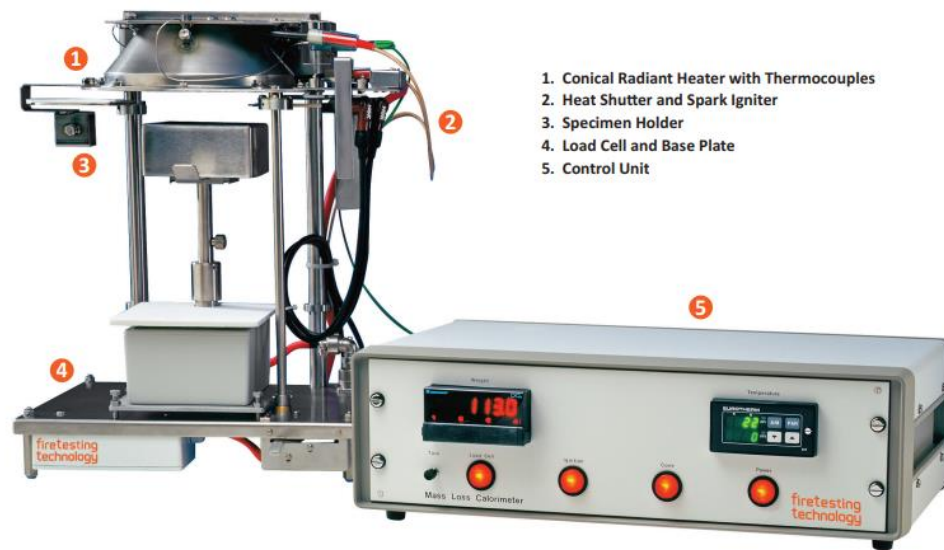


Figure 10. Illustration of typical Mass Loss Cone Calorimeter.

1.6.3 Limiting oxygen index (LOI)

The oxygen index (OI), also known as the limiting oxygen index (LOI), is an effective method of evaluating a material's fire resistance. This metric determines the minimum amount of oxygen required in an oxygen-nitrogen blend to maintain a sample's combustion when set vertically. The experimental set up is shown in Figure 11. A higher OI indicates that the material is more successful in preventing the spread of flames. In summary, the oxygen index is a valuable tool for assessing a material's fire safety capabilities [35].

$$\text{Oxygen Index} = \frac{[O_2]}{[O_2] + [N_2]} \times 100 \quad \text{Equation 3.}$$

Materials with an LOI value lower than 21% are combustible, while those with an LOI value higher than 21% are self-extinguishing due to the air's 21% oxygen content [5].

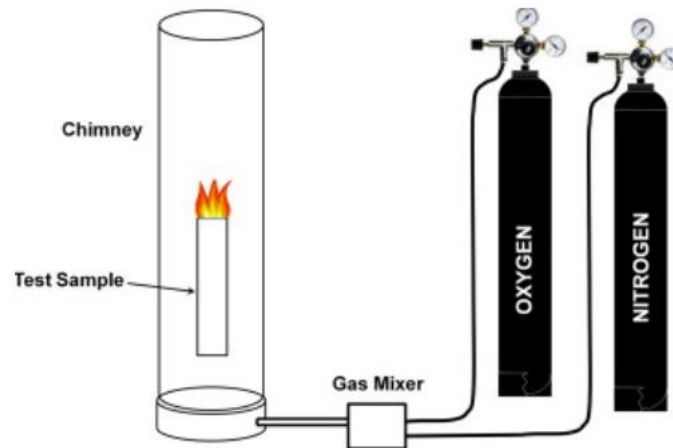


Figure 11. LOI test apparatus.

The LOI test is used to measure a material's susceptibility to fire. It gauges whether a flame can continue burning by vaporizing enough fuel. As oxygen levels decrease, the flame size grows while the amount of heat transferred to the polymer diminishes. Ultimately, the concentration of free radical species that sustain the flame drops below a certain level, causing it to extinguish. This is illustrated in Figure 12, which displays the outcomes for three varying oxygen concentrations. When the test is carried out in high oxygen concentrations, a small, yet intense white flame is noticeable [35].

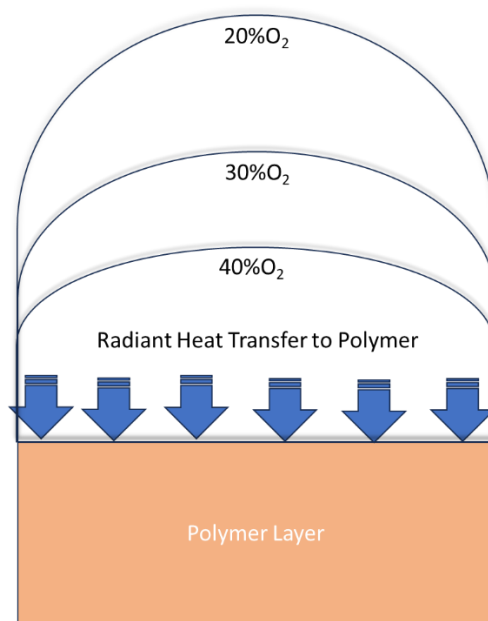


Figure 12. Radiant heat transfer to polymer with oxygen concentration decreasing 40 to 20% [35].

1.6.4 Standard Test Method for Measuring the Comparative Burning Characteristics of Solid Plastics in a Vertical Position (UL-94 V)

Figure 13 shows the UL-94 test scheme. Although the UL 94 vertical test is often considered to be a simple test for flammability, it involves multiple physical processes that interact with one another. The final classification of V-2, V-1, and V-0 does not accurately represent these processes. Since the flame travels upwards, flame dilution is less likely to have an impact than energy absorption through endothermic decomposition or solid phase heat capacity. As a result, most of the heat of combustion is returned to the polymer. Unlike the LOI test, dripping can negatively affect the UL 94 test, as flaming drips can reduce the classification to V-2. However, solid phase fillers and residues can reduce dripping. In order to effectively reduce flammability, endothermic decomposition with the release of water or carbon dioxide must coincide with fuel release during the UL 94 test. Once the first flame has been extinguished, a second 10-second application follows, during

which the heat capacity of the protective residue may contribute the most [35].
 Criteria for UL-94 classification is presented in Table 5.

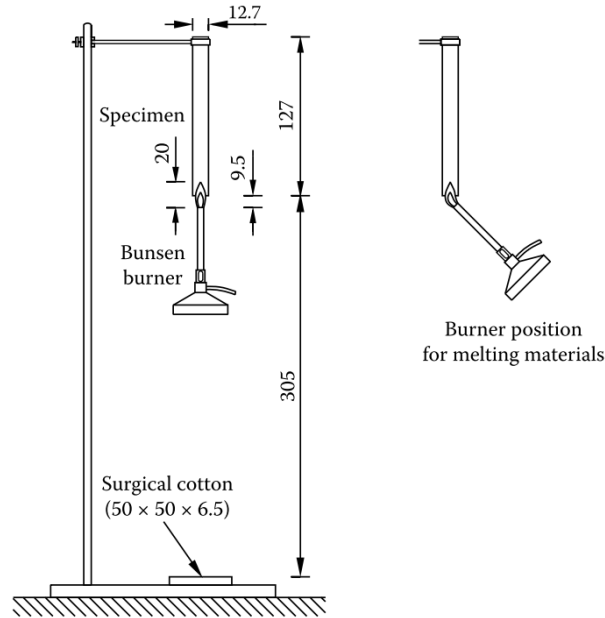


Figure 13. Representation of the UL94 vertical burning test set up [73].

Table 5. Test Criteria for Vertical Burning Classification [73].

Burning Behavior	V0	V1	V2
t_1	<10	<30	<30
t_2	<10	<30	<30
$t_1 + t_2$	<50	<250	<250
$t_2 + t_3$	<30	<60	<60
Cotton ignited by burning drips	No	No	Yes
Afterglow or afterflame up to holding clamps	No	No	No

t_1, t_2 : afterflame time after the first and second flame applications.

CHAPTER 2

AIM OF THE STUDY

Polyurethanes are a versatile class of polymers with a wide range of applications in modern society. However, one of the significant drawbacks of these materials is their high flammability and the emission of toxic gases when burned. Despite the availability of effective fire retardant formulations, many of these are now deemed environmentally unsuitable [74]. Researchers have taken a keen interest in halogen-free flame retardants due to their remarkable features such as low toxicity, low smoke, eco-friendliness, and absence of halogenated fumes upon combustion [75, 61]. In some cases, it may be essential to optimize the multicomponent intumescent system to either decrease the concentration required to achieve the threshold or increase the level of flame retardancy beyond the threshold, depending on the level of flame retardancy desired. The idea of combining flame retardants (FRs), especially those that are nonhalogenated, has gained attraction as a means of enhancing synergistic effects on FR properties. Moreover, reducing the amount of flame-retardant mixture required by incorporating synergists is a key research objective in the field of flame retardancy [76]. As such, numerous synergists have been proposed for intumescent systems used in polymeric materials. Synergistic flame retardancy is achieved through a combination of different modes of action, including flame inhibition and the formation of charring/protective layers in both the gas and condensed phases. This approach is effective due to the complementary nature of these mechanisms, which work together to provide enhanced fire protection [76, 77].

In the literature, numerous combinations can be made with phosphorus, but the P-N synergy, which involves phosphorus and nitrogen, is among the most frequently utilized. By utilizing particular groups of these elements, it is possible to achieve

specific chemical reactions that produce flame retardant effects, such as fuel dilution, charring, and flame inhibition [78]. One instance of combining aluminum diethylphosphinate and melamine cyanurate in polybutylesters can be observed. Similarly, the combination of melamine cyanurate with diphenyl phosphate in thermoplastic polyurethane can also serve as an example [79]. Boric oxide and borates, specifically zinc borate, have been found to be effective synergists in multicomponent systems. In fact, zinc borate is commonly used in conjunction with metal hydrates such as ATH in PU and other polymers to enhance the protective layer properties of fire residue. Studies have shown that the combination of zinc borate and phosphorus flame retardants can result in similar chemical reactions which lead to the formation of an improved protective residual layer. Additionally, melamine borates have been proposed as a potential solution in this regard [51, 53]. The combination of different flame retardant groups in a single flame retardant is considered to be one of the most effective flame retardant synergies, despite being recently proposed as a successful new concept. This practice has been proven to be highly efficient in enhancing the fire resistance of materials and is widely recognized as an essential aspect of flame retardant technology [76].

In this study, it was aimed to investigate non-halogenated multifunctional flame retardant systems, with a particular focus on the use of inorganic flame retardant such as magnesium tetraborate. The high charge to size ratio of the magnesium ion in magnesium borates offers a distinct advantage in this regard. It is worth noting that the Mg^{2+} cation has a pronounced tendency to adsorb water and dehydrate at lower temperatures, typically around 100-200 °C [51]. Firstly, the study investigated the inorganic-inorganic type synergy of HAp coated magnesium tetraborate in PU to increase condensed phase flame retardant efficiency of MTB. Secondly, the proposed inorganic-organic type synergy is Borate-Melamine/Formaldehyde synergism, which could improve flame retardancy of PU. The novel flame retardant, comprising a combination of MF encapsulated MTB, demonstrates promising results in both gas and condensed phases. This innovative solution is a significant step forward in the development of fire safety PUs.

The main motivation of this study is to develop a new flame retardant, MTB-MF, through the microencapsulation of MTB with MF, which is intended to minimize the quantity of FR filler utilized in PU. The combination of melamine-formaldehyde encapsulated MTB serves a dual purpose. Not only does it enhance gas production and fuel dilution, but it also increases melt viscosity in the condensed phase. As a result, this multifunctional FR system boosts the efficiency of MTB as a flame retardant in PU, enabling it to function in both gas and condensed phases. Furthermore, our goal was to create tailored and synergistic multicomponent systems, such as MTB-MF and MTB@HAp-MF, specifically for use in PU.

CHAPTER 3

MATERIALS AND METHODS

3.1 Materials and Chemicals

Boric acid, H_3BO_3 and Magnesium Nitrate Hexahydrate, $Mg(NO_3)_2 \cdot 6H_2O$, purchased from Merck Chemicals with 99.9% purity, used to synthesis Magnesium Tetraborate (MgB_4O_7).

Calcium Nitrate Tetrahydrate, $Ca(NO_3)_2 \cdot 4H_2O$, Diammonium Hydrogen Phosphate, $(NH_4)_2.HPO_4$, and Hexadecyltrimethylammonium bromide, CTAB purchased from Sigma-Aldrich with 99.9% purity, used to produce Hydroxyapatite shell structure on MgB_4O_7 .

Melamine, $C_3H_6N_6$ and 37.0 wt.% formaldehyde aqueous solution, acting as shell-forming monomers on core materials Magnesium Tetraborate and Magnesium Tetraborate coated Hydroxyapatite, purchased from Sigma-Aldrich with 99.9% purity. 25wt% of Ammonia, NH_3 and 70wt % of Nitric Acid, HNO_3 , used to control the pH of solution, were supplied by Sigma Aldrich. Polyvinylpyrrolidone (wt 360,000), PVP, acting as an emulsifier and disintegrant for solution polymerization of Melamine- Formaldehyde, purchased from Sigma Aldrich with analytic grade.

The rigid polyurethane was produced using Adiprene type L-315 elastomer as the isocyanate source (Toluene Diisocyanate) (9-10wt%), supplied by West Coast Polychem Pvt. Ltd, 1,4 Butandiol as the polyol source, supplied by Merck.

3.2 Equipment and Characterization Methods

3.2.1 Powder X-Ray Diffractometer (XRD)

To ensure the purity of synthesized Magnesium Tetraborate, various samples underwent testing using a Rigaku Mini-Flex X-ray powder Diffractometer (XRD) with a Cu-K α line ($\lambda=1,54056 \text{ \AA}$) radiation source. The samples assessed included a Core-Shell structure of Magnesium Tetraborate coated by HAp, M-F Microencapsulated Magnesium Tetraborate, and Magnesium Tetraborate coated by HAp. This analytical technique allowed for the detection and analysis of the crystal structure of the samples, providing valuable information about their composition and purity. Furthermore, the residual chars from PU composites were analyzed by XRD to evaluate flame retardant mechanism.

3.2.2 Fourier Transform Infrared Spectrometer (FT-IR)

Structural characterization of Magnesium Tetraborate (MgB_4O_7), Core/shell structure of Magnesium Tetraborate/Hydroxyapatite and Microencapsulation forms of Magnesium Tetraborate and Magnesium Tetraborate/Hydroxyapatite was performed by Thermo Nicolet iS10 Fourier transform infrared (FTIR) spectrometer. The spectrum was recorded within a wavenumber range of 4000 to 500 cm^{-1} . A total of 32 scans were signal averaged at a resolution of 4 cm^{-1} . The spectra were recorded as percentage transmittance versus wavenumber. The KBr (Potassium Bromide) pellets were used to scan the samples. In a typical experiment, 10 mg of the compound was mixed with about 90 mg of KBr and then finely ground. The KBr pellets were obtained using hydraulic pressure (7–10 psi) for 3 min.

In addition, we conducted FTIR measurement for char residues from cone calorimeter analysis to assess the flame-retardant mechanism of the samples synthesized. In the same way, The FTIR spectrum recorded in the range of 4000 –

500 cm^{-1} equipped with attenuated total reflectance (ATR). Resolution was chosen as 8 cm^{-1} .

3.2.3 Furnace

Protherm furnaces were used to synthesize Magnesium Tetraborate and create a Core/shell structure of Magnesium Tetraborate/Hydroxyapatite. These furnaces can heat samples up to 1500°C while controlling heating rate parameters.

3.2.4 Simultaneous Thermal Analyzer (STA:TGA+DSC)

Thermogravimetry (TG) and Differential scanning Calorimeter (DSC) analyses of synthesized flame retardants and Polyurethane composites were tested by a Netzsch, STA 449 F3 Jupiter under an oxygen atmosphere. The temperature range was 25 to 900 °C, the heating rate was 10°C /min, and the oxygen flow rate was 45 ml/min.

3.2.5 Thermogravimetric Analysis (TGA) coupled with FTIR

Microencapsulated Magnesium Tetraborate, Core/shell structure of Magnesium Tetraborate/Hydroxyapatite flame retardants and Polyurethane composites were undergoing thermogravimetric analysis with TA Instrument, Q500 under Nitrogen atmosphere. The temperature range was 25 to 900 °C, the heating rate was 10°C /min, and the oxygen flow rate was 90 ml/min. Evolved gas during TGA analysis directly measured by Bruker, TENSOR 27 FTIR analyzer. The FTIR spectrum was recorded in the range of 4500–650 cm^{-1} with 64 scan rates.

3.2.6 Scanning Electron Microscopy (SEM)

Thermo Fisher Scientific's Phenom ProX Desktop SEM with EDS scanning electron microscope was used to observe the morphologies of flame-retardant samples (the

microcapsules and Magnesium Tetraborate, Core/shell structure of Magnesium Tetraborate/Hydroxyapatite) and char residues of cone calorimeter analysis.

Before capturing SEM images, the samples are first coated with gold in a vacuum to improve conductivity.

3.2.7 Transmission Electron Microscopy (TEM)

The transmission electron microscope (TEM) operating at 120 kV and the GATAN Orios 2 camera were used to investigate the particle size and morphology of flame-retardant samples with core-shell structure and microencapsulated ones. The particles were suspended in ethanol and prepared for TEM by using ultrasonification. A drop of the suspension was then dried on a carbon-coated copper grid to take pictures.

3.2.8 Mass Loss Calorimeter (MLC)

The fire-retardant performances of the Polyurethane composites (100x100x3 mm³) were analyzed using Mass Loss Calorimeter (MLC, Fire Testing Technology, U.K) under 35 kWm⁻² heat flux according to ISO 13927 standard.

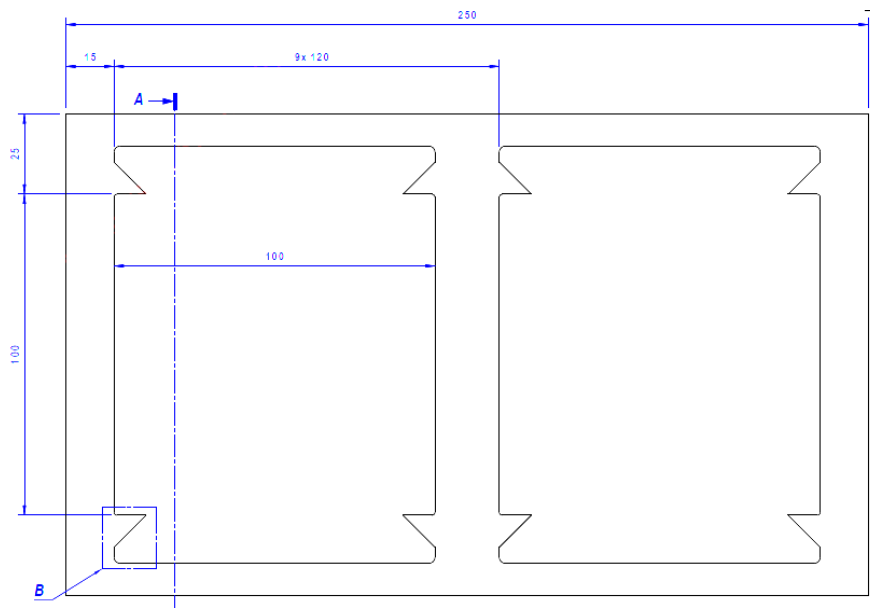


Figure 14. Teflon made Conic Calorimeter test specimen mold.

3.2.9 Standard Test Method for Measuring the Minimum Oxygen Concentration to Support Candle-Like Combustion of Plastics, Limiting Oxygen Index (LOI)

To determine the LOI value, an LOI instrument (Oxygen Index, Fire Testing Technology Limited, England) was utilized. The test bars, which were $130 \times 6.5 \times 3.25 \text{ mm}^3$ in size, were used in accordance with the standard oxygen index test ASTM D2863.

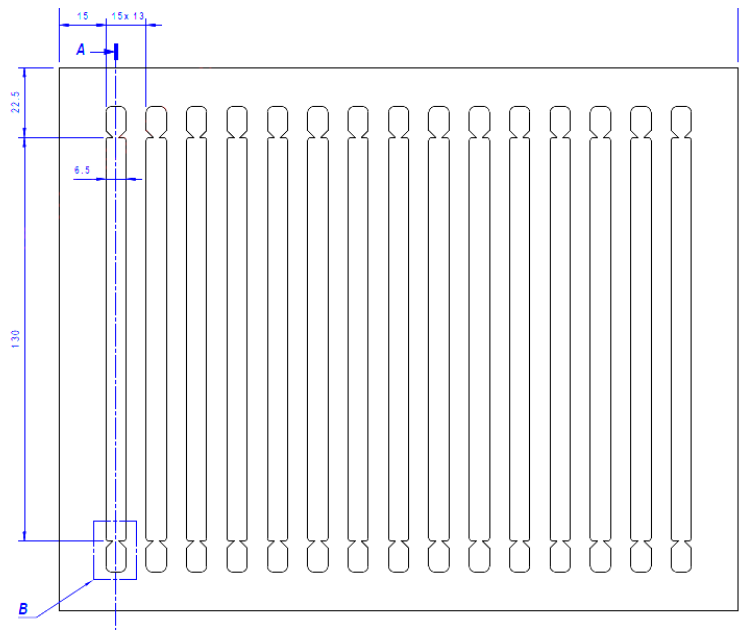


Figure 15. Teflon made LOI specimen mold.

3.2.10 Standard Test Method for Measuring the Comparative Burning Characteristics of Solid Plastics in a Vertical Position (UL-94 V)

This fire-test-response standard covers a small-scale laboratory procedure for determining comparative burning characteristics of solid-plastic material, using a 20-mm (50W) premixed flame applied to the base of specimens held in a vertical position.

The UL-94 rating was determined using ASTM D3801, with V0 being the highest flame retardancy rating and V2 being the lowest. The bar specimens used in testing had dimensions of $130 \times 13 \times 3.25 \text{ mm}^3$.

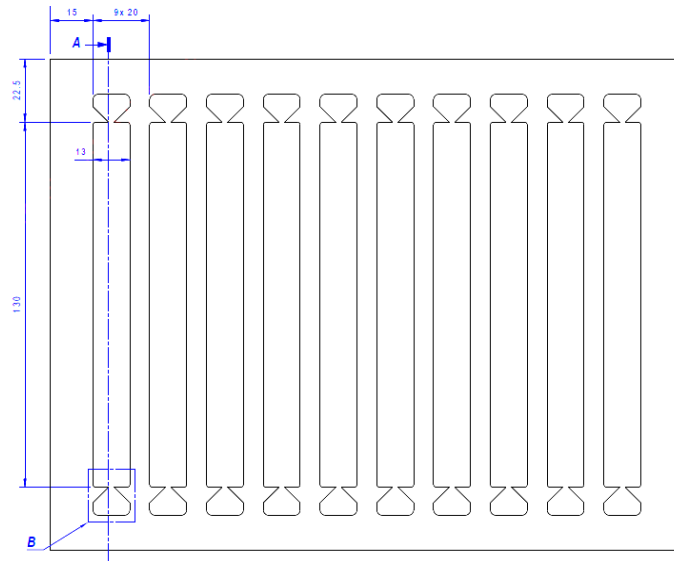


Figure 16. Teflon made Vertical burning test (UL-94V) specimen mold.

3.3 Experimental

3.3.1 Synthesis of Magnesium Tetraborate, (MTB)

MgB₄O₇ (MTB) produced by the solid-state reaction method [80]. Synthesis follows the reaction described below:

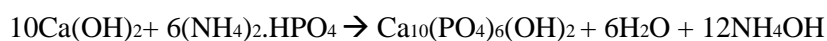


Equation 4. Synthesis reaction for Magnesium Tetraborate.

The reagents utilized for 1 gram of MTB product in this experiment were 2.855 grams of Mg(NO₃)₂·6H₂O and 2.172 grams of H₃BO₃, which were carefully blended to ensure a homogeneous mixture. The resulting mixture was subjected to a sintering process at a temperature of 850 °C for a duration of 3.5 hours. The heating rate employed during the sintering process was 4 °C per minute, and the entire procedure was carried out in atmospheric air.

3.3.2 Synthesis of Magnesium Tetraborate as Core, Hydroxyapatite as Shell Structure (Inorganic-Inorganic Core Shell Model)

Core/shell structure of Magnesium Tetraborate/Hydroxyapatite were synthesized by wet chemical precipitation method according to equation 5. The 1 gram of synthesized MTB were dispersed in 70 mL of 0.06 M calcium nitrate tetrahydrate solution. The pH of the solution was adjusted at 9 with 25% ammonia solution. During this procedure, Ca^{2+} ions initiate their nucleation over MTB surface due to its favorable zeta potential [81]. Next, 50 mL of a 0.07 M di-ammonium hydrogen phosphate solution was gently added dropwise to MTB- Ca^{2+} containing solution. 0.2 g of cetyl trimethyl ammonium bromide (CTAB) was added as surfactant. To maintain the proper stoichiometric ratio of 1.67 of hydroxyapatite, given amounts of calcium chloride and diammonium hydrogen phosphate were dissolved in an aqueous solution. The next step followed by nucleation of PO_4^{3-} ions deposition over Ca^{2+} to form HAp crystals. The whole experimental study was performed at 40°C with pH 9.0. After addition of di-ammonium hydrogen phosphate, the clear solution turns cloudy due to the formation of HAp coating over MTB particles. The mixture was sintered in furnace at 700 °C for 2 h [82, 83, 84, 85].



Equation 5 Synthesis reaction for Hydroxyapatite

3.3.3 Microencapsulation of MTB and MTB/HAp Core Shell

3.3.3.1 Preparation of Microencapsulated MTB with Melamine-Formaldehyde Resin

Microencapsulation of Magnesium Tetraborate with Melamine Formaldehyde was produced through in situ polymerization.

Initially, the synthesis of melamine formaldehyde (MF) prepolymer was carried out using the procedure outlined in Figure 17. 1.0 g of melamine and 5 mL of 37%(w/w)

formaldehyde were mixed in 5 mL of distilled water yielding the prepolymer solution of melamine–formaldehyde (abridged as M–F prepolymer); and resultant mixed solution was adjusted to pH 8.0– 9.0 with 25%(w/w) of NH₃ solution and stirred at 70°C until transparent solution obtained [86].

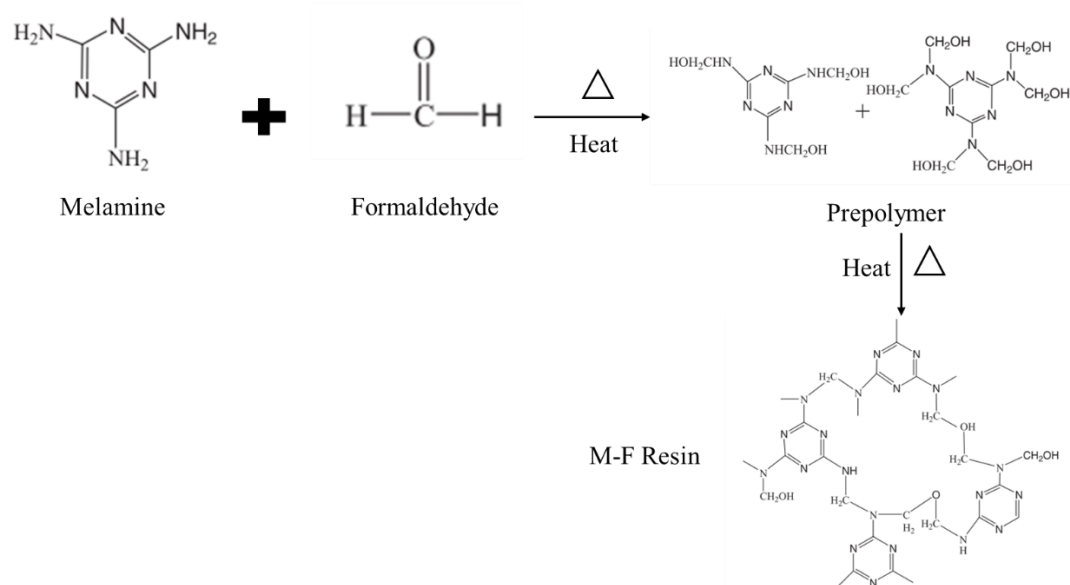


Figure 17. The reaction scheme of the formation of MF prepolymer resin [87, 88].

Microencapsulation of MTB was prepared with synthesized MF prepolymer described in Figure 17. A varying amount of encapsulated MF prepolymer was utilized. MF prepolymer and MTB/HAp ratio is given in Table 6. 1.0 g of MTB, 0.2 g of polyvinylpyrrolidone and 100 mL of distilled water were added to 250 mL three-necked flask and sonicated for 30 min. The pH value of resultant mixed solution was adjusted to 2.0–3.0 with Nitric Acid (HNO₃) acid. The mixture was heated and stirred at 80 °C. Then, prepolymer solution was added dropwise into the flask and continuously. After MF solution was added, 2 ml of 25%(w/w) of NH₃ solution added drop wisely. Upon addition of ammonia solution, formation of precipitates starts in flask. The final mixture was stirred at 70°C for 120 min. The reaction system was filtered, and the filtered cake was separately washed three times with ethanol and distilled water affording wet powders of microencapsulated MTB@MF. The

product was dried at 80 °C in an oven for 24h [86, 87]. Schematic representation of microencapsulation of MTB with MF resin is displayed in Figure 18.

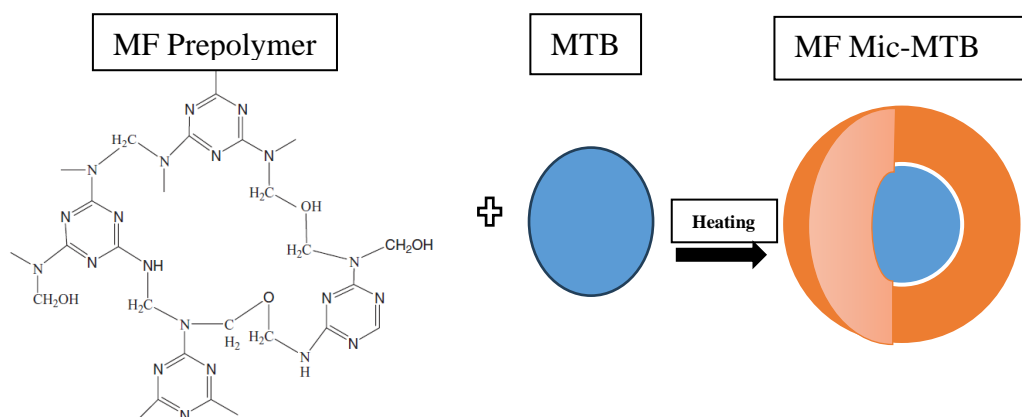


Figure 18. The preparation route of microcapsule with melamine-formaldehyde of MTB.

3.3.3.2 Preparation of Microencapsulation of MTB/HAp Core Shell Structure as Double Shell Microencapsulated MTB

Preparation of MTB@MF microcapsule was carried out based on a previous procedure section. Briefly, MTB/HAp inorganic-inorganic core shell structure was microencapsulated with MF resin. A varying amount of encapsulated MF prepolymer was utilized. MF prepolymer and MTB/HAp ratio is given in Table 6. MF acts as a second organic shell after encapsulation. The MTB/HAp/MF microcapsule was synthesized according to the schematic illustration of the route in Figure 19 [89].

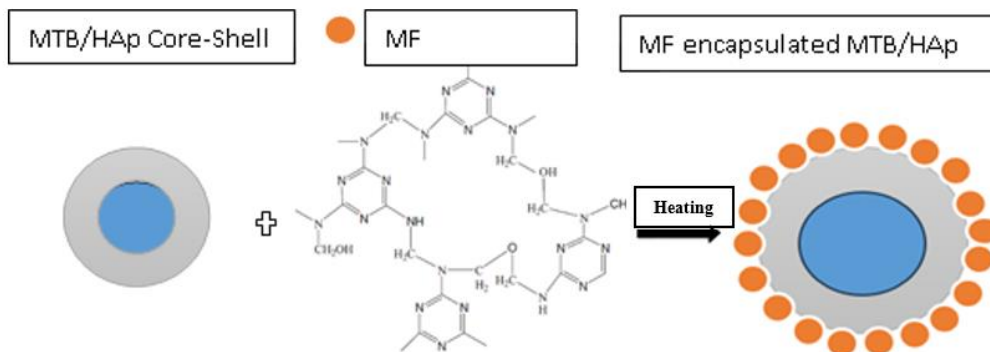


Figure 19. Reaction schematic of surface-microencapsulated MTB/HAp core shell by melamine-formaldehyde resin.

Table 6. A varying amount of encapsulated MF versus Core Materials

Encapsulated Core	Core Ratio (weight)	MF Prepolymer Ratio (weight)
MTB	1	1
MTB	1	2
MTB	1	3
MTB/HAp	1	1
MTB/HAp	1	2
MTB/HAp	1	3

3.3.4 Preparation of Flame Retarded Thermoset Polyurethane Composites

A network of polyurethane was synthesized through the combination of polyol and isocyanate group precursors (NCO) described in Table 7. The source of urethane (prepolymer) utilized was Adiprene L-315, which comprises 9.5 weight percent NCO (toluene diisocyanate, TDI) and polyol (polyether glycol). 1,4 Butandiol was

used as chain extender which increases crosslink density of polyurethane. The reaction equation is as follows (Figure 20).

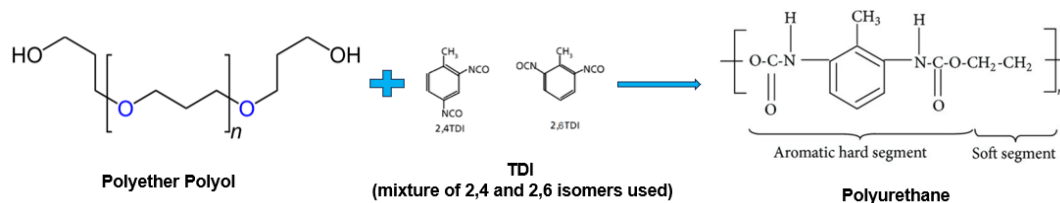


Figure 20. Polyol and Diisocyanate reaction mechanism[5].

To obtain flame retarded polyurethane, the polyol and synthesized flame retardant were put into a 500 mL glass beaker equipped with a mechanical stirrer and a thermometer. The beaker was kept at a temperature of 50 °C and stirred at 80 rpm blade speed for 15min [90].

Table 7. Polyurethane formulation

Component	Parts by Weight
Adiprene L-315	100
1,4-Butandiol	9

3.3.4.1 Polymer Casting Process

Figure 21 illustrates the casting procedure of polymer mixture into a preheated Teflon test (LOI, UL-94 and CC) molds. Viscous polymer mixture is casted into molds and then excess polymer on molds is stripped off to obtain regular specimen dimensions. At the end of the process, polymer containing teflon molds are placed in oven at 70°C for 24 h.

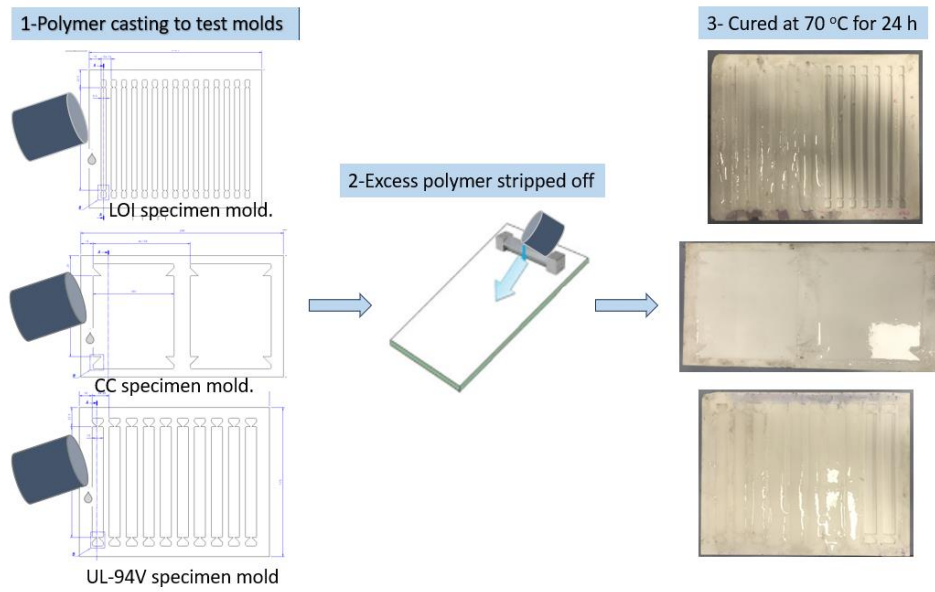


Figure 21. Casting process and curing process of PU test specimens.

In preparing the PU composites, between 5 and 20 parts by weight of MTB and MTB@HAp as FR component were added to 100 parts by weight of the PU. Table 8 describes PU composites with FR types and concentrations by PHR. In addition, MF encapsulated MTB and MTB@HAp were added into PU by 5 PHR. a mixture of MF was incorporated into PU at a ratio of 2.5 PHR to 10 PHR to evaluate its efficiency as a flame retardant.

Table 8. Formulation of flame retarded PU composites.

SAMPLE NAME	FR TYPE	PU	FR PHR
PU	-	100	0
5-MTB-PU	MTB	100	5
10-MTB-PU	MTB	100	10
15-MTB-PU	MTB	100	15
20-MTB-PU	MTB	100	20
5-MTB@HAP-PU	MTB@HAp	100	5
10-MTB@HAP-PU	MTB@HAp	100	10
15-MTB@HAP-PU	MTB@HAp	100	15
20-MTB@HAP-PU	MTB@HAp	100	20
2.5-MF-PU	MF	100	2.5
5-MF-PU	MF	100	5.0
7.5-MF-PU	MF	100	7.5
10-MF-PU	MF	100	10
PU/MTB-MF (1:1)	MTB-MF (1:1)	100	5
PU/MTB-MF (1:3)	MTB-MF (1:3)	100	5
PU/MTB@HAP-MF (1:1)	MTB@HAp-MF (1:1)	100	5
PU/MTB@HAP-MF (1:3)	MTB@HAp-MF (1:3)	100	5

Abbreviations: PHR, Per Hundred Resin, MF; Melamine Formaldehyde Prepolymer, MTB-MF, MTB microcapsuled with melamine formaldehyde; PU, polyurethane; MTB@HAp, Core/Shell structure of Magnesium Tetraborate/Hydroxyappetite, MTB@HAp-MF, Melamine formaldehyde encapsulated MTB@HAp.

CHAPTER 4

RESULTS AND DISCUSSION

In first part, all synthesized compounds, depicted in section 3.3, are characterized to identify phase purity, chemical structure, morphology, particle size and thermal stability with XRD, FTIR, TGA/DTA and Electron Microscopy such as SEM and TEM.

In the second part, thermal and flame retardancy efficiency of PU composites are investigated with flammability tests such as TGA, LOI, UL-94 Vertical Test, and Mass Loss Calorimeter.

In the last part, flame retardancy mechanisms of MTB, MTB@HAp and their Microencapsulated form with MF in PU network are discussed. To understand flame retardancy performance of PU composites, thermal analysis such as TGA and TGA coupled FTIR and char residue analyses, which are XRD and FTIR, after conic calorimeter tests are performed.

4.1 Characterization of Synthesized Flame Retardants

4.1.1 X-Ray Diffraction Analysis

The XRD pattern of MgB_4O_7 is illustrated in Figure 22, MgB_4O_7 is in the orthorhombic phase, coincident with JCPDS Card number 31-0787 given in Figure 22. The crystallographic parameters are $a=13.73 \text{ \AA}$; $b=7.97 \text{ \AA}$; $c=8.62 \text{ \AA}$; $\alpha=90^\circ$; $\beta=90^\circ$, corresponding to magnesium tetraborate (MgB_4O_7). Based on the XRD analysis, it has been confirmed that most of the phase is MgB_4O_7 . This indicates a higher efficiency of solid-state reaction [80].

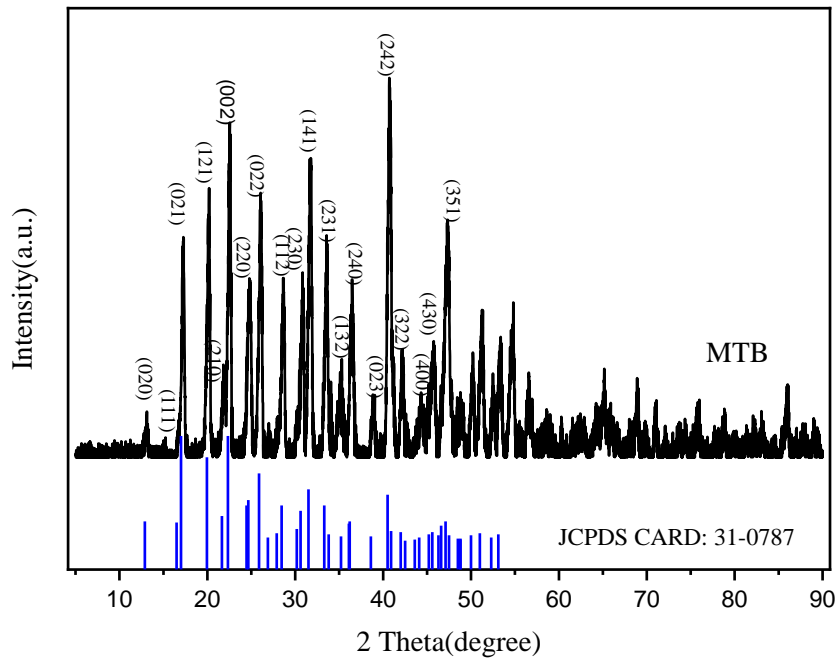


Figure 22. XRD Pattern of Synthesized Magnesium Tetraborate and JCPDS Card:31-0787 lines.

Once MgB_4O_7 was obtained purely, core shell structure of MTB@HAp was synthesized with solution precipitation synthesis method. Figure 23 presents the experimental data for MgB_4O_7 @HAp synthesis. The core is MTB, and it is surrounded by a shell of hydroxyapatite (HAp) coating. The majority of the XRD phase can be attributed to the presence of HAp in the analyzed material, which is a result of its core-shell structure. In Figure 23, the XRD pattern of pure MTB was added for comparison, characteristic peaks of MTB were not detected in XRD pattern. Namely, the major peaks of the MTB are suppressed, which demonstrates that the pure MTB is covered with HAp shell. Thus, the existence of crystal phases within the product signifies that the process of HAp crystal mineralization was accomplished with success.

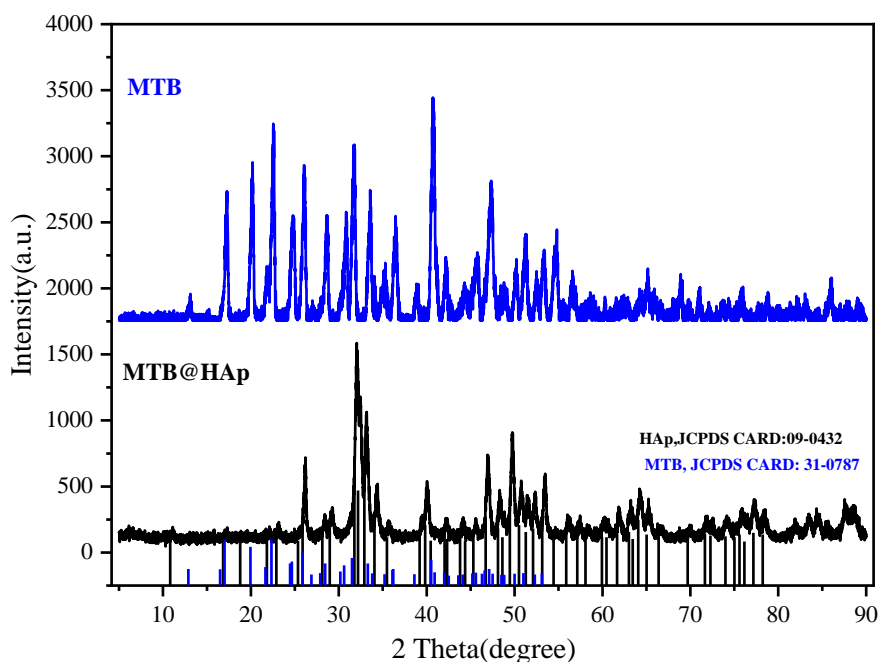


Figure 23. XRD patterns of MgB_4O_7 denoted as MTB, and Core/Shell structure of MgB_4O_7 @HAp denoted as MTB@HAp.

Figure 24 displays the XRD patterns of both MTB and microencapsulated MTB at varying weight ratios of Melamine-Formaldehyde (MF) resin. The X-ray diffraction (XRD) patterns of the MTB-MF sample provide evidence that the crystallinity of MTB decreased as the ratio of MF increases. This phenomenon can be attributed to the polymeric structure of MF. Upon comparing MTB to MTB/MF (1:1). This ratio indicates a significant change in the crystallinity of MTB, leading to a more amorphous structure. Thus, MTB particles are completely encapsulated by MF resin.

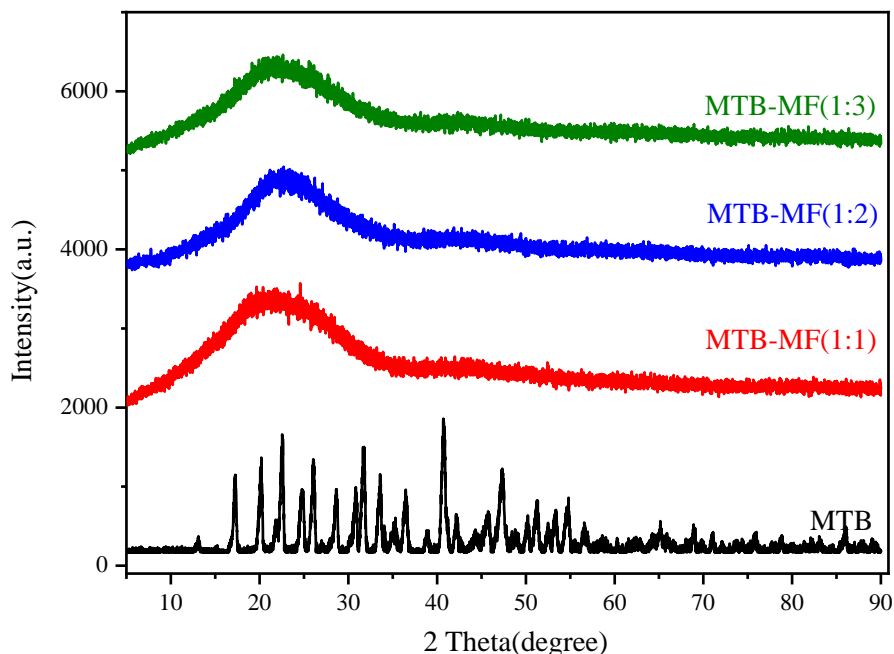


Figure 24. XRD Patterns of Microencapsulated MTB with Melamine-Formaldehyde Resin.

Once the core shell structure of MTB@HAp was ensured according to XRD pattern in Figure 23, more melamine formaldehyde resin was used to encapsulate as double shell for MTB core. XRD patterns of double shell structure are given in Figure 25. MF as second shell decreased the crystallinity of MTB@HAp. Regarding the MTB@HAp sample with a 1:3 ratio encapsulation, it is noteworthy that although the XRD pattern's majority phase is amorphous. In XRD pattern, marked peaks denoted as + represents HAp, the peaks of Calcium Hydrogen Phosphate diffraction marked as *. During the microencapsulation reaction, a slightly basic medium with a pH of less than 9.8 might cause the formation of Brushite, which is Calcium Phosphate (whitelockite) that dissociates from HAp [91]. Besides, it is evident that whitelockite formation and HAp occur in MF ratios of 1:1 and 1:3 containing microcapsules. This is due to the insufficient deposition of MF on MTB@HAp.

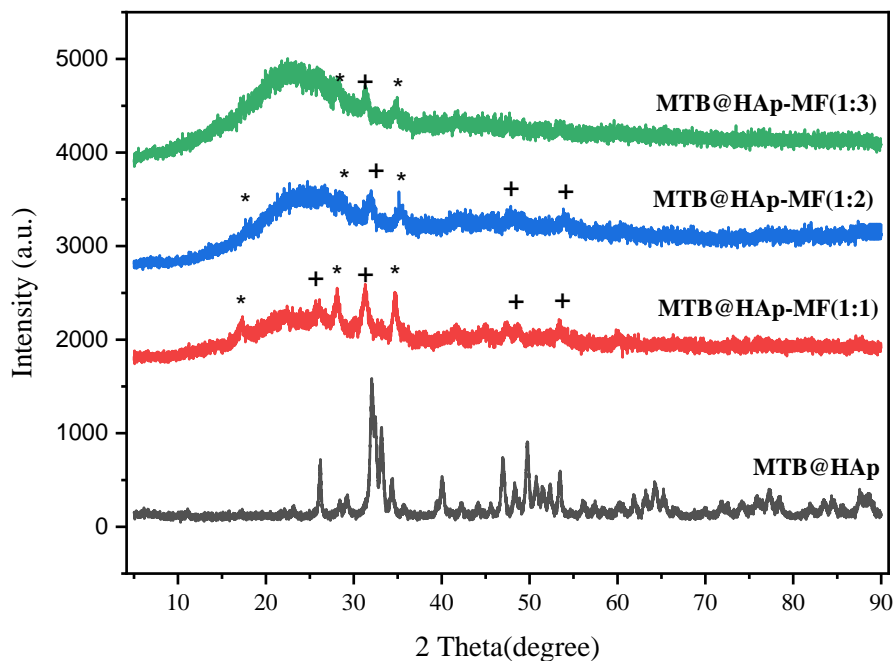


Figure 25. XRD Patterns of Microencapsulated MTB@HAp with Melamine-Formaldehyde Resin.

4.1.2 FTIR Analysis

Vibrational spectroscopy is a significant method to comprehend chemical bonding and can offer valuable insight that can aid in the empirical assessment of core-shell structures. Figure 26 shows FTIR spectra of MTB, HAp, and MTB@HAp core-shell structure. The MTB spectrum indicates bands at 1432 cm^{-1} , 1344 cm^{-1} , and 1258 cm^{-1} that are attributed with the asymmetric stretching of the B-O bond in BO_3 [58]. The band at 1100 cm^{-1} is due to asymmetric stretching of B-O bond in BO_4 . The bands at 990 cm^{-1} and 830 cm^{-1} are attributed to the symmetric stretching of B-O in BO_3 and BO_4 respectively. Out-of plane bending of B-O in BO_3 is detected at 710 cm^{-1} . Finally, the bands at 454 cm^{-1} and 580 cm^{-1} are due to O-B-O ring bending in the structure [92]. FTIR spectrum proves that the HA was synthesized successfully.

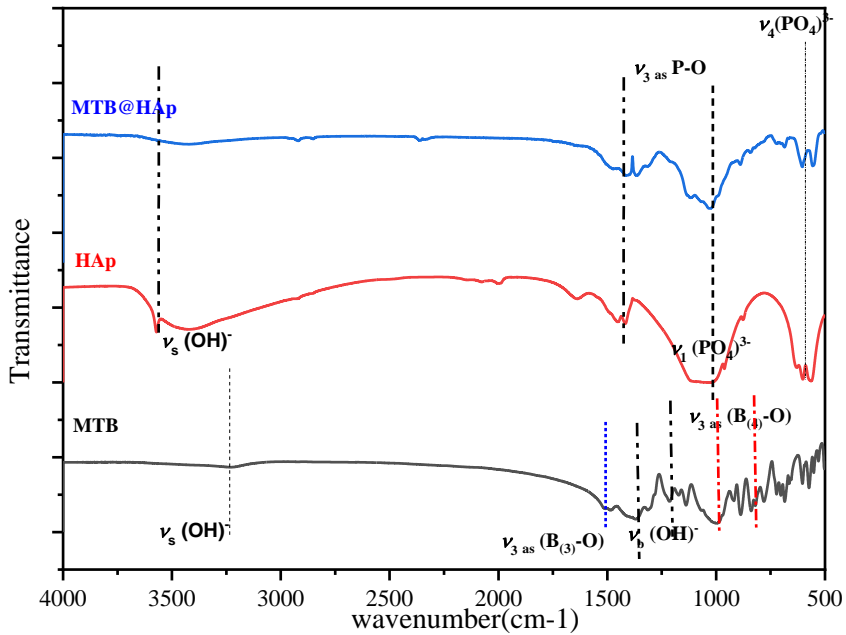


Figure 26. FTIR spectra of synthesized MTB, HAp and MTB@HAp.

HAp was utilized as shell for MTB core. Pure FTIR spectrum of HAp is given in Figure 26 to compare the FTIR spectrum of MTB@HAp core-shell structure. The peaks at 3500 cm^{-1} are attributed to -OH stretching mode in crystal structure of HAp, which is not obvious because of overlapping with OH absorption peak of water. The absorption bands of the apatite phase are characterized by peaks at 590 cm^{-1} , 1025 cm^{-1} , and 1200 cm^{-1} . These peaks correspond to the bending of O-P-O and the asymmetric stretching of PO_4^{3-} ions [82, 81]. Therefore, HAp was coated successfully as shell according to FTIR spectrum of MTB@HAp sample.

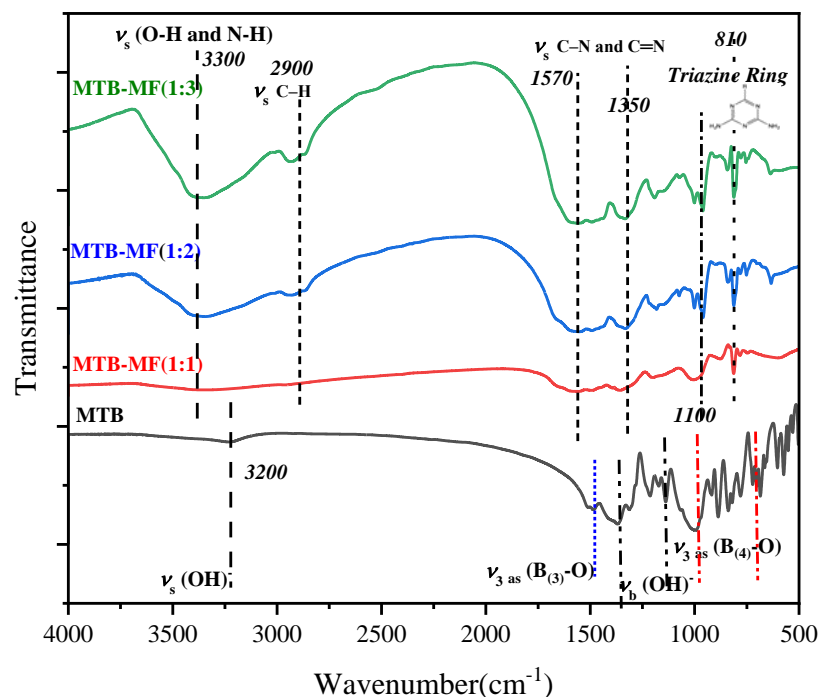


Figure 27. FTIR Spectra of MTB and Microencapsulated MTB with MF.

FTIR spectra of MTB and Mic-MTB-MF are given in Figure 27. The vibrational bands of MTB in Figure 26 are completely different from the MF microcapsules. MF encapsulated MTB samples show their own characteristic vibrational bands. FTIR spectra of microcapsules show that vibrational band at 3300 cm^{-1} was the stretching vibration peak of the secondary amino group N-H [86]. The 2900 cm^{-1} is attributed to the symmetrical and antisymmetric stretching absorption of methylene C-H. The peak positions of 1570 cm^{-1} , 1509 cm^{-1} , 1373 cm^{-1} and 810 cm^{-1} were the characteristic absorption bands of triazine ring. This result indicated that MF resin encapsulated MTB core [93].

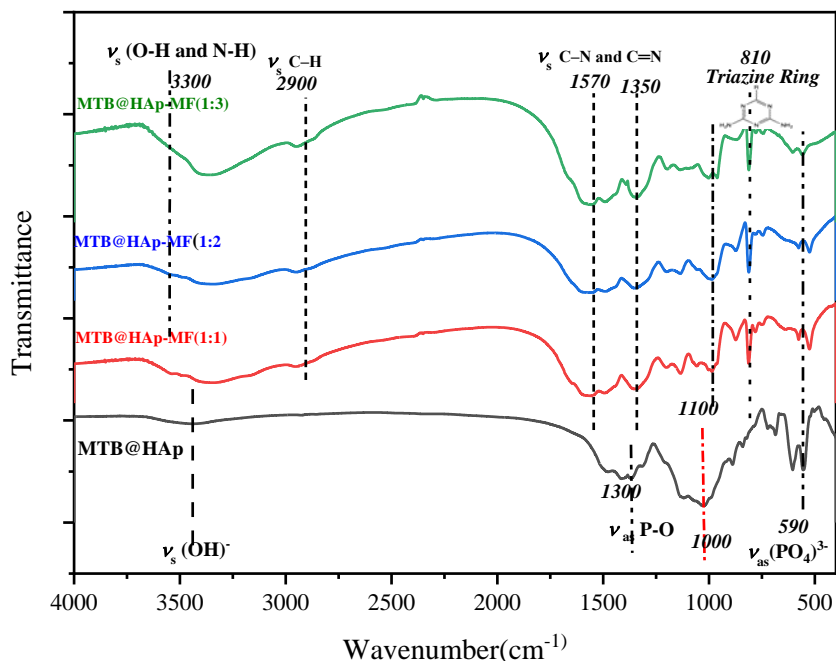


Figure 28. FTIR spectra of MTB@HAp and Microencapsulated MTB@HAp with MF.

FTIR spectra of MTB@HAp-MF microcapsules are shown in Figure 28. Likewise, FTIR spectra of MTB encapsulated with MF (Figure 27), there is a peak around 3300 cm^{-1} , which was assigned to N–H and O–H stretching vibration. A peak at 1570 cm^{-1} , which was assigned to C–N stretching vibration. There was a peak at 810 cm^{-1} , which was ascribed to triazine ring stretching vibration [86]. Compared with the FTIR spectrum of MTB@HAp core-shell with microcapsules, the characteristic asymmetric P–O vibrations of O–P–O bonds in PO_4^{3-} was observed [81]. As the MF ratio on the core structure increases, the vibrational absorption bands become more noticeable in intensity. This result indicated that MF resin had appeared in the MTB@HAp-MF microcapsule.

4.1.3 Scanning Electron Microscopy (SEM)-Energy Dispersive X-Ray Spectroscopy (EDS) Analysis

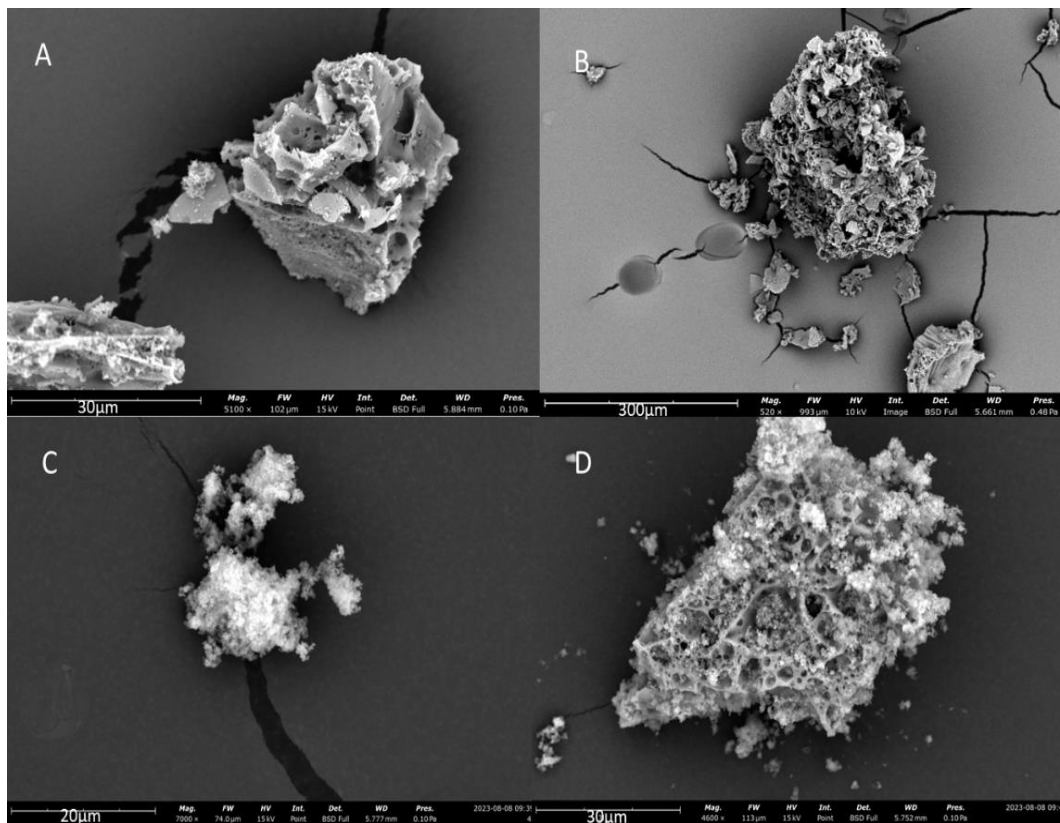


Figure 29. SEM micrographs of MTB and MTB@HAp; a- MTB-Overview, b- MTB-close view, c- MTB@HAp-overview, d- MTB@HAp-close view.

SEM micrograms of synthesized MTB and MTB@HAp core-shell are illustrated in Figure 29. SEM micrograph analysis was used to determine surface morphology of synthesized MTB and HAp coated MTB. The surface of MTB is porous, and particles are not uniform and MTB structure is proved by EDS analysis of MTB given in Figure 30. HAp is deposited on surface of MTB particles, which is demonstrated by SEM images and EDS analysis given in Figure 31. The EDS analysis was conducted multiple times on various spots of the sample. Mg, B and O element from MTB core and Ca, P, O elements from HAp as shell were observed

and weight ratios in the structure is given in Figure 31. The EDS analysis confirmed that the MTB@HAp core shell structure with deposited HAp was successfully obtained.

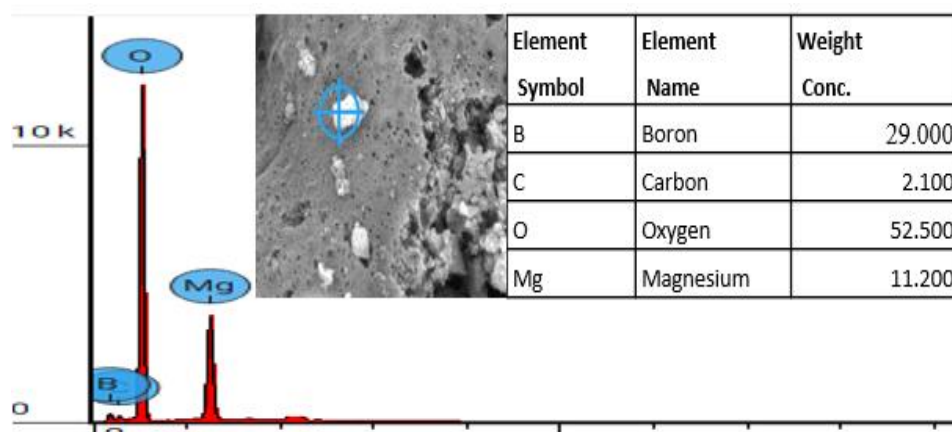


Figure 30. EDS analysis of MTB and detected elements.

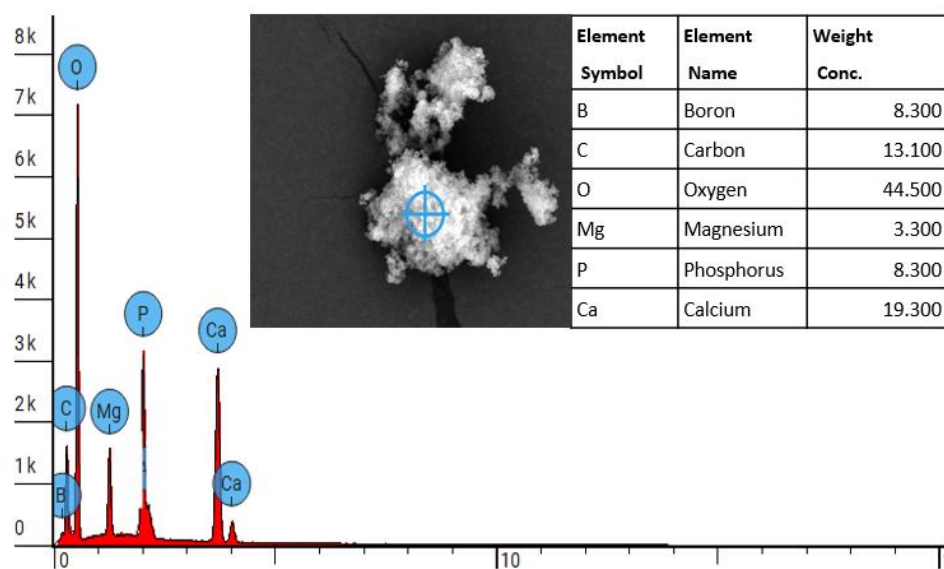


Figure 31. EDS analysis of MTB@HAp and detected elements.

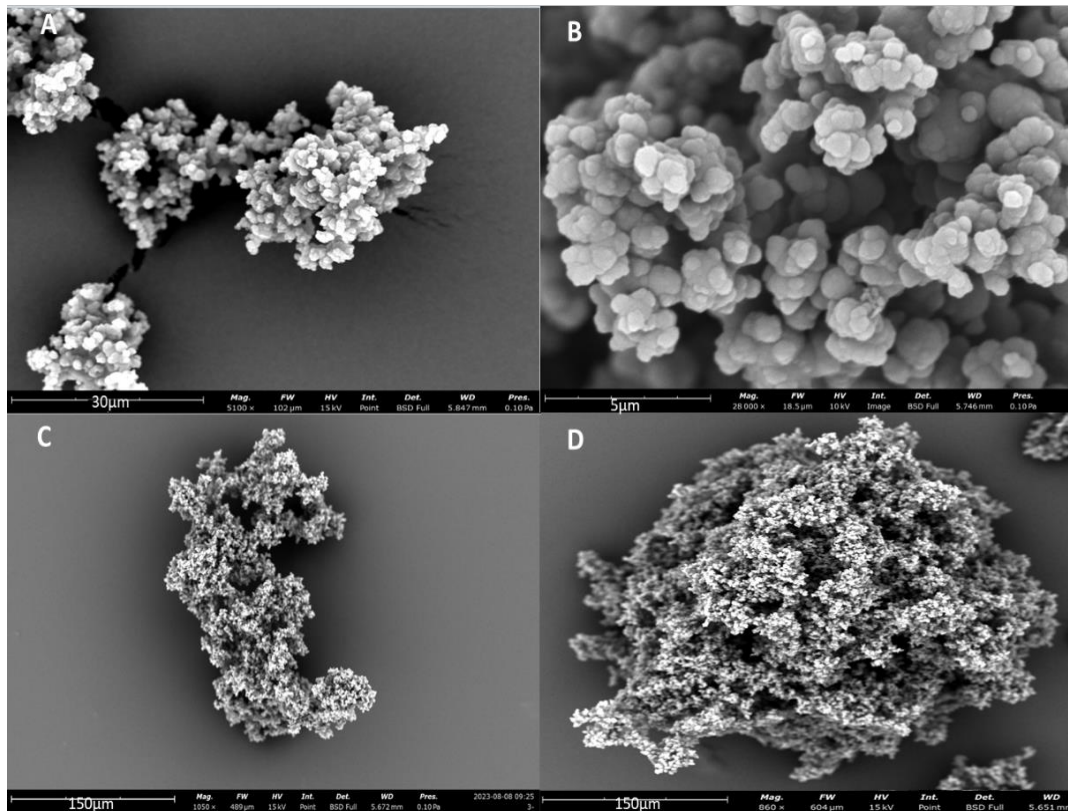


Figure 32. SEM micrographs of Microencapsulated MTB with MF resin, a-b, MF ratio 1:1, c-d, MF ratio 1:3.

Figure 32 shows the surface morphologies of MF with 1:1 and 1:3 ratio capsulated MTB. Surface morphology of MTB changed drastically. MTB presents a comparably rough surface. After microencapsulation, the surface of MTB-MF is very smooth and spherical. However, the size of the spheres are not uniform due to conglomeration [86]. When MF ratio increased to 1:3, the size of spheres becomes more uniform than MF ratio 1:1 microcapsule. Encapsulation of MF was analyzed with EDS to confirm the MF layer over MTB. EDS analyses shown in Figure 33 and Figure 34, C and N weight ratio increases with increasing MF layer. The Carbon ratio showed a slight increase from 20.7% to 21.1%. This may be attributed to the measurement being performed on carbon tape, which increased the base carbon percentage during analysis.

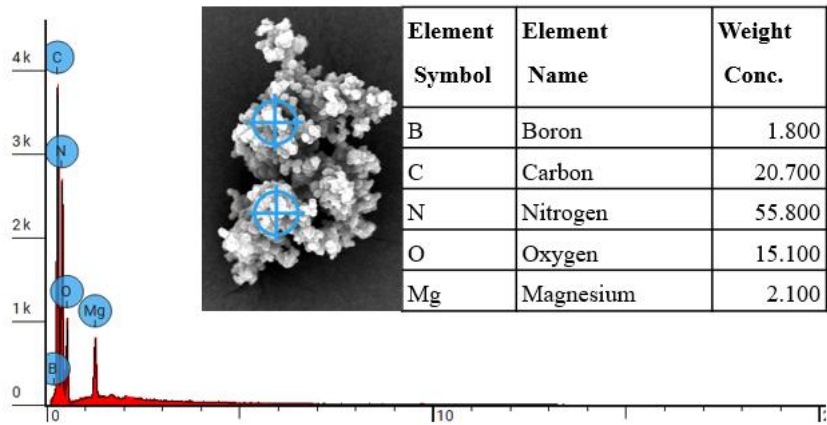


Figure 33. EDS analysis of Microencapsulated MTB with 1:1 MF and detected elements.

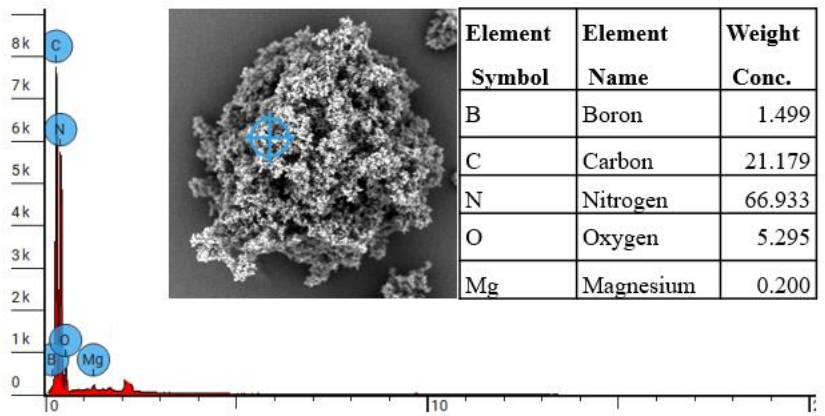


Figure 34. EDS analysis of Microencapsulated MTB with 1:3 MF and detected elements.

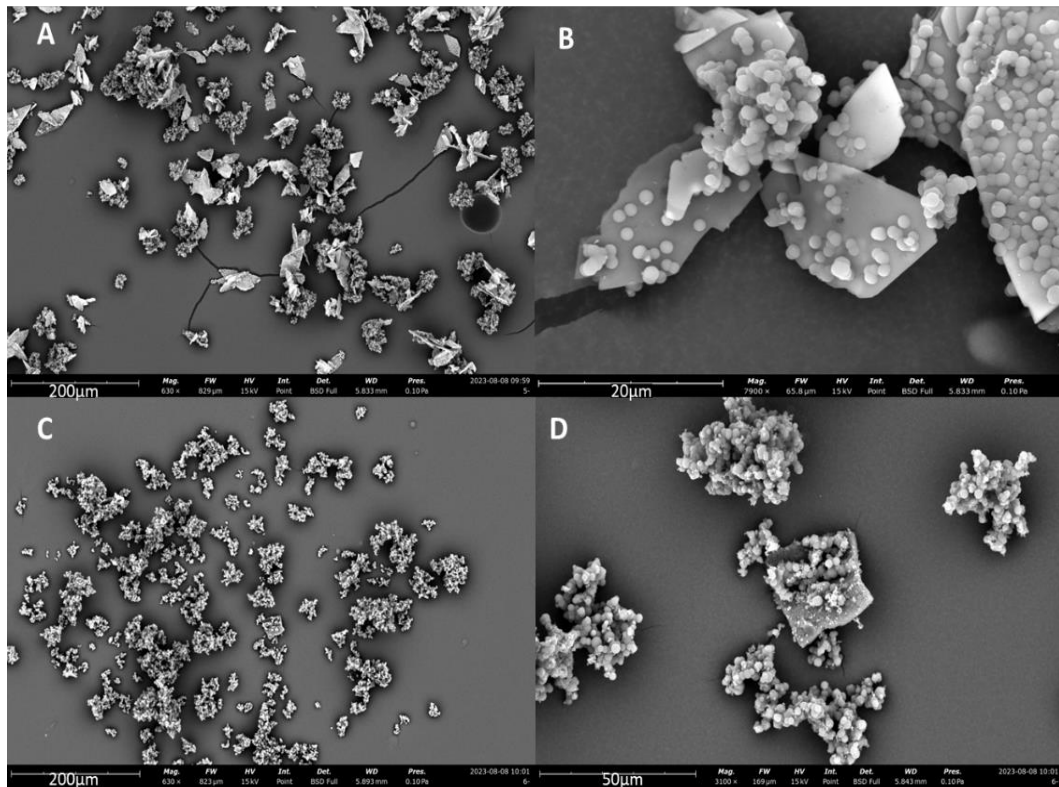


Figure 35. SEM micrographs of Microencapsulated MTB@HAp with MF resin, a-b, MF ratio 1:1, c-d, MF ratio 1:3.

The morphology of microencapsulated MTB@HAp with MF resin is investigated with SEM technique. Figure 35 shows the SEM micrograms of microcapsules. After MF encapsulation of MTB@HAp, it could be seen that the surface morphology of the particles had changed progressively. The surface of MTB@HAp is coated by MF microcapsule. MTB@HAp particles act as host to deposition of MF microcapsules. Covered surface area of MTB@HAp increased with increasing MF ratio from 1:1 to 1:3, which is supported by EDS elemental analysis given in Figure 36 and Figure 37. The nitrogen amount in microcapsule referring to MF layer increased from 11.8% to 57.5%. This result demonstrates that MF deposits on the surface of core structure.

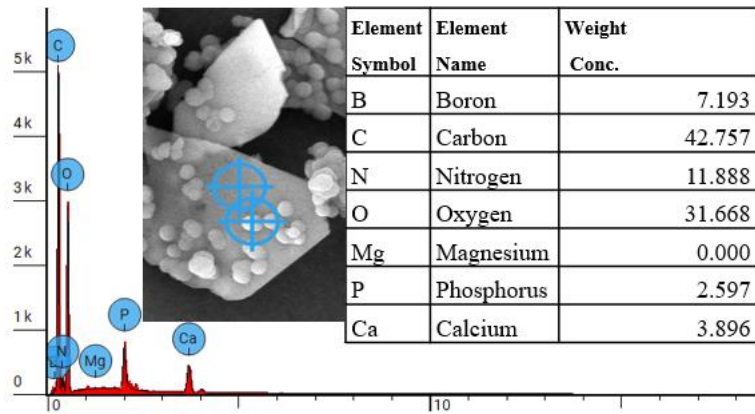


Figure 36. EDS analysis of Microencapsulated MTB@HAp with 1:1 MF and detected elements.

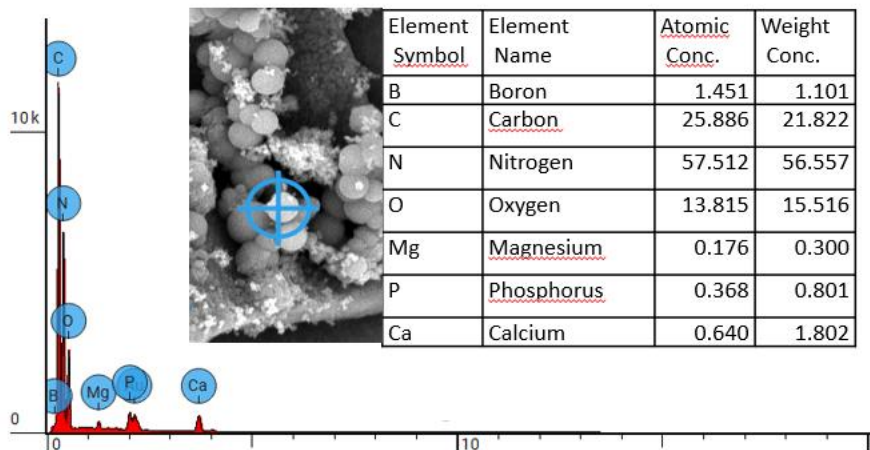


Figure 37. EDS analysis of Microencapsulated MTB@HAp with 1:3 MF and detected elements.

4.1.4 Transmission Electron Microscopy (TEM) Analysis

Figure 38 showed TEM morphology of MTB and Figure 39 showed images of HAp coated MTB (MTB@HAp). The size of MTB observed from TEM images is 400-500 nm and the particles are tending to agglomerate. The morphology of MTB particles is uniform even if they are merged spheres. From Figure 39, we can find

that the size of HAp coated MTB particles increased obviously. Moreover, the sphere shape of the particles became distorted due to the deposition of HAp particles of MTB core. While the darker side represents the core, the clear side over the core is due to the HAp deposition. It implies that core-shell structure of MTB@HAp was achieved.

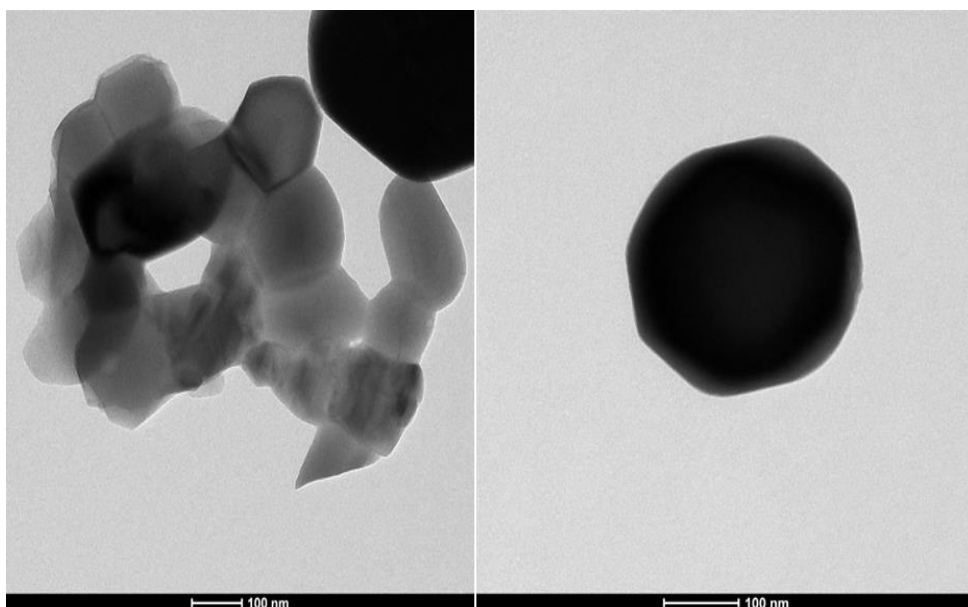


Figure 38. TEM images of synthesized MTB.

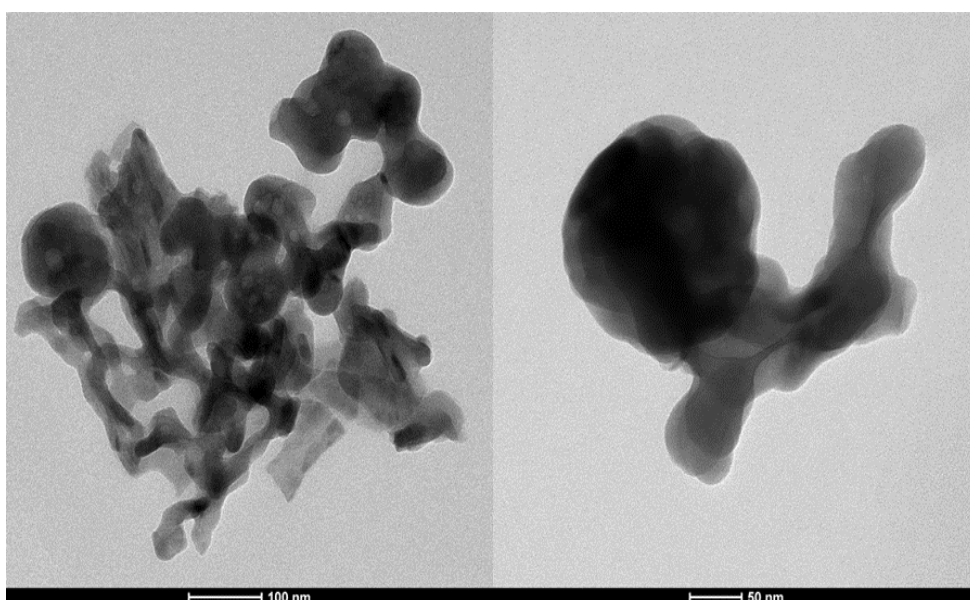


Figure 39. TEM images of synthesized MTB@HAp.

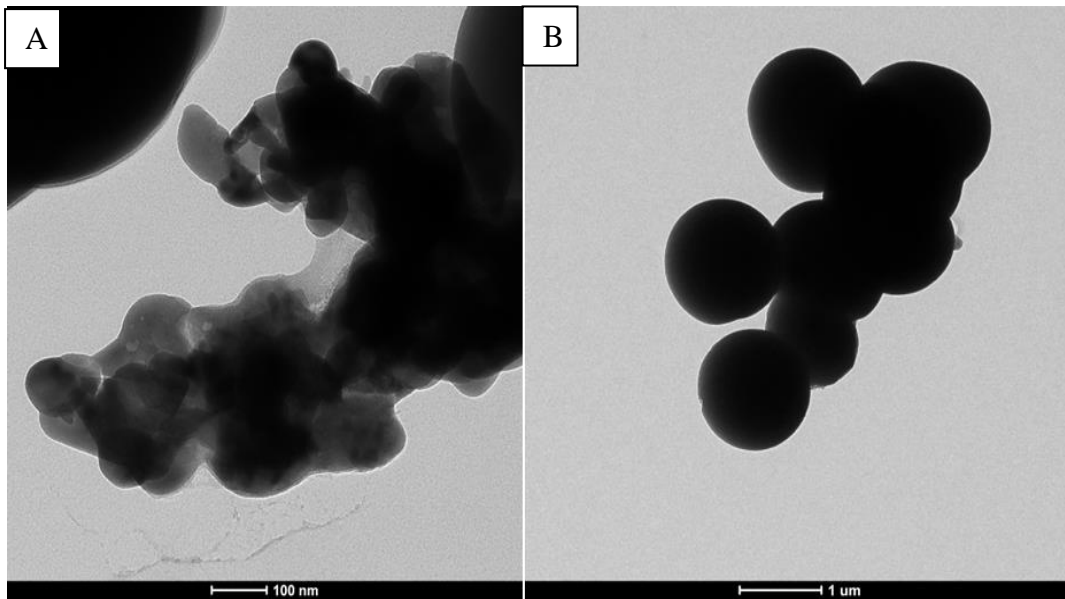


Figure 40. TEM images of synthesized MTB-MF microcapsules, A: MTB-MF-1:1, B: MTB-MF-1:3.

Figure 40(A) reveals that TEM images of melamine formaldehyde resin microencapsulated MTB samples. For the MF ratio 1:1, the particles are aggregated and not uniform size distribution. Figure 40(B) shows morphology of MTB-MF microcapsules (the mass ratio of 1:3), which exhibited not only regular spheres and well-dispersed morphology, but also the average diameter was about 700 nm–900 nm and a uniform size distribution. Figure 41(A) shows the morphology of MTB@HAp-MF samples. The particles of MTB@HAp-MF microcapsules (the mass ratio of MTB@HAp:MF, 1:1) are aggregated and the shapes of the particles are not regular. It is obvious that microencapsulation with MF increased the particle size MTB@HAp. Moreover, microencapsulation made the shape more spherical. Figure 41(B) illustrated the effects of mass ratio of MF on MTB@HAp-MF morphology. It can be seen that the particle size of MTB@HAp-MF increased with increasing MF ratio. Furthermore, unreacted MF resin prepolymers are attached to microencapsulated MTB@HAp-MF spheres, which is supported by SEM-EDS elemental analysis. Nonuniform particles were analyzed to determine microcapsule

structure. Analyzed points show that the particles consist of carbon, nitrogen, and oxygen, which demonstrates the unreacted MF existence.

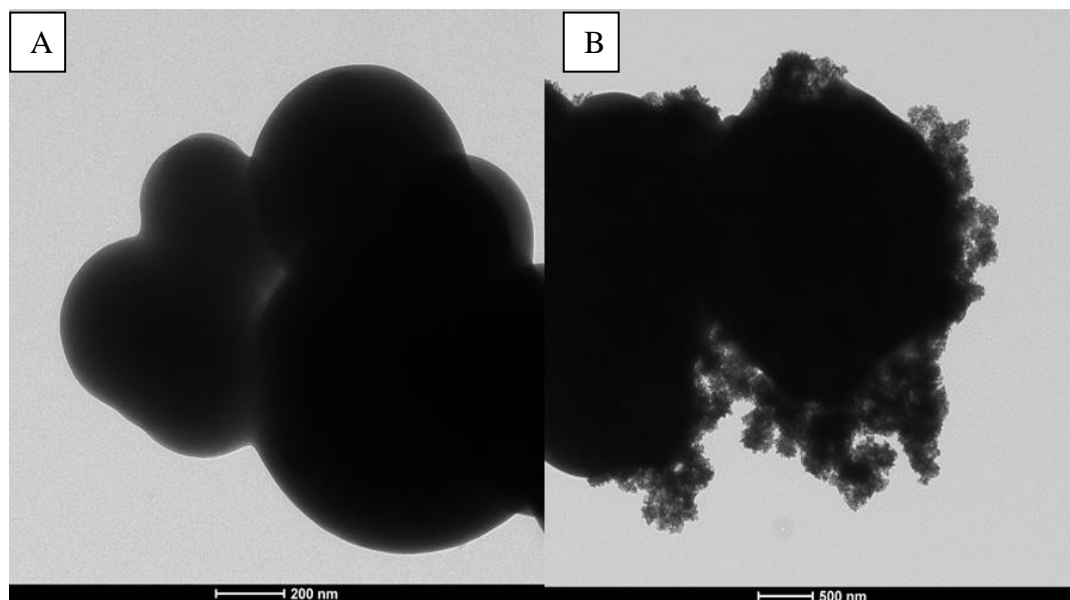


Figure 41. TEM images of synthesized MTB@HAp-MF microcapsules, A:MTB@HAp-MF-1:1, B: MTB@HAp-MF-1:3.

4.1.5 Thermal Analysis of Synthesized Flame Retardants

DSC/TG curves of the MTB produced by S.S are shown in Figure 42. The DSC (red line) represents chemical and physical changes in the samples structures during the temperature rising. The TG (blue dash line) records changes in the samples mass along of this process.

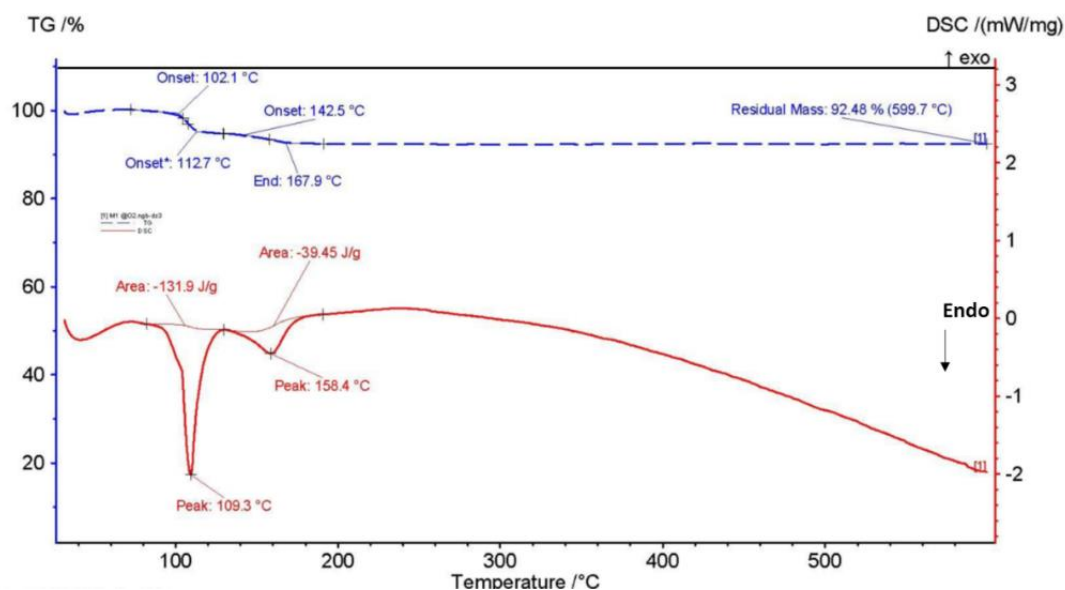


Figure 42. TGA and DSC curves of MTB.

The DSC curve shows two peaks of endothermic activity at approximately 109 °C and 158 °C. Endothermic peak at 109 °C shows that 131.9 J/g heat absorbed while the smaller peak at 158 °C absorbed 40 J/g. These peaks are accompanied by mass losses of around 10% and 3%, respectively in TGA curve. These endotherms are associated with the decomposition of adsorbed water molecules [94, 58]. Beyond the temperature 160 °C, there is no significant mass loss in TGA curve and endothermic/exothermic phase transition and decomposition.

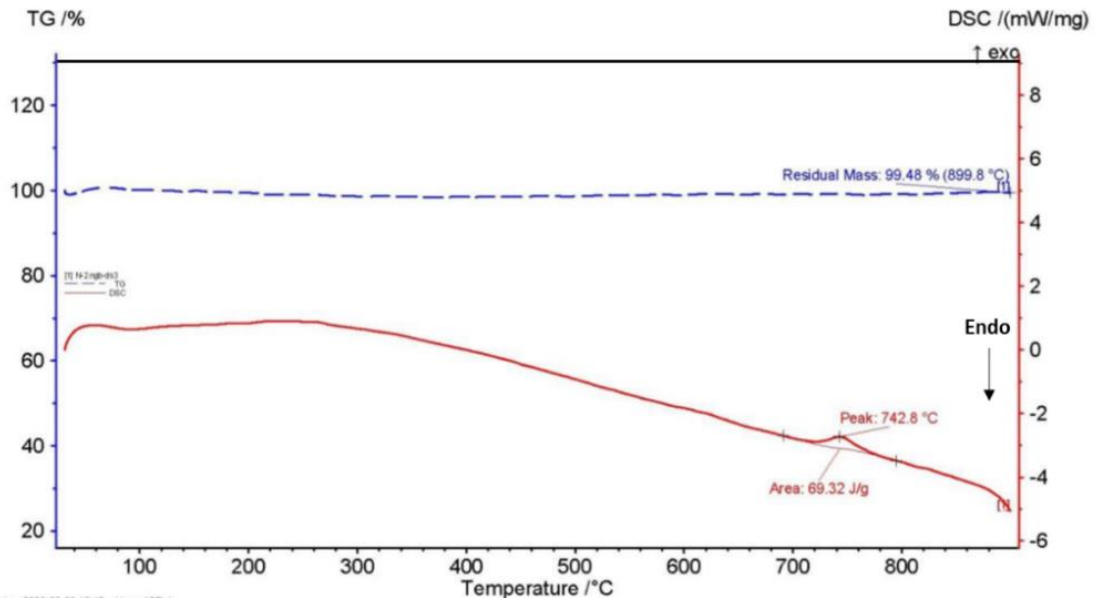


Figure 43. TGA and DSC curves of MTB@HAp.

Thermal behavior of MTB@HAp was analyzed with TGA/DSC. The analysis result is given in Figure 43. In thermogram, the DSC (red line) represents chemical and physical changes in the samples structures during the temperature rising. The TG (blue dash line) records changes in the samples mass along of this process. Mass loss of MTB@HAp between 20°C and 900°C is approximately 1%. In DSC analysis, there is exothermic heat release due to decomposition of HAp [95].

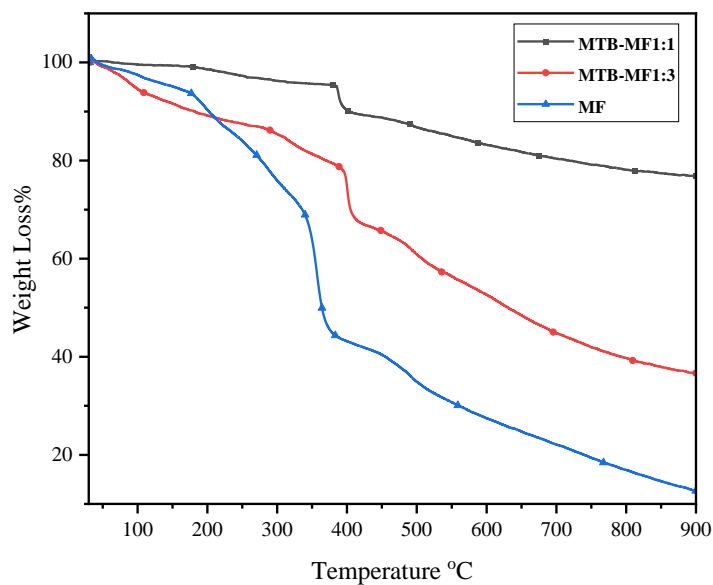


Figure 44. TGA curves of MTB-MF (1:1), MTB-MF (1:3) microcapsule.

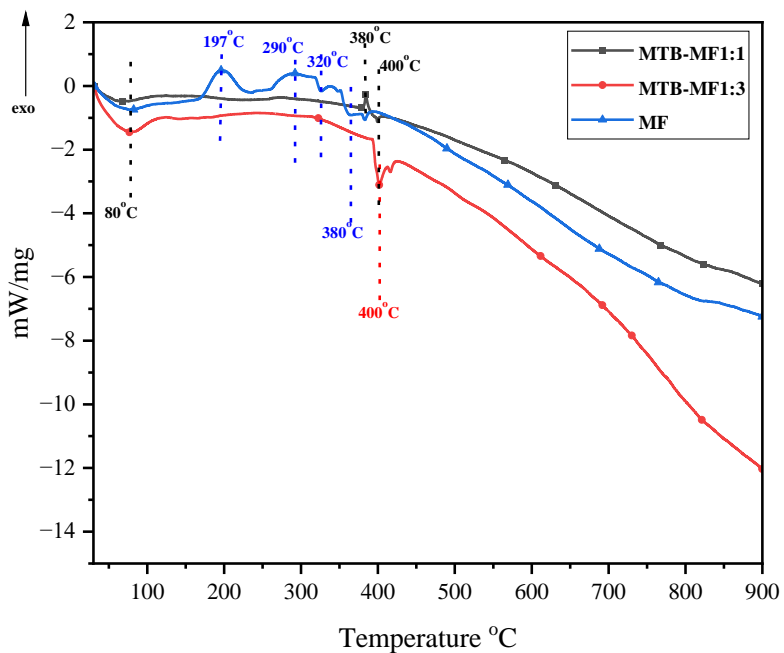


Figure 45. DCS curves of MTB-MF (1:1) microcapsule, MTB-MF (1:3) microcapsule.

The thermal characteristics of the MF and MTB-MF microcapsules with different MF ratio are demonstrated in Figure 44 and Figure 45. The thermal stability data of MF encapsulated MTB was obtained through TG analysis. The TGA and DSC curves of the samples are indicated in Figure 44 and Figure 45. Besides, the data are interpretant in Table 9. The weight losses of MF resin and MTB-MF microcapsules can be divided into five steps. Figure 44 is the TG curves of samples MF resin, MTB-MF 1:1, MTB-MF 1:3. Figure 45 shows DSC analysis of the samples. The first temperature interval (30 to 100 °C) in the curves of MF resin, MTB-MF 1:1, and MTB-MF 1:3 samples corresponds to the evaporation of moisture retained during synthesis [96, 97]. The weight losses are in both samples MF and MTB-MF 1:3 was 4% and 1% for MTB-MF 1:1. During the second stage of thermal degradation, the differential scanning calorimetry (DSC) curve of melamine-formaldehyde (MF) exhibits exothermic peaks at 197 °C. This observed increase in temperature signifies the progression of the resin curing process. According to the research by Merline et al. [98], the curing reactions that occur in the temperature range of 100 to 200 °C are a result of the self-condensation of methylol groups. This leads to the formation of ether bridges in the temperature range of 140 to 160°C. Additionally, there is another condensation reaction between methylol groups (-CH₂-OH) and melamine, leading to the formation of methylene bridges at temperatures above 160 °C. It is worth noting that melamine is formed in a reverse reaction (decomposition) of 3-methylol melamine in the temperature range of 140 to 160 °C [96]. At a temperature of 140 °C, the methylol groups undergo decomposition, resulting in the liberation of formaldehyde. This formaldehyde may interact with free amine groups, leading to the formation of another ether linkage [97]. The DSC curve of MF sample in the temperature range of 100-200 °C differs slightly from MTB-MF 1:1 and 1:3 samples. The exothermic peak appears at 189 °C for MF. However, in the case of samples MTB-MF 1:1 and 1:3, no additional peaks were observed around 190°C. This means that the DSC traces of MTB-MF 1:1 and 1:3 show a flat line, indicating that the resin has been completely cured. Within the temperature range of 200 to 380°C, the highest weight loss of 45% can be ascribed exclusively to demethylation. This

outcome suggests that weight loss in MF resins below 290°C is likely due to NHCH_2OH groups reverting to NH_2 [99]. It is important to note that any evidence of degradation, apart from the loss of formaldehyde, cannot be substantiated [100]. At temperatures beyond 331°C, a polycondensation reaction was ensured, leading to the formation of diverse products through independent reactions involving both side chain and ring degradation of triazine ring of melamine. This implies that some melamine molecules can sublime at a temperature lower than the standard sublimation temperature observed at 346°C. Nonetheless, the MTB-MF 1:1 and 1:3 samples displayed thermal stability of the melamine formaldehyde resin, even at a temperature as high as 380°C [99]. The weight losses in the samples MTB-MF 1:1 and 1:3 was 3% and 11% respectively. Throughout the process of weight loss within the MTB-MF samples, specifically at temperatures between 380°C and 450°C, it was observed that various compounds such as formaldehyde, methanol, amine, and NH_3 were released [96]. The results obtained from the recent weight measurements at temperatures exceeding 450°C were consistent with the expected outcomes of melamine's thermal degradation, as typically observed [96, 99, 101]. The formation of cyameluric structures in melamine-formaldehyde (MF) has been proposed by Ferra et al. [102]. Degradation of the MF resin condensate is observed at temperatures above 660 °C, leading to the generation of volatile products such as CO_2 , HCN, and CO [96]. In addition, the total weight loss of MF in the temperature range 30–900 °C was around 88% and the amount of MTB-MF microcapsule residues observed during TGA analysis at 900°C decreased from 76% to 36% with an increasing MF encapsulation ratio from 1:1 to 13. This indicates that the volume of MF microcapsules increases with the MF ratio increases.

Table 9. Results of thermogravimetric analysis of MTB and MTB-MF microcapsules.

Sample Name	Stage-I		Stage-II		Stage-III		Stage-IV		Stage-V		Residue
	T° C-Range	Mass Losses%	T° C-Range	Mass Losses%	T° C-Range	Mass Losses%	T° C-Range	Mass Losses%	T° C-Range	Mass Losses%	
MTB	30-100	~1%	100-200	~6.5%*	-	-	-	-	-	-	~92%
MF	30-100	~3%	100-200	~6%	200-380	~45%	380-450	~5%	450>	~28%	~12%
MTB-MF (1:1)	30-100	~1%	100-200	~2%	200-380	~3%	380-450	~8%	450>	~8%	~76%
MTB-MF (1:3)	30-100	~4%	100-200	~5%	200-380	~11%	380-450	~15%	450>	~30%	~36%
The Weight Loss due to	Release of Water-Formaldehyde (unreacted)		*: adsorbed water Elimination of Formaldehyde, post curing		Destruction of Triazine Ring for MF and Ammonia release in MF capsules		Destruction of Triazine Ring. The organic polymer destruction and char formation, HCN, CO formation				

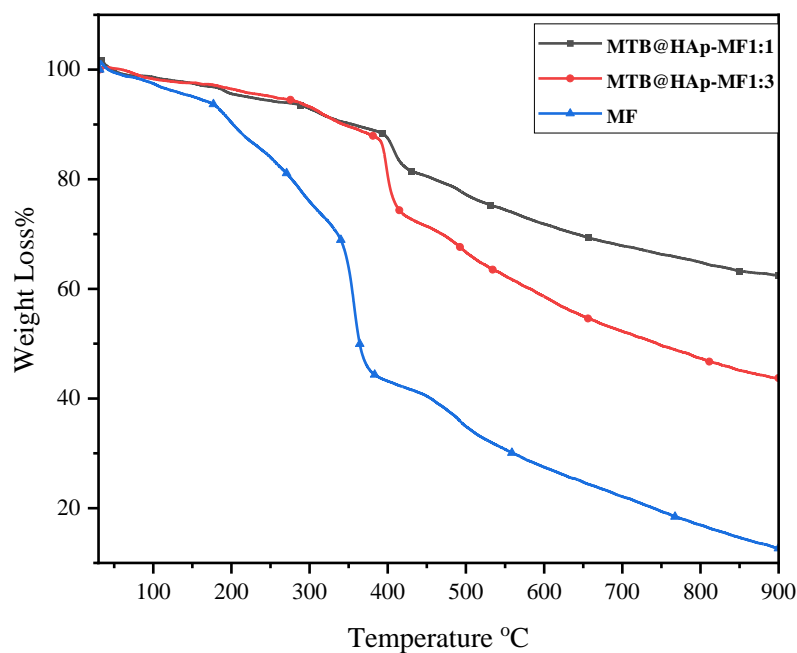


Figure 46. TGA curves of MTB@HAp-MF (1:1) microcapsule, MTB@HAp-MF (1:3) microcapsule, MF resin.

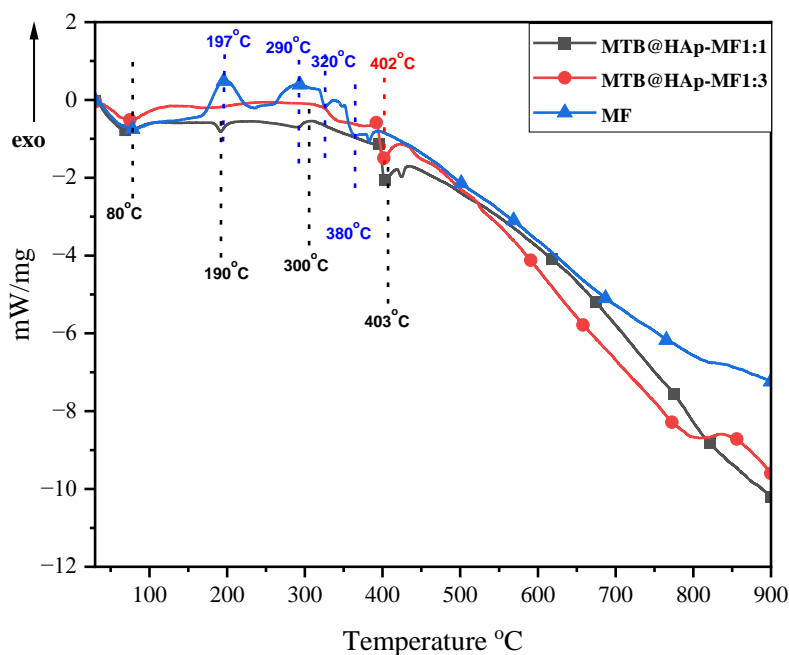


Figure 47. DSC curves of MTB@HAp-MF (1:1) microcapsule, MTB@HAp-MF (1:3) microcapsule, MF resin.

TGA and DSC curves of MTB@HAp and MF encapsulated MTB@HAp with different ratio, 1:1 and 1:3, which are shown in Figure 46 and Figure 47, respectively. The thermal behavior of MTB@HAp-MF microcapsules monitored by TGA and DSC show a complex mechanism of thermal degradation in five main consecutive stages: from 30 to 100 °C, 100 to 200 °C, 200 to 380 °C, 380 to 450 °C for temperatures higher than 450 °C, which is given in Table 10. Thermal degradation of MF was detailed in Figure 47. MF encapsulated MTB@HAp 1:1 and 1:3 has similar mass loss regime. The first weight loss (~3%) can be ascribed to the evaporation of water, which is demonstrated by endothermic peak in DSC [96]. For the second interval of 100 to 200 °C, DSC measurement indicates an exothermic peak associated with curing reactions. These reactions entail the self-condensation of methylol groups. However, in the case of the sample MTB@HAp-MF 1:1, an endothermic peak is observed, which is attributed to dehydration [100]. In the range

of 200-380 °C which corresponds to the elimination of formaldehyde accompanied with exothermic peak in DSC [67]. Beyond 380 °C, the three-dimensional polymer structure of melamine breaks down during its thermal degradation during TGA analysis at 900 °C. It was observed that the amount of microcapsule residue decreased from 62% to 43% as the MF encapsulation ratio increased. This suggests that the volume of MF microcapsules also increases as the MF ratio increases.

To compare thermal characteristics of MTB and MTB@HAp microcapsules, thermal decomposition temperatures of microcapsules are inspected. MTB@HAp microcapsules present a relatively good thermal stability since no significant weight loss occurred until 290 °C indicating the stability of the microcapsules in this temperature range. It is evident that the amount of encapsulated MF on the surface of MTB@HAp is lower than that of MTB-MF microcapsules when exposed to char residue during thermal analysis. Furthermore, the exothermic peak between 150-270 °C, as seen in Figure 45, cannot be observed in the DSC analysis of MTB@HAp and MTB-MF microcapsules. This is since curing of MF resin was completed.

Table 10. Results of thermogravimetric analysis of MTB@HAp and MTB@HAp-MF microcapsules.

Sample No	Stage-I		Stage-II		Stage-III		Stage-IV		Stage-V		Residue
	T°C-Rang e	Mass Losses %	T°C-Rang e	Mass Losses %	T°C-Rang e	Mass Losses %	T°C-Rang e	Mass Losses %	T°C-Rang e	Mass Losses %	
MTB@HAp	30-100	~0.5%	-	-	-	-	-	-			~99,5%
MF	30-100	~3%	100-200	~6%	200-380	~45%	380-450	~5%	450>	~28%	~12%
MTB@HAP-MF (1:1)	30-100	~3%	100-200	~2%	200-380	~6%	380-450	~8%	450>	~18%	~62%
MTB@HAP-MF (1:3)	30-100	~3%	100-200	~2%	200-380	~8%	380-450	~18%	450>	~26%	~43%
The Weight Loss due to	Release of Water		Elimination of Formaldehyde		Destruction of Triazine Ring		The organic polymer destruction and char formation				

4.1.6 TGA-FTIR Analysis of MF Resin

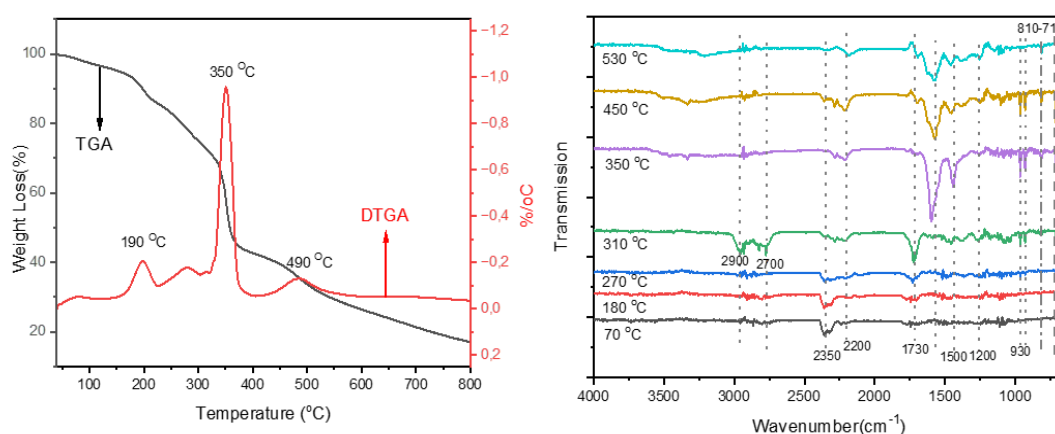


Figure 48. TGA/DTGA Curve and FTIR of MF Resin at different temperatures.

Thermal gravimetric analysis coupled with fourier-transform infrared spectroscopy (TGA-FTIR) was employed to analyze the pyrolysis products generated from the decomposition of MF. The spectra of evolved gases at different pyrolysis temperatures are shown in Figure 48. The spectral analysis indicates that the primary gaseous emissions consist of $\text{-C}\equiv\text{C-R}$ (2349 cm^{-1}), amines (1641 cm^{-1} and 3247 cm^{-1}), methanol (671 cm^{-1}), and compounds containing C-O-C (1232 cm^{-1}) and C-C (1099 cm^{-1}). The vibrations at 960 cm^{-1} and 930 cm^{-1} are attributed to symmetric bending of N-H bonds in ammonia (NH_3) over $300\text{ }^\circ\text{C}$ [103]. Moreover, upon decomposition at $350\text{ }^\circ\text{C}$, a distinctive absorption at 2275 cm^{-1} arises, only to disappear during pyrolysis at $500\text{ }^\circ\text{C}$. This absorption is likely attributed to compounds containing $\text{-C}\equiv\text{N}$, such as HCN. Furthermore, the characteristic absorption of melamine, identified by peaks at 1436 and 814 cm^{-1} , can be detected in the decomposition products during decomposition at $340\text{ }^\circ\text{C}$. These peaks correspond to the stretching vibration of C=N and deformation of the triazine ring, respectively. These observations suggest the emergence of gaseous melamines during the thermal decomposition of MF resin, which could be caused by the sublimation of melamine above $340\text{ }^\circ\text{C}$ [104].

4.2 Characterization of Flame Retardancy Properties of PU Composites

Limiting oxygen index measurement (LOI) and Vertical Burning Test-UL-94, Thermogravimetric Analysis, and Conic Calorimeter Test were widely used to evaluate the flammability of materials. Corresponding data summarized in Table 21. LOI value and UL 94 rating of PU samples.

4.2.1 TGA and TGA-FTIR Analyses of PU Composites

Thermogravimetric analysis (TGA) is a well-established method utilized for evaluating the thermal characteristics of polyurethane. Even today, it remains a commonly employed analytical technique. The criteria for thermal stability

encompass sustaining mechanical properties (such as melting and softening points), strong resistance against chemicals, and exceptional resilience against degradation, especially in oxidative environments.

4.2.1.1 Thermogravimetric Analysis of MTB-PU Composites

The thermal decomposition properties of neat polyurethane (PU) and MTB-PU composites with varying MTB content were subjected to TGA analysis under a nitrogen atmosphere. This examination aimed to investigate the behavior of the materials in response to thermal stability. The related data are given Table 11. Figure 49 and Figure 50 show the TGA and Derivative Thermogravimetric Analysis (DTGA) graphs. Through the examination of TGA (Thermogravimetric Analysis) and DTG (Derivative of Thermal Analysis) curves, valuable insights can be gained regarding the thermal stability of PU composites. These insights include identifying the onset of weight loss, the initiation of thermal degradation, the peak rate of weight loss, the extent of weight loss during the most intense degradation, the weight residue at 610 °C, as well as other relevant parameters [105].

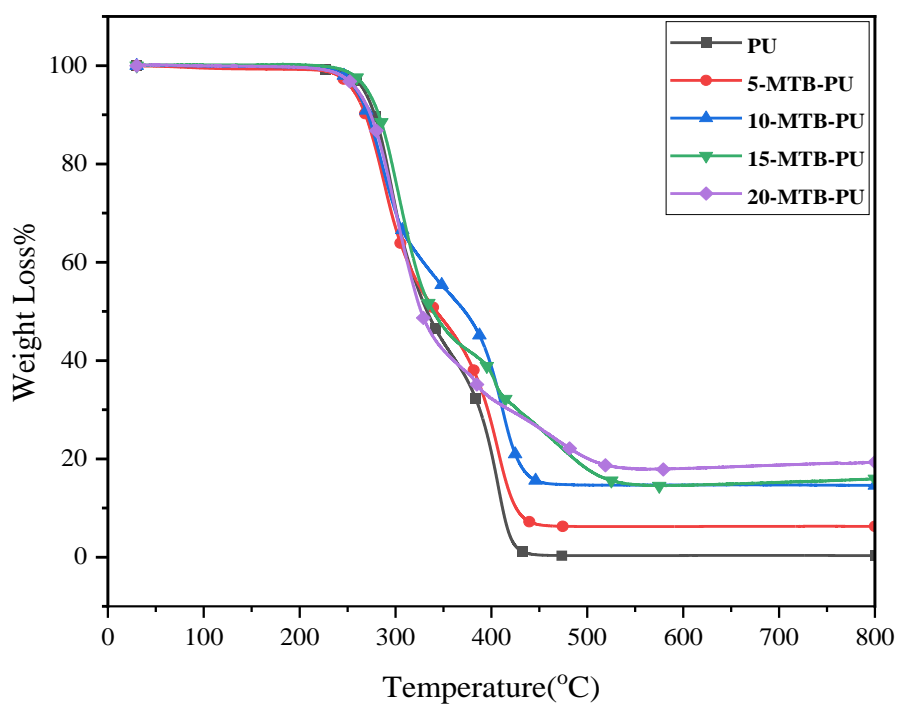


Figure 49. TGA curves of Neat PU and MTB-PU compositions.

Table 11. TGA Data of neat PU and MTB-PU Composites sample

Sample Name	T _{5%} (°C) ^a	T _{50%} (°C) ^b	T _{max1%} (°C) ^c	T _{max2%} (°C) ^c	Char yield (%) ^d
PU	268	332	295	404	0.3
5-MTB-PU	256	338	290	410	6.1
10-MTB-PU	262	368	285	412	13.3
15-MTB-PU	269	337	302	403	15.4
20-MTB-PU	258	325	298	383	19.0

^{a,b}Temperature at 5% and 50% weight losses.

^cThe maximum degradation rate temperature.

^dResidue yield at 900°C.

As indicated in the relevant literature, the process of thermal degradation in polyurethane occurs in two or three stages. The initial stage involves the decomposition of hard segments and urethane linkages, while the second and third stages are associated with the decomposition of soft segments [106, 107, 108]. The curve of neat PU in Figure 49 show two steps of degradation. According to Table 11, the initial phase of degradation commences at 220 °C, with the highest rates of decomposition occurring at 295 °C and 404 °C. This overlaps with our findings. The first stage of degradation can be attributed to the thermolysis of urethane linkages, while the second stage is a result of the macrodiol component breaking down, ultimately leaving a carbonaceous residue of only 0.3 wt.%. Char yield depends on polyol structure [105]. With the addition of MTB with varying concentration (between 5Phr and 20 Phr) into PU, the composite degrades in two or three steps. 5-MTB-PU and 10-MTB-PU composites also undergo two-step degradation. 15 and 20PHR MTB containing PU degrades three steps. The addition of MTB further reduces the $T_{5\%}$ value of MTB-PU composites. It has been observed that the maximum temperature at which degradation occurs ($T_{50\%}$) tends to decrease with a rise in the quantity of MTB added, except in the case of MTB-15. In the temperature range of 220 °C to 360 °C, the behavior of 5-MTB-PU and 10-MTB-PU appears to be quite similar. However, between 340 °C and 500 °C, 10-MTB-PU exhibits greater stability compared to neat PU and other MTB-PU composites. This is due to its higher char residue content of 14% among MTB-PU composites with respect to FR% in PU. The data presented in Table 12 illustrates the temperature of decomposition and the rate of mass loss for both neat PU and MTB-PU. The initial stage of neat PU degradation takes place within the temperature range of 220 °C-376 °C. The second stage, which is characterized by T_{max2} peak, occurs within the range of 348 °C-470 °C. The maximum degradation rate for the first stage, known as T_{max1} , falls within the range of 285°C -302°C, while for the second stage or T_{max2} , it falls within the range of 348°C-420°C for the composites. The first step degradation in DTG profiles (Figure 50) of PU and MTB-PU (up to 10 PHR) are similar. It was observed that the highest decomposition rate of 10-MTB-PU, indicated by the main peak of the DTG

curve, occurred at temperatures of up to 410°C. Additionally, the weight loss of all the PU composites studied during the initial degradation stage (Δm_1) corresponded to the hard segment content (urethane linkage) detailed in Table 12. The improved thermal stability of the MTB-PU composite is indicated by the increased Δm_2 (%) of 10-MTB-PU, as compared to PU and other composites.

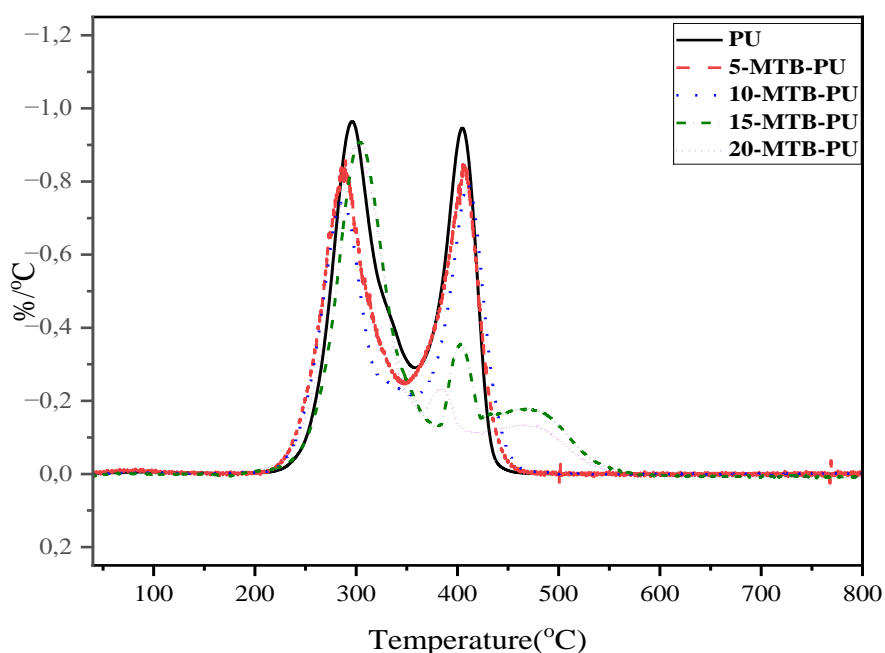


Figure 50. First derivative (DTG) curves of neat PU and MTB-PU composites.

The DTGA profiles of MTB-PU, which include 15 and 20PHR MTB composites, exhibit an increase in weight loss beyond 430°C due to a low crosslinking density. The most significant degradation stage, featuring a DTG peak maximum between 220°C and 360°C, resulted in weight losses ranging from 50% to 60%. As a result, the composites experienced a reduction in thermal stability.

Table 12. DTGA data of neat PU and MTB-PU composites.

Sample Name	T _{max1} (°C)	1.Peak Range(°C)	Δm1 (%)	T _{max2} (°C)	2.Peak Range(°C)	Δm2 (%)
PU	295	223-361	60	404	361-454	39
5%MTB-PU	290	217-348	51	410	348-465	42
10%MTB-PU	285	220-358	47	412	358-470	38
15%MTB-PU	302	238-376	57	403	376-425	12
20%MTB-PU	298	226-366	60	383	366-420	10

T_{max1,2}, temperature of maximum rate of decomposition for the first and second steps of degradation from the DTG curve.
 Δm1,2, mass loss on the end of the first and second steps of degradation.

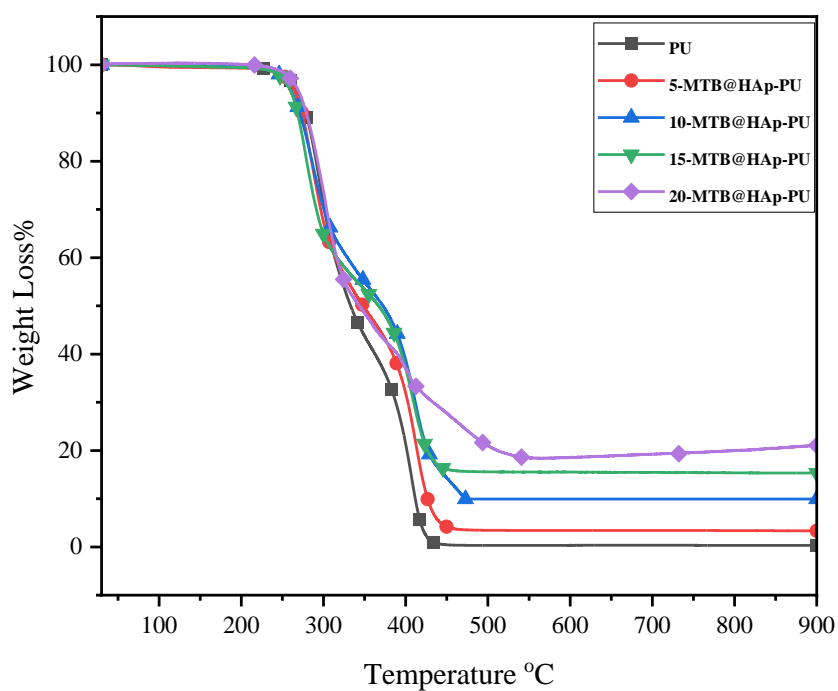


Figure 51. TGA curves of MTB@HAp-PU compositions.

Table 13. TGA Data of neat PU and MTB@HAp-PU Composites sample.

Sample Name	T _{5%} (°C) ^a	T _{50%} (°C) ^b	T _{max1%} (°C) ^c	T _{max2%} (°C) ^c	Char yield (%) ^d
PU	268	332	295	404	0.3
5-MTB@HAp-PU	263	344	287	410	3.4
10-MTB@HAp-PU	260	360	282	412	9.8
15-MTB@HAp-PU	258	363	277	410	16
20-MTB@HAp-PU	266	340	301	397	19

^{a,b}Temperature at 5%,50% weight losses.

^cThe maximum degradation rate temperature.

^dResidue yield at 900°C.

The results of the TG and DTG analyses of MTB@HAp-PU composites are listed in Table 13 and Table 14, weight loss profiles with temperature are shown in Figure 51 and Figure 52. Upon analyzing the degradation process of MTB@HAp-PU composites, it was discovered that thermal degradation occurs in two distinct phases. However, should the MTB@HAp content surpass 15 PHR in PU, a three-phase degradation process ensues. During the initial phase of degradation, the temperature range of initial decomposition, the temperature at which degradation commences, and the temperature corresponding to the maximum rate of degradation (T_{max1}), all decrease in comparison to neat PU. The thermal stability of MTB@HAp-PU composite material was evaluated, and the results indicate that the second decomposition temperature increased by 10°C, with a corresponding increase in the temperature at the maximum rate of degradation from 404 °C to 410 °C. The 15-MTB@HAp-PU sample attained the highest T_{max2} , which represents the temperature at which the maximum rate of degradation occurs, resulting in a 40% weight loss (Δm_2). During the initial stage of degradation, the weight loss indicated by Δm_1 decreases. However, as the MTB@HAp content increases by 15 PHR in the second stage of degradation, the weight loss represented by Δm_2 increases. For 20-MT-HAp-PU, thermal degradation is observed in three stages, which are clearly depicted in the TGA graph. The third step of degradation is also supported by the first derivative of TGA. The data presented suggests that the hard segment of 20-

MTB@HAp-PU displays low thermal stability. The observed $T_{\max 1}$ degradation, combined with the highest weight loss%, supports this conclusion [109]. The inclusion of MTB@HAp in PU as a flame retardant has been found to enhance the thermal stability of PU by improving its thermal insulation properties, up to a certain limit of 15 PHR. However, the addition of excessive amounts of MTB@HAp may lead to a decrease in the crosslink density of PU, which in turn may result in a deterioration of the thermal stability of PU composite.

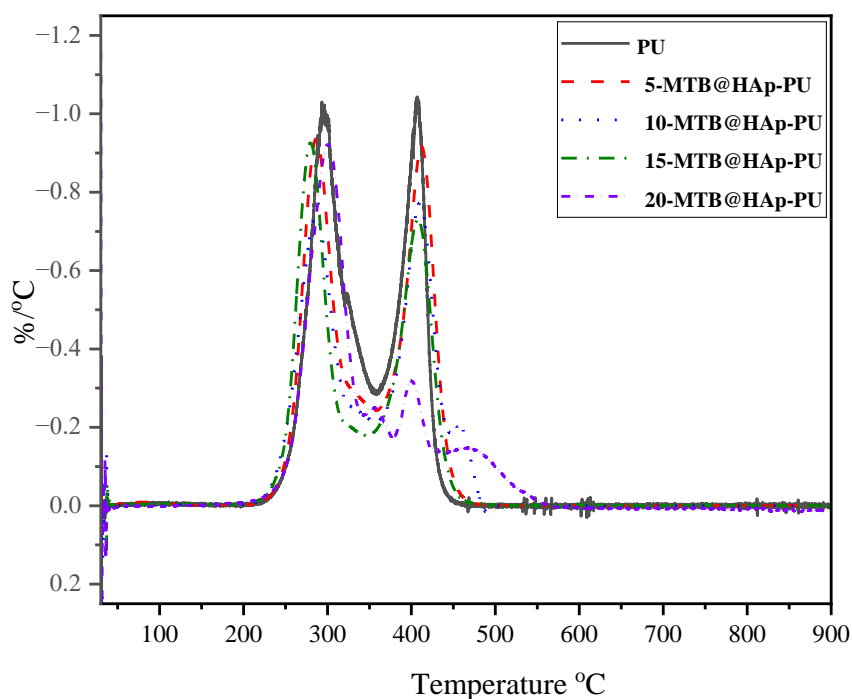


Figure 52. First derivative (DTG) curves of neat PU and MTB@HAp-PU composites.

Table 14. DTGA data of neat PU and MTB@HAp-PU composites.

Sample Name	T _{max1} (°C)	1.Peak Range(°C)	Δm1 (%)	T _{max2} (°C)	2.Peak Range(°C)	Δm2 (%)
PU	295	223-361	60	404	361-454	39
5-MTB@HAp-PU	287	216-354	50	410	354-480	44
10-MTB@HAp-PU	282	215-360	57	412	360-450	30
15-MTB@HAp-PU	277	210-344	45	410	344-470	40
20-MTB@HAp-PU	301	214-382	50	397	382-430	30

T_{max1,2}, temperature of maximum rate of decomposition for the first and second steps of degradation from the DTG curve.
 Δm1,2, mass loss on the end of the first and second steps of degradation

Melamine formaldehyde is a type of additive flame retardant that finds extensive usage in flame retardant polyurethanes [87, 110]. The minimum required Melamine-Formaldehyde (MF) ratio in the MTB-MF1:1 composite is 2.5 PHR. This ratio was added to the polyurethane (PU) and subsequently utilized to investigate the thermal stability of the resultant MF-PU composites. The study involved generating TGA curves, which are presented in Figure 53. It has been observed that the weight loss pattern of neat PU and MF-PU composites is quite similar. (two-step degradation illustrated in Figure 53). Nevertheless, first degradation starts earlier than neat PU, which is supported by T_{5%} data given in Table 15. In DTG graph in Figure 54, Figure 53. TGA curves of neat PU and MF-PU compositions. According to the results of the thermogravimetric analysis, the MF-PU underwent a significant weight loss between the temperatures of 180 °C-370 °C. This phenomenon was attributed to the evaporation of the flame-retardant MF.

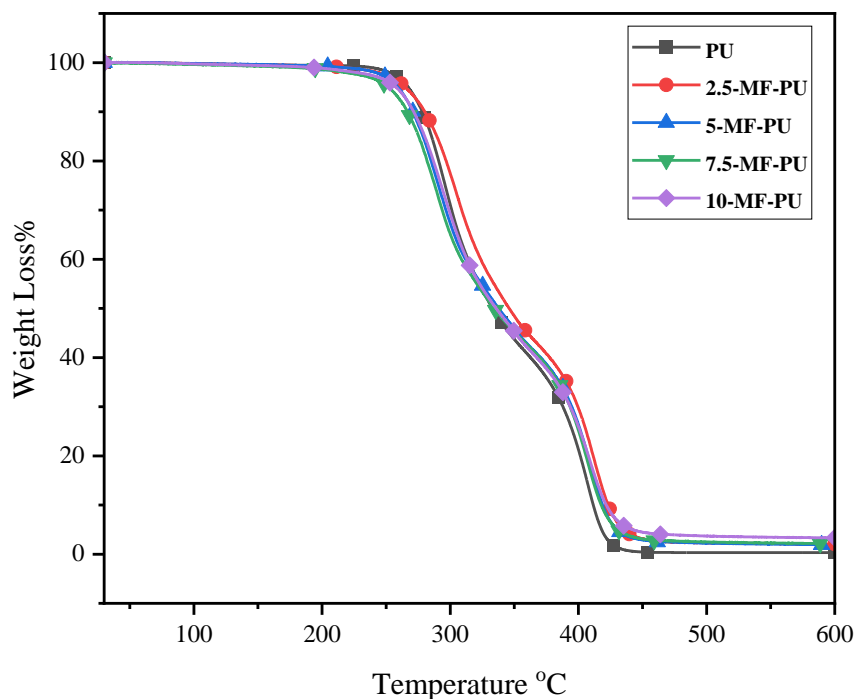


Figure 53. TGA curves of neat PU and MF-PU compositions.

It should be noted that upon heating Melamine Formaldehyde (MF) to 180 °C, formaldehyde gas is released [97]. Moreover, it has been observed that the compound undergoes decomposition in the temperature range of 150-200°C, which is observed in Figure 44. Conversely, from 360 to 480 °C, MF-PU shows more stability than neat PU, which is supported by increasing second weight loss rate temperature T_{max2} shifted to 410 °C from 400 °C, which is summarized in Table 16. Although char residues at 900 °C increased by 10 PHR containing MF-PU, the increase in total residue % is not significant. This is evidence of thermal stability increased slightly with addition of 2.5-MF into PU.

Table 15. TGA Data of neat PU and MF-PU Composites sample.

Sample Name	T _{5%} (°C) ^a	T _{50%} (°C) ^b	T _{max1%} (°C) ^c	T _{max2%} (°C) ^c	Char yield (%) ^d
PU	268	332	295	404	0.3
2.5-MF-PU	261	344	303	411	2.1
5-MF-PU	255	337	293	410	2.2
7.5-MF-PU	251	332	288	404	2.2
10-MF-PU	256	330	295	408	3.2

^{a,b}Temperature at 5%, 50% weight losses.

^cThe maximum degradation rate temperature.

^dResidue yield at 900°C.

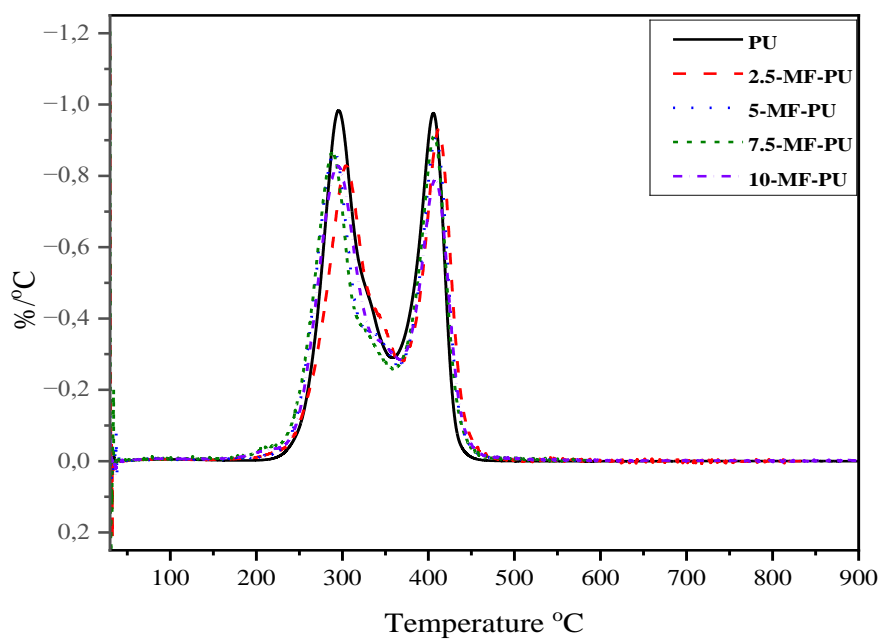


Figure 54. First derivative (DTG) curves of MF-PU composites.

Table 16. DTGA data of neat PU and MF-PU composites.

Sample Name	T _{max1} (°C)	1.Peak Range(°C)	Δm1 (%)	T _{max2} (°C)	2.Peak Range(°C)	Δm2 (%)
PU	295	223-361	60	404	361-454	39
2.5-MF-PU	303	186-367	58	411	367-476	40
5-MF-PU	293	190-365	59	410	365-476	38
7.5-MF-PU	288	185-361	57	404	361-476	40
10-MF-PU	295	187-364	59	408	364-482	38

T_{max1,2}, temperature of maximum rate of decomposition for the first and second steps of degradation from the DTG curve.
 Δm1,2, mass loss on the end of the first and second steps of degradation

TGA and DTGA curves of neat PU, MTB-PU and Melamine Formaldehyde encapsulated MTB containing PU composites are shown in Figure 55 and Figure 56 respectively. The related data are given in Table 17 and Table 18. The thermal degradation of the composites proceeds in two stages (Figure 55 and Figure 56). For neat PU, the initial phase of the decomposition process is a significant occurrence in polyurethane, with nearly 60% of the material undergoing decomposition between 220 °C and 360 °C [74]. Addition of MTB, MF and MTB-MF with 5 PHR, Table 18 shows a noteworthy decrease of approximately 30°C in the first thermal decomposition temperature. This decrease can be attributed to the crosslink density of the polyurethane and the evaporation or decomposition of the flame retardant prior to the PU degradation temperature [106, 105]. The addition of borate unit to polyurethane (PU) with MTB may reduce the crosslink density of PU by reacting with the isocyanate group during the curing process. The incorporation of MF or MTB-encapsulated MF into PU resulted in a temperature reduction of 30°C for 5% weight loss. It is believed that the reduction in thermal stability is due to the comparatively lower thermal stability of the fillers (MF) relative to the neat PU. During the second degradation stage of neat PU, the maximum weight loss rate was recorded at 404 °C, resulting in a residue of only 0.3% char at 900 °C.

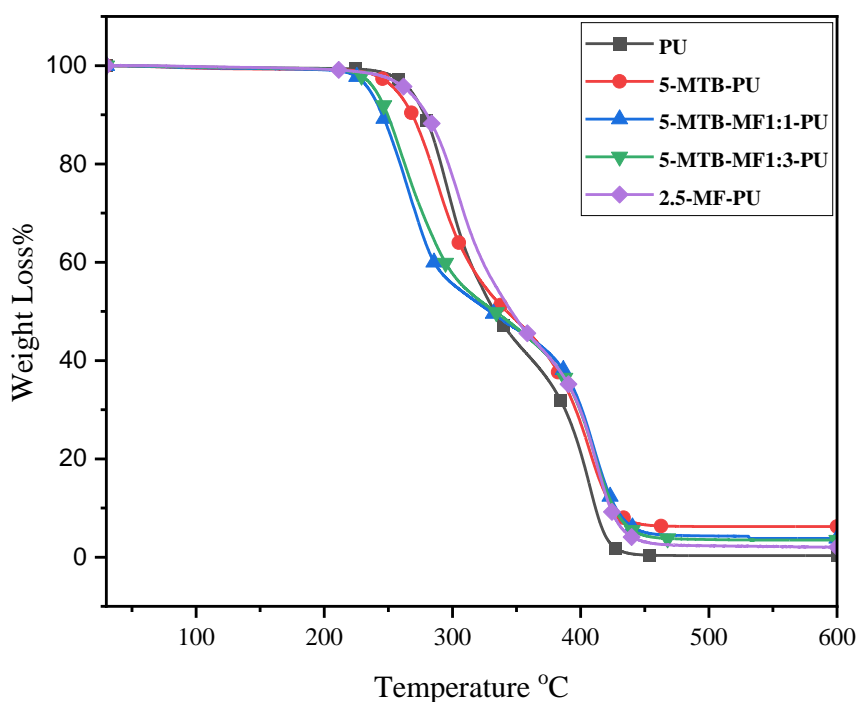


Figure 55. TGA curves of MTB and MTB-MF-PU compositions.

Table 17. TGA Data of neat PU and MTB-MF-PU Composites sample.

Sample Name	T _{5%} (°C) ^a	T _{50%} (°C) ^b	T _{max1%} (°C) ^c	T _{max2%} (°C) ^c	Char yield (%) ^d
PU	268	332	295	404	0.3
2.5-MF-PU	261	344	303	411	2.1
5-MTB-PU	256	338	290	410	6.0
5-MTB-MF1:1-PU	245	327	265	410	3.8
5-MTB-MF1:3-PU	240	355	262	408	3.4

^{a,b}Temperature at 5%,50% weight losses.

^cThe maximum degradation rate temperature.

^dResidue yield at 900°C.

It has been observed that the inclusion of MTB has no impact on the thermal degradation properties of PU. However, due to the presence of undecomposed MTB,

the residual yield increases up to 6%. On the other hand, the addition of MF and MTB-MF exhibits a remarkable rise in the maximum weight loss ($T_{\max 2}$) by approximately 10°C. It has been observed that the MTB-MF composite exhibits a greater range of degradation in comparison to MF alone. In Figure 55, this may be attributed to the microencapsulation of MTB, which enhances the stability of the filler at higher temperatures (specifically, within the range of 330-480°C). This increase in weight loss value at elevated temperatures suggests that the 5-MTB-MF-PU composites may offer superior thermal stability as compared to those containing 2.5-MF-PU. Furthermore, MF encapsulation ratio effects on thermal stability of PU was investigated by TGA and DTGA. The incorporation of MTB-MF1:1 results in a slight decrease in the initial thermal stability ($T_{5\%}$) and maximum main weight loss ($T_{\max 1}$). Similarly, the employment of 2.5-MF and MTB-MF1:1 produces a similar trend in the $T_{5\%}$ and $T_{\max 1}$ values as compared to MTB-MF1:3. However, the first and second maximum degradation period of MTB-MF1:3 reduced with increasing MF ratio on MTB. Thermal degradation trend of MTB-MF1:3 becomes similar to MF-PU. It is supported by char residues values of MTB-MF1:3 and MF. Char residues decreased with increasing MF ratio. Accordingly, the lower char formation is observed for MF-PU. It is evidence that most of MTB-MF1:3 contains MF, which decomposes at 900 °C.

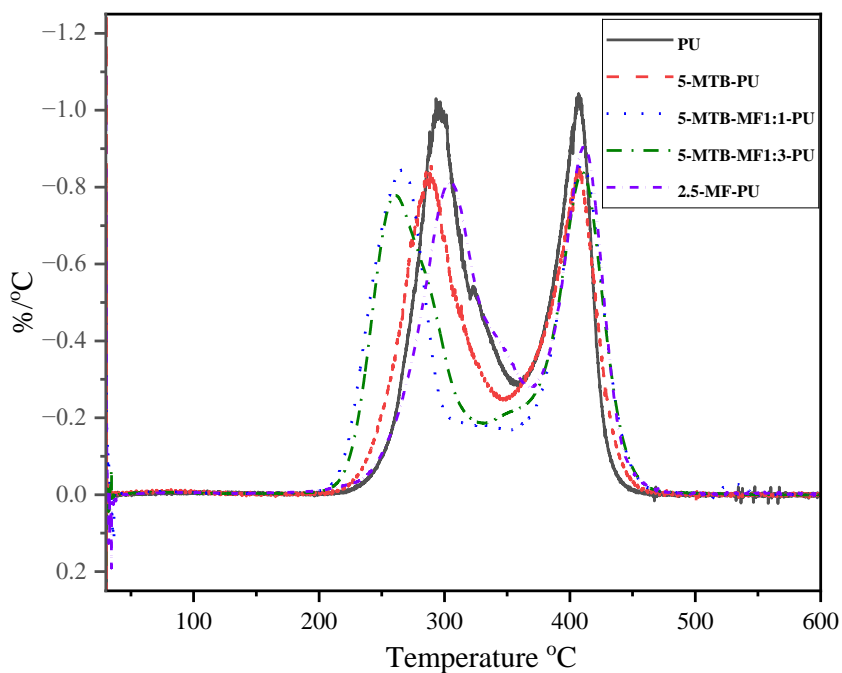


Figure 56. First derivative (DTG) curves of Neat PU and MTB-MF-PU composites.

Table 18. DTGA data of neat PU and MTB-MF-PU composites.

Sample Name	T _{max1} (°C)	1.Peak Range(°C)	Δm1 (%)	T _{max2} (°C)	2.Peak Range(°C)	Δm2 (%)
PU	295	223-361	60	404	361-454	39
2.5-MF-PU	303	186-367	58	411	367-476	40
5-MTB-PU	290	217-248	51	410	348-465	42
5-MTB-MF1:1-PU	265	202-330	50	410	330-480	44
5-MTB-MF1:3-PU	262	190-331	50	408	331-475	46

T_{max1,2}, temperature of maximum rate of decomposition for the first and second steps of degradation from the DTG curve.
 Δm1,2, mass loss on the end of the first and second steps of degradation

TGA and DTGA curves of neat PU, MTB@HAp-PU and Melamine Formaldehyde encapsulated MTB@HAp (1:1 and 1:3 MF ratios) containing PU composites are shown in Figure 57 and Figure 58, respectively. The related data are given in Table 19 and Table 20. Polyurethane (PU) and its composites undergo thermal degradation in two stages [2]. When MTB@HAp is added, the initial thermal stability ($T_{5\%}$) and the maximum main weight loss ($T_{\max 1}$) decrease by 48%. However, in the second stage, thermal stability increases by 10°C compared to the second decomposition temperature of PU alone. At 900°C , the residue weight is 3.4%, which is lower than the amount initially added. The MTB@HAp composite demonstrates a higher decomposition temperature compared to PU. However, the mixing process for the composites may lead to low char yield due to inhomogeneity. Notably, the MTB@HAp-MF1:1 and MTB@HAp-MF1:3 composites feature two-step degradations akin to PU. Nonetheless, the first step of degradation commences earlier than the $T_{5\%}$ values of neat PU. This reduction in thermal stability may be linked to the lower thermal stabilities of MF on MTB@HAp. As the MF ratio increases from 1:1 to 1:3 in MTB@HAp-MF, both $T_{5\%}$ and $T_{\max 1}$ values reduce, which is in line with the expected behavior. Additionally, the $T_{\max 2}$ values of MTB@HAp-MF 1:1 and 1:3 was 395°C and 406°C , respectively. The introduction of MTB@HAp-MF1:1 has no significant effect on $T_{\max 2}$ and $T_{\max 2}$ degradation step, with the DTG peak maximum occurring at $361^{\circ}\text{C} - 455^{\circ}\text{C}$. However, in the case of MTB@HAp-MF1:3, the $T_{\max 2}$ of degradation step with the DTG peak maximum starts at 335°C and continues to 470°C , with a higher mass loss of 47%. It is believed that triazine degradation starts in the range of 250°C and 300°C , which leads to the expansion of the $T_{\max 2}$ degradation step with a higher weight loss [67].

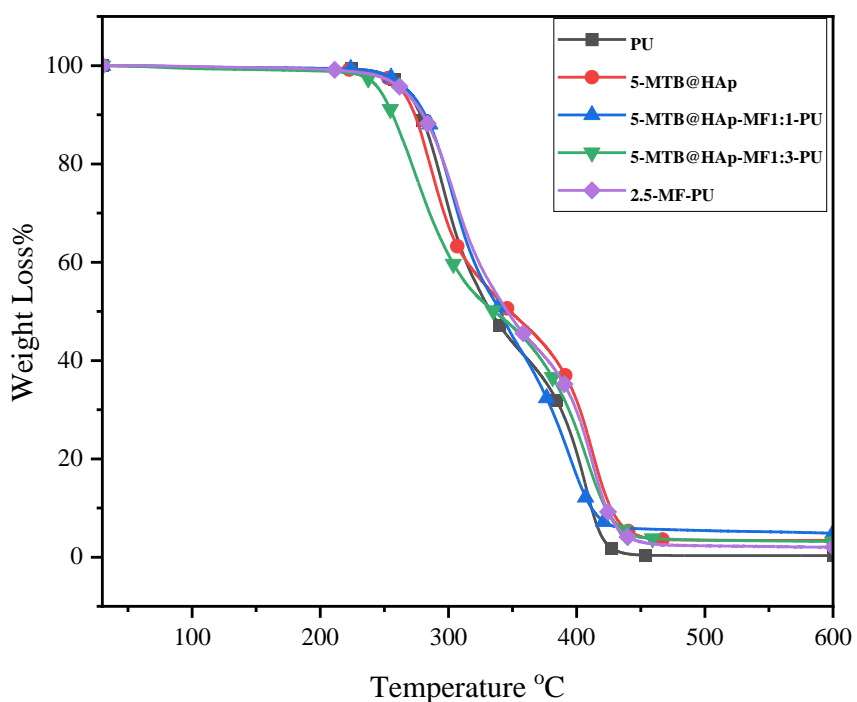


Figure 57. TGA curves of PU, MTB@HAp and MTB@HAp-MF-PU composites.

Table 19. TGA Data of neat PU, MTB@HAp and MTB@HAp-MF-PU Composites sample.

Sample Name	T _{5%} (°C) ^a	T _{50%} (°C) ^b	T _{max1%} (°C) ^c	T _{max2%} (°C) ^c	Char yield (%) ^d
PU	268	332	295	404	0.3
2.5-MF-PU	261	344	303	411	2.1
5-MTB@HAp-PU	263	344	287	410	3.4
5-MTB@HAp-MF1:1-PU	266	340	305	405	4.9
5-MTB@HAp-MF1:3-PU	245	336	276	395	3.6

^{a,b}Temperature at 5%,50% weight losses.

^cThe maximum degradation rate temperature.

^dResidue yield at 900°C.

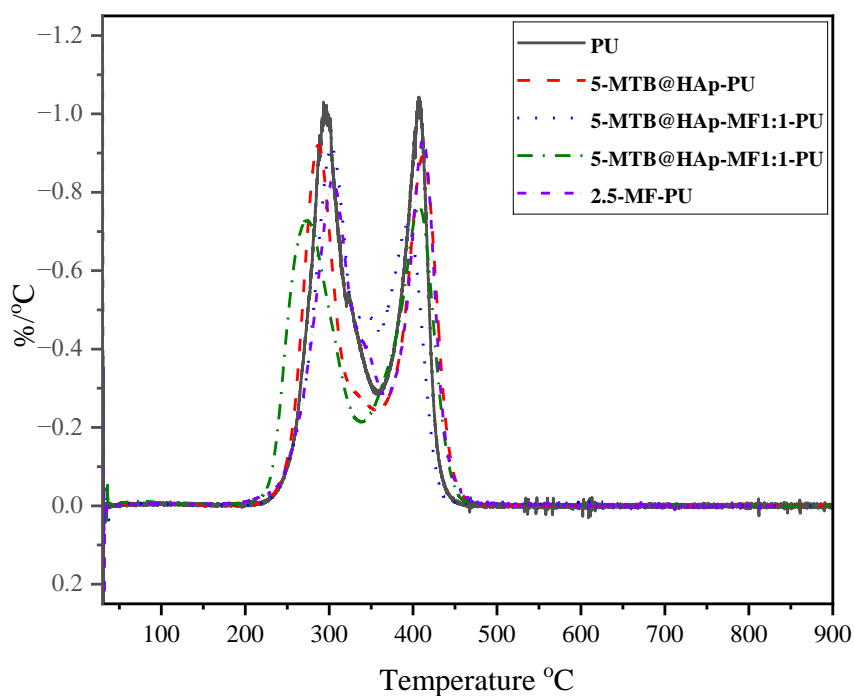


Figure 58. First derivative (DTG) curves of Neat PU and MTB@HAp-MF-PU composites.

Table 20. DTGA Data of PU, MTB@HAp-PU and MTB@HAp-MF composites.

Sample Name	T _{max1} (°C)	1.Peak Range(°C)	Δm1 (%)	T _{max2} (°C)	2.Peak Range(°C)	Δm2 (%)
PU	295	223-361	60	404	361-454	39
2.5-MF-PU	303	186-367	58	411	367-476	40
5-MTB@HAp-PU	287	216-354	48	410	354-480	44
5-MTB@HAp-MF1:1-PU	305	218-361	59	395	361-455	34
5-MTB@HAp-MF1:3-PU	276	217-335	49	406	335-470	47

T_{max1,2}, temperature of maximum rate of decomposition for the first and second steps of degradation from the DTG curve.
 Δm1,2, mass loss on the end of the first and second steps of degradation

4.2.1.2 Thermogravimetric Analysis Coupled with Fourier Transform Infrared Absorption Spectroscopy (TGA/FT-IR)

The TG and DTG curves, acquired during the TG-IR experiments performed in a nitrogen atmosphere, have been depicted in Figure 59. The results indicate that the pure PU undergoes decomposition in two distinct stages when exposed to an inert atmosphere, with the DTGmax being recorded at 298 and 404 °C.

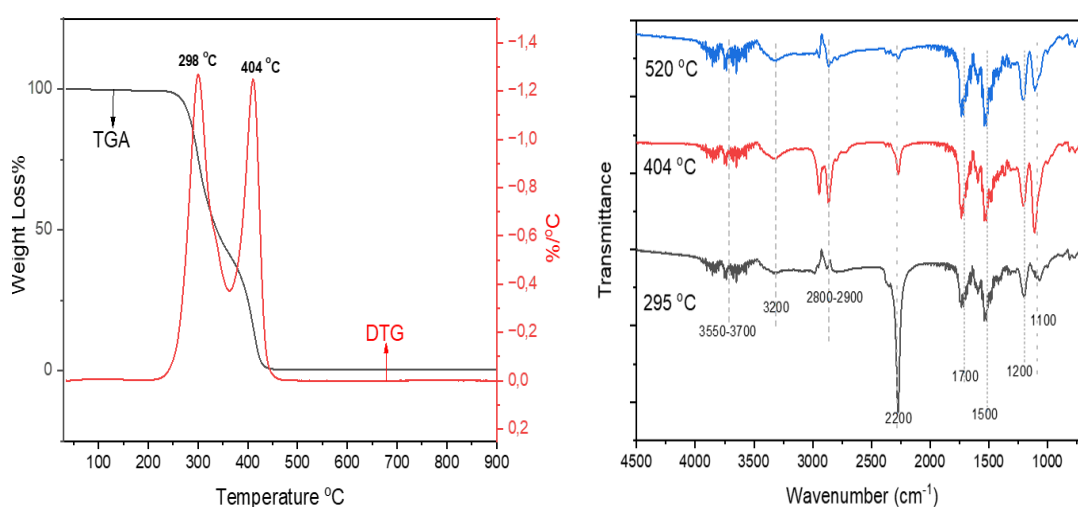


Figure 59. TGA/DTGA and FTIR of neat PU at different temperatures.

Figure 59 shows that the infrared spectra of neat polyurethane were collected at varying temperatures, including the maximum temperature of evolution rates, and at 298 °C and 404 °C, respectively, while being subjected to a nitrogen atmosphere. During the initial stage of thermal degradation at 298 °C, the release of volatile compounds is marked by specific peaks in their vibrational spectra. These include the symmetric and asymmetric stretching vibrations of N—H at 3357 cm^{-1} , the stretching vibration of —CH₂— groups at 2931 cm^{-1} , and the symmetric and asymmetric bands of C—O—C in aryl alkyl ethers, which are represented by the peaks at 1056 cm^{-1} and 1217 cm^{-1} . Furthermore, it has been verified that the peak at 2360

cm^{-1} confirms the formation of CO_2 . However, there should have been another peak detected around 2310 cm^{-1} which couldn't be identified because its vibration region overlapped with the $-\text{NCO}$ vibration region (around 2270 cm^{-1}) [111]. Additional peaks have been identified within the ranges of $3400\text{-}3900 \text{ cm}^{-1}$ and $1303\text{-}1625 \text{ cm}^{-1}$. These vibration bands strongly is associated with the presence of water vapors in the gases generated during thermal decomposition [112]. The rupture of hard segments can be attributed to the generation of substantial quantities of isocyanates ($-\text{NCO}$) and water vapor [113]. During the second stage of thermal degradation at $404 \text{ }^\circ\text{C}$, several peaks were observed in the infrared (IR) spectrum. Specifically, the peaks at 2973 cm^{-1} , 2931 cm^{-1} , and 2877 cm^{-1} can be attributed to the stretching vibration of $-\text{CH}_3$, $-\text{CH}_2$, and $-\text{CH}$, respectively. It is noteworthy that these peaks exhibited a significant increase in intensity with increasing temperature [2]. The additional products display the typical bands of CO_2 at 2366 cm^{-1} and 2327 cm^{-1} , along with the presence of a carbonyl group ($-\text{C}=\text{O}$) at 1745 cm^{-1} . Thus, the formation of tert-butyl groups ($-\text{C}-(\text{CH}_3)_3$) is suggested by the peaks identified at 910 cm^{-1} , 1375 cm^{-1} , and 1452 cm^{-1} . Furthermore, the presence of a range of ether types is indicated by the peaks at 1662 cm^{-1} for vinyl ethers, and the peaks at 1022 cm^{-1} and 1278 cm^{-1} for the symmetric and asymmetric absorption bands of $\text{C}-\text{O}-\text{C}$ in aryl alkyl ethers [113]. Lastly, the $\text{C}-\text{O}-\text{C}$ stretching vibration of ethers exhibits the strongest absorption peak at 1108 cm^{-1} due to high polarity. Therefore, in the second stage of degradation, the ether polyols obtained in the first stage undergo decomposition, resulting in the generation of methyl, methylene, methine, carbonyl groups, and carbon dioxide [2]. FTIR spectrum was taken at $520 \text{ }^\circ\text{C}$, which is after second stage degradation. The peaks at 2973 cm^{-1} , 2931 cm^{-1} , and 2877 cm^{-1} , which correspond to the stretching vibration of $-\text{CH}_3$, $-\text{CH}_2$, and $-\text{CH}$, respectively, decrease in intensity as the temperature increases. At 520°C , the formation of CO_2 also decreases, as evidenced by the peak at 2360 cm^{-1} . This suggests that the carbonaceous material undergoes rapid evolution after polyol degradation at $400 \text{ }^\circ\text{C}$. Based on the TGA-FTIR data about MTB-PU, it was observed that the initial stage degradation temperature of the composites decreased in comparison to neat PU.

However, in the second stage, the degradation of the composites became more stable and consistent than that of neat PU.

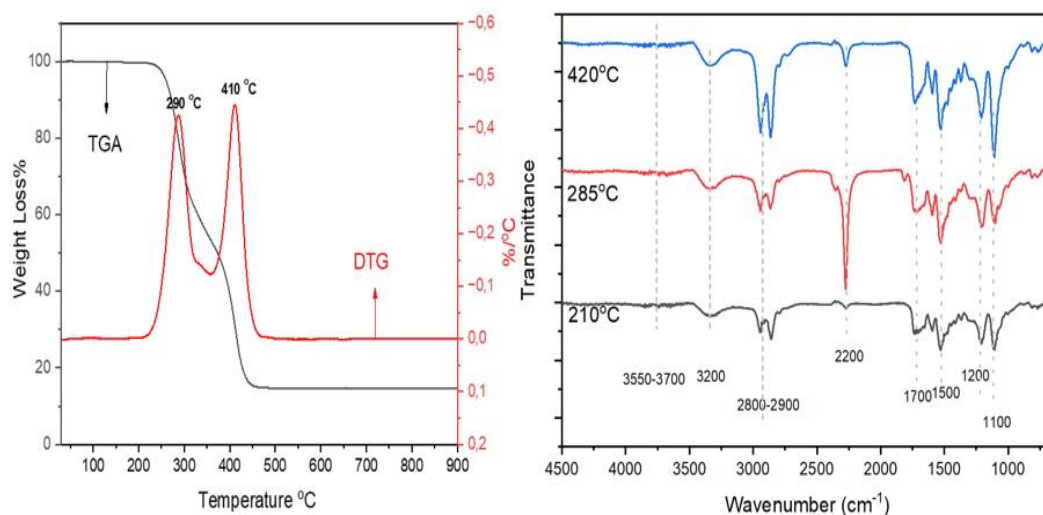


Figure 60. TGA/DTGA and FTIR of 10-MTB-PU composite at different temperatures.

Figure 60 shows that the IR spectra of 10-MTB-PU obtained at the maximum temperature of evolution rates, 290 and 410 °C, in nitrogen atmosphere. According to the DTGA curve, the urethane linkage begins to break before the first stage degradation, at around 210 °C. This observation is supported by the peak at 2270 cm^{-1} , which is the vibration region of $-\text{NCO}$ [111]. The rupture of the hard segment takes place as a result of the formation of substantial quantities of isocyanate and water vapor [113]. As the temperature rises, there is a corresponding increase in the peak intensity at 2270 cm^{-1} . The degradation of the urethane linkage achieves its highest level within the range of 285 °C-290 °C. Furthermore, the characteristic bands of CO_2 at 2366 cm^{-1} and 2327 cm^{-1} become increasingly prominent, along with the presence of the carbonyl group ($-\text{C}=\text{O}$) at 1745 cm^{-1} . The peaks observed at 2973 cm^{-1} , 2931 cm^{-1} , and 2877 cm^{-1} are linked to the stretching vibration of $-\text{CH}_3$, $-\text{CH}_2$, and $-\text{CH}$, respectively. These peaks display a significant increase in intensity

with rising temperatures. Interestingly, the absorption strengths of the $-\text{CH}_3$, $-\text{CH}_2$, and $-\text{CH}$ bands are most pronounced at approximately 420 °C, indicating the decomposition of the ether polyols into methyl, methylene, methine, carbonyl groups, and carbon dioxide during the second stage of degradation [113].

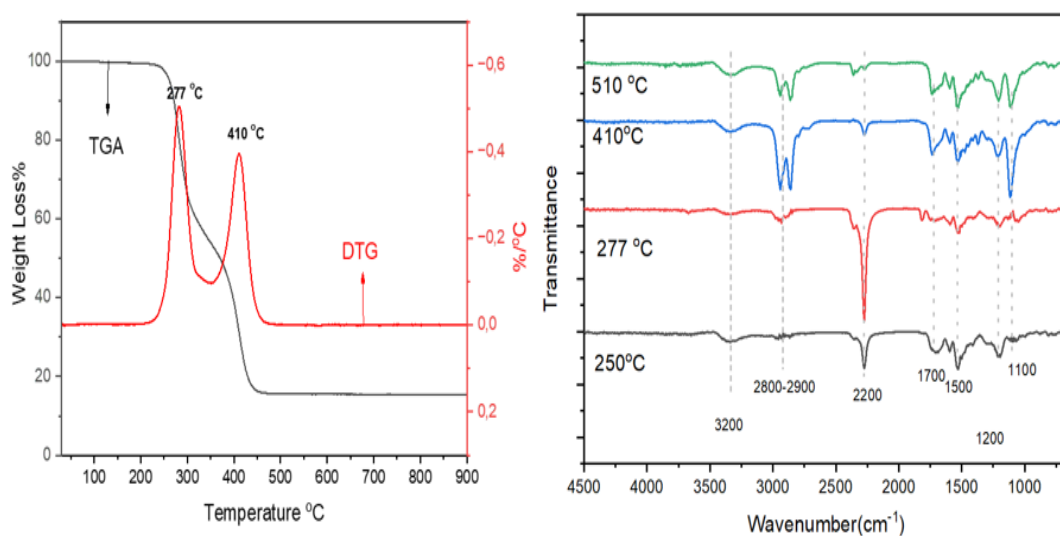


Figure 61. TGA/DTGA and FTIR of 15-MTB@HAp-PU composite at different temperatures.

Figure 61 shows TGA/DTGA and the IR spectra of 15-MTB@HAp-PU at different temperatures. At 277 °C, the gaseous products are released as a result of the decomposition of the urethane linkage which generates isocyanates ($-\text{NCO}$) and water vapor [113]. Additionally, a CO_2 band was observed in the infrared spectrum between 2200-2300 cm^{-1} . The initial peak temperature registered at 277 °C, causing the $-\text{NCO}$ vibration band to become the most prominent feature of the MTB@HAp-PU IR spectrum. As the temperature increased, the symmetric and asymmetric stretching vibrations of $\text{N}-\text{H}$ at 3357 cm^{-1} and the stretching vibrations of $-\text{CH}_2-$ groups at 2931 cm^{-1} became dominant due to the decomposition of the hard segment [18]. During the second stage of thermal degradation at 410 °C, three distinct peaks are observed at 2973 cm^{-1} , 2931 cm^{-1} , and 2877 cm^{-1} . These peaks correspond to the

stretching vibration of $-\text{CH}_3$, $-\text{CH}_2$, and $-\text{CH}$, respectively [113]. As the temperature rises to 500°C , these peaks become more pronounced. It is believed that after the second stage of thermal degradation, the amount of carbonous material in the condensed phase decreases. The resulting products exhibit the characteristic bands of CO_2 at 2366 cm^{-1} and 2327 cm^{-1} , as well as the presence of a carbonyl group ($-\text{C}=\text{O}$) at 1745 cm^{-1} . The most prominent absorption peak, detected at 1108 cm^{-1} , corresponds to the stretching vibration of C-O-C bonds in highly polar ethers. This finding provides evidence of polyol degradation, which is an essential consideration in many industrial applications [2]. At the temperature of 510°C , the infrared spectrum shows that the CO_2 band is no longer detectable between the ranges of $2200\text{-}2300\text{ cm}^{-1}$. Despite this, the specific bands of CO_2 at 2366 cm^{-1} and 2327 cm^{-1} persist, as well as the presence of a carbonyl group ($-\text{C}=\text{O}$) at 1745 cm^{-1} . These observations indicate that ether polyols, composed of methyl, methylene, methine, carbonyl groups, and carbon dioxide, undergo decomposition at the temperature of 510°C . Therefore, the urethane linkage in 15-MTB@HAp-PU decomposes earlier than neat PU. Conversely, high-temperature thermal degradation stability is improved by 10°C .

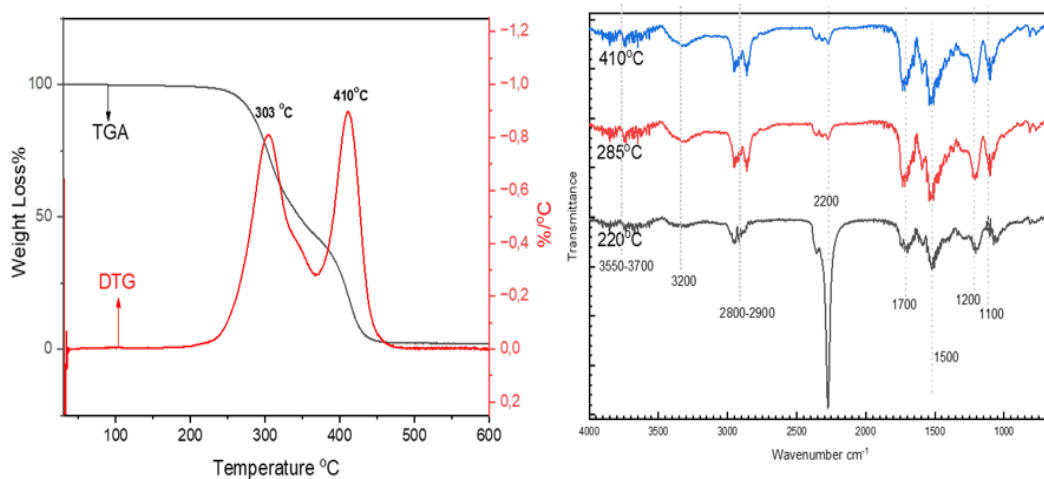


Figure 62. TGA/DTGA and FTIR of 2.5-MF-PU composite at different temperatures.

Figure 62 illustrates TGA/DTGA and FTIR of 2.5-MF-PU composite at different temperatures. When exposed to temperatures of 220 °C, the -NCO group displays a peak vibration at 2270 cm⁻¹, indicating the breakdown of the urethane linkage. This particular absorption band vanishes before it reaches a temperature of 285 °C. The wider absorption bands situated at 3322.9 cm⁻¹ and 3389 cm⁻¹ are identified as the symmetric and asymmetric stretching vibrations of N-H for the isocyanate segments, respectively. Further, the in-plane bending vibration of N-H is confirmed by the medium-strong peak at 1526.4 cm⁻¹ [112]. The absorption peaks observed at approximately 1726.3 cm⁻¹ and 1221.9 cm⁻¹ exhibit characteristic features of the stretching vibration of esters C=O and asymmetric stretching vibration of C-O (from N-CO-O), respectively [113]. For soft segment polyether polyols, there exist weak absorption peak groups near 2979.5 cm⁻¹, 2929 cm⁻¹, and 2873 cm⁻¹, which are attributed to the stretching vibration of C-H in methyl, methylene, and methylene. It is noteworthy that this absorption peak resurfaces and intensifies with the rise in temperature from 280 °C to 310 °C. The peak with the highest vibration strength of -NCO at 2270 cm⁻¹ vanishes during the temperature range of 280 °C to 310 °C, indicating that the isocyanate monomers evaporate entirely from the PU composite. A CO₂ band was detected in the range of 2200-2300 cm⁻¹. At a temperature of 410 °C, the stretching vibration of the C-O-C bond in ethers was observed as the most intense absorption peak at 1108 cm⁻¹, which provides evidence of polyol degradation.

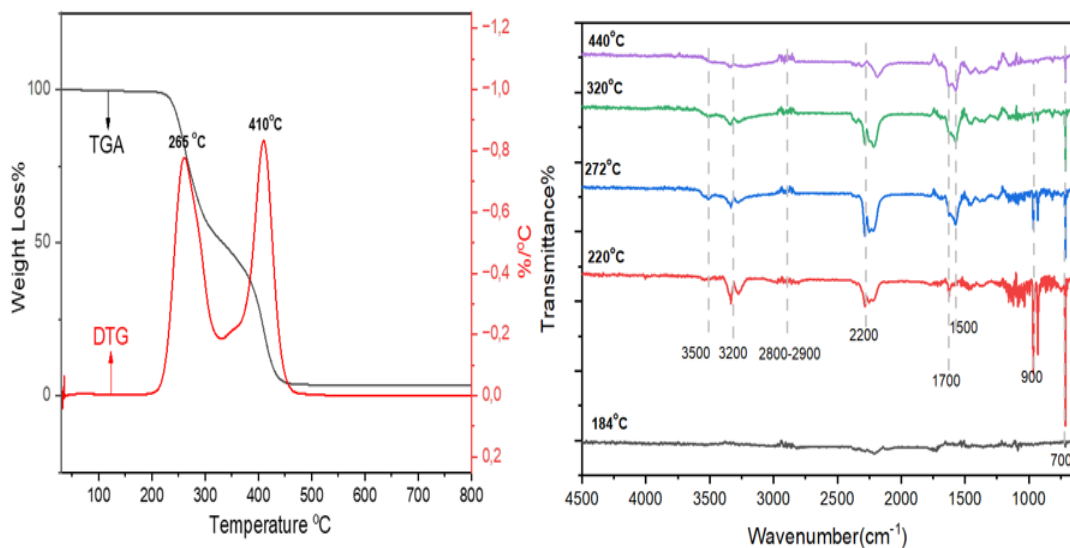


Figure 63. TGA/DTGA and FTIR of 5-MTB-MF1:3-PU composite at different temperatures.

TGA/DTGA and FTIR of 5-MTB-MF1:3-PU composite is shown in Figure 63 at different temperatures. At temperature of 184 °C, the IR spectrum of 5-MTB-MF1:3-PU was obtained, which revealed the detection of weak absorption peaks of CO₂ and C=O at 2200 cm⁻¹ and 1700 cm⁻¹, which suggests the decomposition of filler prior to urethane linkage decomposition [97]. At temperatures above 184 °C, there is a strengthening of the CO₂ band, with an increase in temperature up to 222 °C. The vibration peak of -NCO at 2280 cm⁻¹ is observed as weak absorption, which confirms the initiation of thermal degradation of the urethane linkage [113]. The infrared spectra were captured at 272 °C, the temperature at which the rate of evolution peaks. The vibration peak assigned to -NCO at 2270 cm⁻¹ was observed to resurface and strengthen. Furthermore, the broad absorption bands in the vicinity of 3322.9 cm⁻¹ and 3389 cm⁻¹ corresponded to the symmetric and asymmetric stretching vibrations of N-H in the isocyanate segments. The in-plane bending vibration of N-H was also confirmed by the medium-strong peak at 1526.4 cm⁻¹. The infrared spectrum analysis of the sample reveals sharp absorption peaks at approximately 1726.3 cm⁻¹, which are indicative of the stretching vibration of esters C=O and the asymmetric stretching

vibration of C-O (from N-CO-O). Additionally, other peaks were detected between 3200-3500 cm^{-1} , which refers the presence of water vapor or decomposed gases [2]. Upon the rupture of hard segments in polyurethane, a significant amount of isocyanate and water vapor is generated. However, within the temperature range of 272°C to 320 °C, the absorption bond at 2280 cm^{-1} is observed to almost disappear completely. This observation indicates that the isocyanate monomers have fully evaporated from the polyurethane residue. At the second step degradation with max rate is shown in Figure 63, the gradual reduction in the absorption band intensities that correspond to the polyol segments suggests a degradation of the polyols [113].

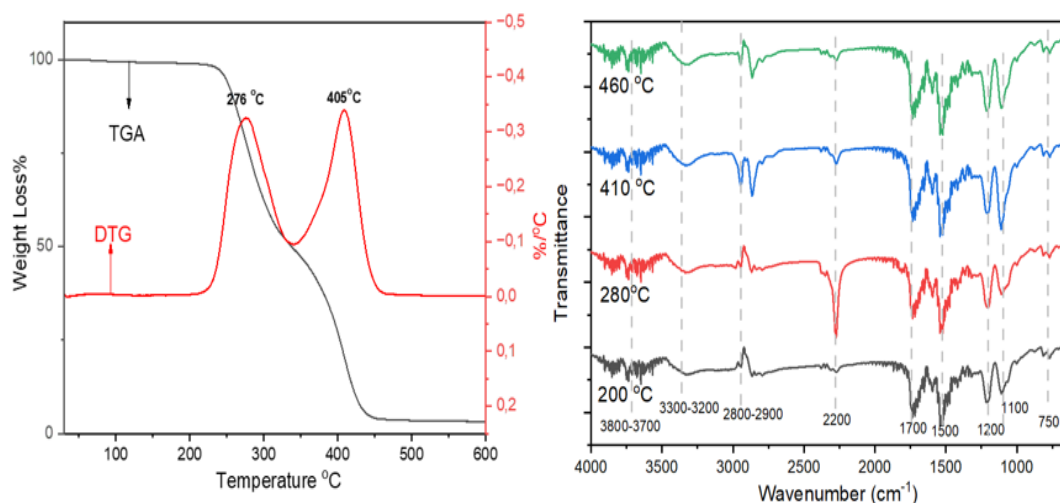


Figure 64. TGA/DTGA and FTIR of 5-MTB@HAp-MF1:3-PU composite at different temperatures.

Figure 64 shows TGA/DTGA and FTIR of 5-MTB@HAp-MF1:3-PU composite at different temperatures. Particularly, the IR spectra obtained at the maximum temperature of evolution rates, 280 °C and 410 °C. t a temperature of 200 °C, which is below the temperature at which the first step degradation with the maximum rate occurs (280 °C), it is possible to observe the symmetric and asymmetric characteristic stretching vibrations of N—H at 3357 cm^{-1} . Moreover, the vibration bands of water vapor from the decomposed gases can be observed in the range of 3200-3500 cm^{-1} and 1300-1600 cm^{-1} [2]. The CO₂ bands at 2366 cm^{-1} are evident in the other

products. However, in the temperature range of 200°C to 280°C, the hard segments disintegrate, leading to the formation of considerable amounts of isocyanates, which are detectable in the decomposition residues at 2270 cm⁻¹. Furthermore, the stretching vibration of —CH₂— groups at 2931 cm⁻¹ and the symmetric and asymmetric bands of C-O-C in ether become more detectable with increasing temperature. The observed peaks in the thermal analysis data suggest that the degradation of polyurethane starts with the rupture of the urethane bond at 220°C [2]. During the second stage of degradation, which occurs at a temperature of 410°C, the stretching vibrations of the organic functional groups —CH₃, —CH₂, and —CH were observed at wavenumbers of 2973 cm⁻¹, 2931 cm⁻¹, and 2877 cm⁻¹, respectively. These peaks exhibited a significant increase with the increase in temperature [113]. Other products have CO₂ characteristic bands present at 2366 cm⁻¹ and 2327 cm⁻¹, as well as an ester carbonyl group (—C=O) at 1745 cm⁻¹. The formation of tert-butyl groups (—C(CH₃)₃) is suggested by peaks at 910 cm⁻¹, 1375 cm⁻¹, and 1452 cm⁻¹. Evidence of various ethers is also present, as demonstrated by peaks at 1662 cm⁻¹ for vinyl ethers and at 1022 cm⁻¹ and 1278 cm⁻¹ for the symmetric and asymmetric C—O—C absorption bands in aryl alkyl ethers [112]. The observed disappearance of the absorption bond at 2280 cm⁻¹ suggests that the isocyanate monomers have evaporated from the polyurethane (PU) system, leading to the onset of polyol degradation. At temperatures exceeding 410 °C, the weakening of the absorption bands corresponding to the polyol segments signifies the degradation of polyols.

4.2.2 LOI and UL-94 Analyses of PU Composites

The limiting oxygen index and vertical burning test are effective methods for determining a material's flame retardancy. A higher LOI value indicates stronger ignition resistance in environmental conditions. In the plastics industry, LOI and UL94 tests are crucial screening and quality control methods. According to literature, LOI value of neat polyurethane, produced from polyether polyol and aromatic isocyanate (TDI), was measured ~22% [107, 23]. Figure 65 shows LOI index and

UL-94 rating of neat PU and MTB containing PU composites. Compared with pure PU, LOI values of the 5-MTB-PU, 10-MTB-PU, 15-MTB-PU and 20-MTB-PU increased from 22% to 24.5%, 25.0%, 23.5% and 23.5%, respectively. In addition, dripping of MTB-PU decreased significantly, even if it has melt dripping. Nevertheless, MTB-PU composites failed to achieve V-0 in the UL-94 test.

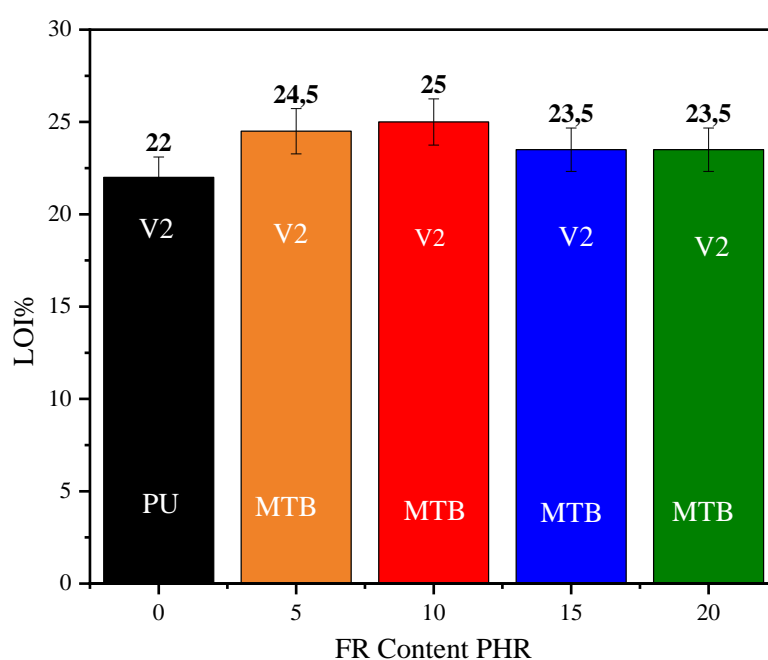


Figure 65. LOI and UL-94 rating of MTB containing PU composites.

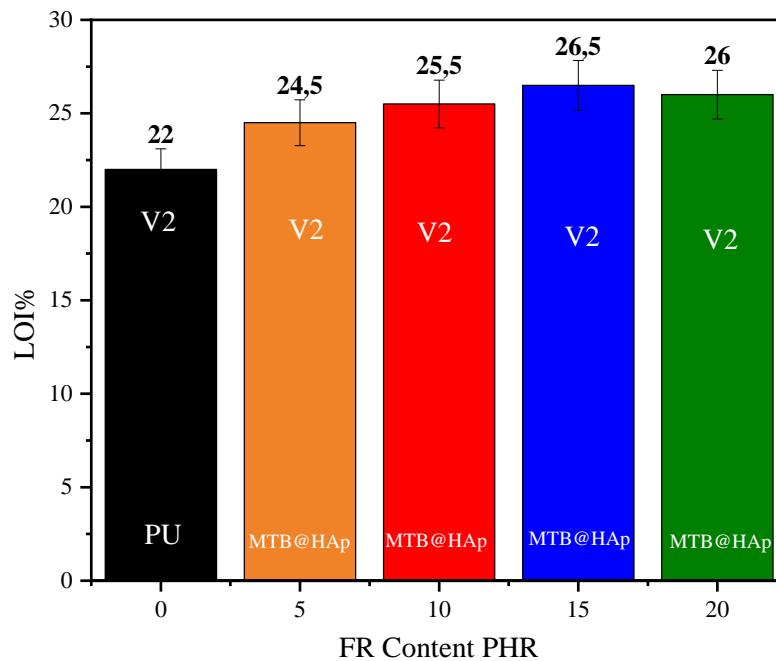


Figure 66. LOI and UL-94 rating of MTB@HAp containing PU composites.

LOI% and UL-94 rating results of MTB@HAp-PU composites are given in Figure 66. The addition of MTB@HAp with 5, 10, 15 and 20 PHR to PU increases LOI value from 22% to 24.5, 25.5, 26.6 and %26 respectively. Modification of MTB with HAp to obtain core shell structure increased the LOI% for 26.5% with 15PHR of MTB@HAp-PU. When the amount of MTB@HAp containing MTB@HAp-PU composite exceeds 15PHR, LOI value decreases and becomes stable at 26%. However, UL-94 rating was not achieved to V0 with lower dripping.

The appendices section includes a detailed analysis of the LOI% and UL-94 rating measurements conducted on HAp-PU composites. (Figure A. 2 and Figure B. 2).

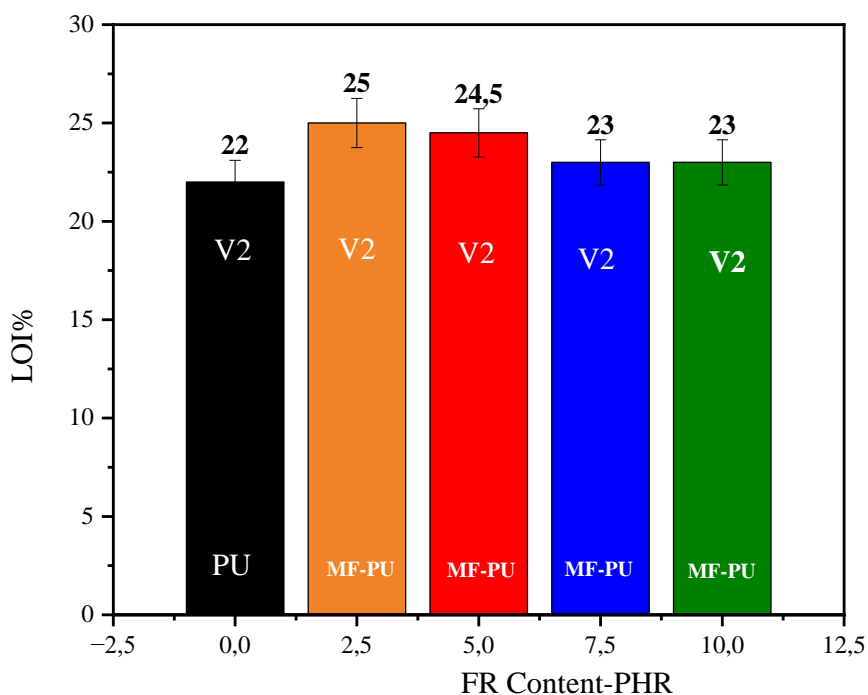


Figure 67. LOI and UL-94 rating of MF containing PU composites.

Melamine formaldehyde resin (MF) is a type of thermoset polymer that possesses inherent flame retardancy, which sets it apart from highly flammable polymers. Melamine formaldehyde (MF) resin was used as microcapsule with MTB and MTB@HAp. Flame retardancy of MF without any core (MTB and MTB@HAp) was tested by LOI and UL-94V measurements. LOI data of MF resin containing PU composites are shown in Figure 67. The LOI value of MF-PU microcapsule composites were 25%, 24.5%, 23% and 23% for the mass ratio of MF-PU microcapsules were 2.5PHR, 5PHR, 7.5PHR and 10PHR, respectively. The UL-94 test results indicated that the MF-PU composites achieved a V2 rating, similar to that of pure PU. Nonetheless, the amount of dripping observed during the test was significantly reduced in the MF-PU composites compared to pure PU. This decrease

in dripping can be attributed to a lower degree of carbonization, as evidenced by the char residue percentage in TGA.

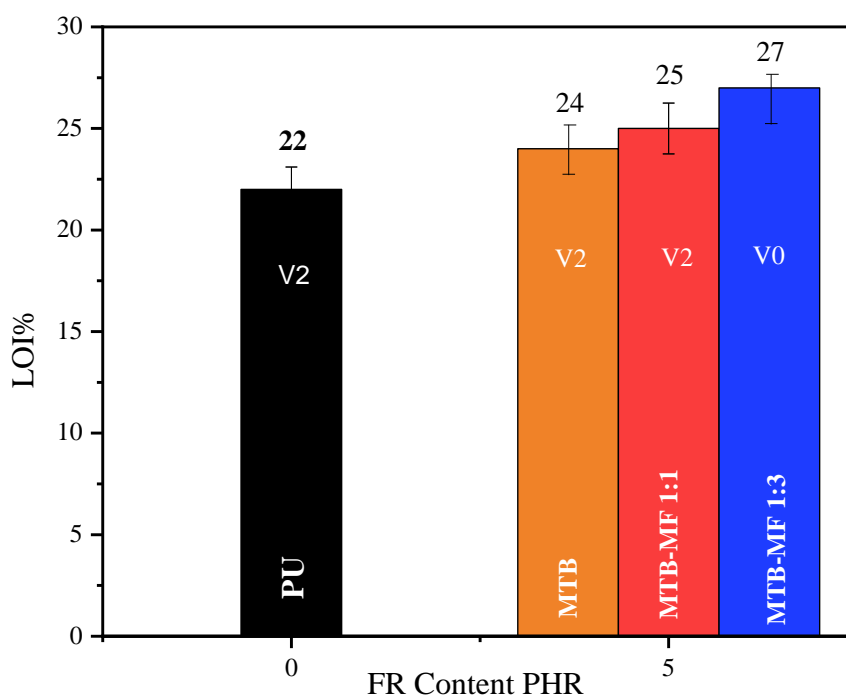


Figure 68. LOI and UL-94 rating of MTB-MF microcapsule containing PU composites.

In previous results, the LOI value of neat PU and 5-MTB-PU and 5-MTB@HAp-PU were given as 22%, 24% and 24.5%, respectively. The dripping phenomenon was barely eliminated and UL-94 rating unchanged as V2. In Figure 68, a comparison is presented between the LOI values and UL-ratings of MTB and micro-capsulated MTB, with varying MF ratios. When the content of MTB-MF microcapsules with MF ratios of 1:1 and 1:3 was 5PHR in PU composites, the LOI value significantly increased and reached 27% from 22%. The dripping phenomenon was eliminated with MF addition to MTB. When the mass content of MF resin in MTB-MF reaches a ratio of 1:3, a UL-94 vertical test was conducted on 5-MTB-MF-PU with 25%

concentration, resulting in a V-0 rating. Furthermore, the LOI value increased to 27.0%.

The appendices section includes a detailed analysis of the LOI% and UL-94 rating measurements conducted on 10PHR, 15PHR and 20PHR MTB-MF-PU composites, which is illustrated in Figure C. 2 and Figure D. 2.

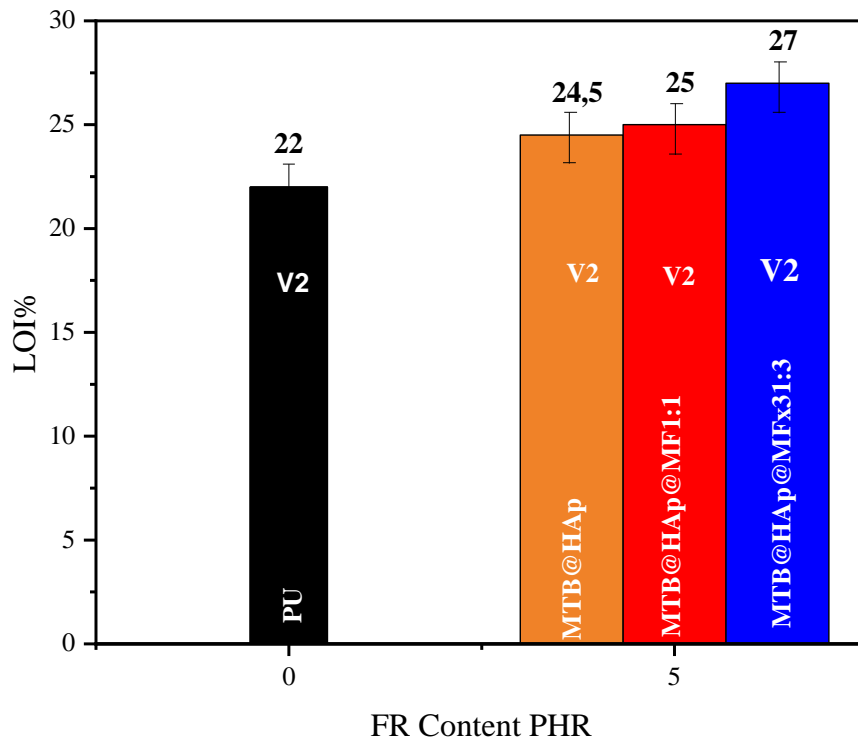


Figure 69. LOI and UL-94 rating of MTBMTB@-MF microcapsule containing PU composite.

Similarly, MF microencapsulation has effects on LOI value of MTB@HAp-PU is observed in Figure 69. By adding MTB@HAp-MF microcapsules with MF ratios of 1:1 and 1:3 to PU composites at a 5PHR content, the LOI value increased significantly from 22% to 27%. Additionally, the dripping phenomenon was eliminated by incorporating MF into MTB@HAp. The dripping was significantly

eliminated with MF addition to MTB@HAp. However, the UL-94 rating of MTB@HAp-MF-PU remained unchanged.

The appendices section includes a detailed analysis of the LOI% and UL-94 rating measurements conducted on 10PHR, 15PHR and 20PHR MTB@HAp-MF-PU composites, which is shown in Figure E. 2 and Figure F. 2.

Table 21. LOI value and UL 94 rating of PU samples.

Sample Name	LOI%	Δ LOI	UL-94	Burning Behavior UL-94V (t ₁ + t ₂)
Neat PU	22	0	V2	10+4-Excess dripping
5-MTB-PU	24.5	2.5	V2	8+1-(Dripped)
10-MTB-PU	25	3.0	V2	6+1-(Dripped)
15-MTB-PU	23.5	1.5	V2	15+2-(Dripped/Dropped)
20-MTB-PU	23.5	1.5	V2	20+6-(Dripped/Dropped)
5-MTB@HAP-PU	24.5	2.5	V2	4+3-(Dripped)
10-MTB@HAP-PU	25.5	3.5	V2	1+2-(Dripped)
15-MTB@HAP-PU	26	4.5	V2	1+3-(Dripped)
20-MTB@HAP-PU	24.5	2.5	V2	13+6-(Dripped/Dropped)
2.5-MF-PU	25	3.0	V2	2+3-(Dripped)
5-MF-PU	24.5	2.5	V2	2+0-(Dripped)
7.5-MF-PU	23	1.0	V2	3+3-(Dripped)
10-MF-PU	23	1.0	V2	5+3-(Dripped)
5-MTB-MF (1:1)-PU	25	3.0	V2	0+0-(Dripped-Charring)
5-MTB-MF (1:3)-PU	27	5.0	V0	0+0- (No Dripping-Charring)
5-MTB@HAp-MF (1:1)-PU	25	3.0	V2	1+0-(Dripped-Charring)
5-MTB@HAp-MF (1:3)-PU	27	5.0	V2	0+0-(Dripped-Charring)

Δ LOI: LOI = LOI-LOI (Neat PU)

4.2.3 Mass Loss Calorimeter Analyses of PU Composites

Mass Loss calorimetry (MCL) is an effective approach to evaluate the combustion behavior of flame retarded polymers. The heat release rate is a critical factor that determines the intensity of a fire. It measures the amount of heat released per unit

area when a material is ignited under a specific incident heat flux. A higher number indicates that more heat is released during the combustion process, leading to a higher risk of fire [42]. Total Heat Evolve (THE) is defined as total energy released combustion of gases during the decomposition of polymeric material [114]. Heat release rate (HRR) and total heat evolved (THE) data for PU samples are listed in Table 22.

Table 22. Mass Loss calorimeter data of PU composite samples.

Sample Name	TTI (sec)	P-HRR (kW/m ²)	av HRR (kW/m ²)	THE (MJ/m ²)
PU	30	350	172	105
5-MTB-PU	26	328	186	94
10-MTB-PU	40	245	155	45
15-MTB-PU	55	231	139	46
20-MTB-PU	83	224	135	53
5-MTB-MF (1:1)-PU	20	108	51	27
5-MTB-MF (1:3)-PU	30	70	42	16
5-MTB@HAP-PU	35	238	115	47
10-MTB@HAP-PU	35	294	136	66
15-MTB@HAP-PU	42	280	146	57
20-MTB@HAP-PU	30	260	134	45
5-MTB@HAp-MF (1:1)-PU	30	150	83	41
5-MTB@HAp-MF (1:3)-PU	30	136	78	37

The heat release rate (HRR) curves of MTB-PU composites are shown in Figure 70. Pure PU rapidly melts and burns, and its peak HRR (PHRR) and THE are 350 kW/m² and 105 MJ/m², respectively. 5-MTB-PU composite showed a broad peak at 225 sec, and the PHRR was 328 kW/m². But average HRR and THE increases with respect to pure PU. It is explained by rapid melting and dripping out of PU from sample holder during the measurement. In the same way, melting of PU may affect time to

ignition (TTI), which is larger than TTI of 5-MTB. It can be also seen from Figure 70, the PHRR values of 10-MTB-PU, 15-MTB-PU and 20-MTB-PU decreased to 245 kW/m², 231 kW/m², 224 kW/m², respectively. THE values of the samples are reduced to 45 kW/m², 42 kW/m² and 53 kW/m² from 105 kW/m². The reason why the MTB causes reduction at PHRR and THR is that PU degrades by the formation of thin black film and MTB particles are integrated into the char and increases the barrier effect of the char and PHRR values are reduced [115]. However, the addition of MTB reduces the THE and PHRR values of PU, but the reduction is not meaningful.

The effect of microencapsulation of MTB with MF (1:1 and 1:3) on PU can be seen by CC measurement, which is given in Figure 71. The heat release rate (HRR) curves of 5-MTB-PU, 5-MTB-MF (1:1)-PU, 5-MTB-MF (1:3)-PU composites and neat PU are compared in Figure 71. The addition of 5PHR of MTB provides a slightly decrease in PHRR curves from 350 kW/m² to 328 kW/m². Yet, The PHRR value of PU composites containing MTB-MF microcapsules decrease rapidly. Besides, the form of HRR curves of MTB-MF (1:1) and MTB-MF (1:3) become broad and PHRR are 108 and 70 kW/m², respectively. In the same way, THE value of MF microcapsules is significantly diminished from 70 MJ/m² to 16 MJ/m², which indicates inhibition of flame. As the MF content increases, the PHRR values of 5-MTB-MF-PU decreases to 16 MJ/m². This was consistent with the LOI and Vertical Burning test results were given in Table 21. However, introducing MF resin to MTB is not able to enhance char formation for preventing combustible gases. Thus, flame retardant effect of MF microcapsules may work at gas phase rather than condensed phase [114]. The appendices section includes MLC measurements conducted on 10PHR, 15PHR and 20PHR MTB-MF-PU composites. HRR curves are illustrated in Figure C. 1 and Figure D. 1.

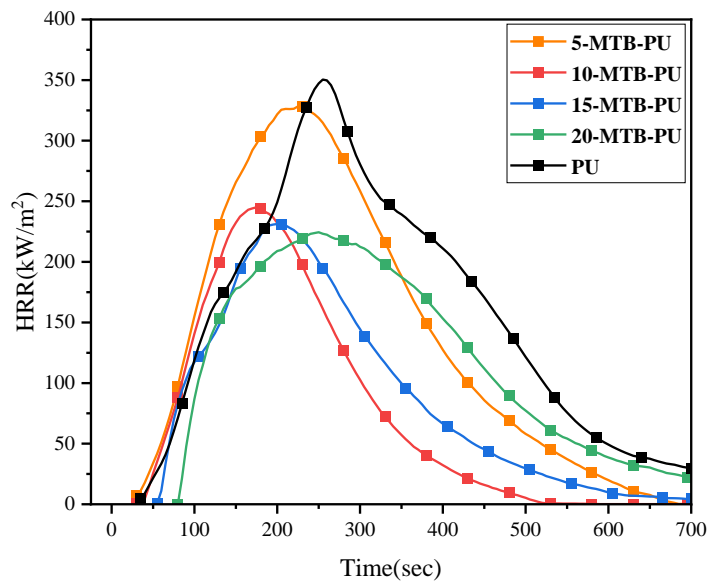


Figure 70. HRR curves of MTB-PU composites.

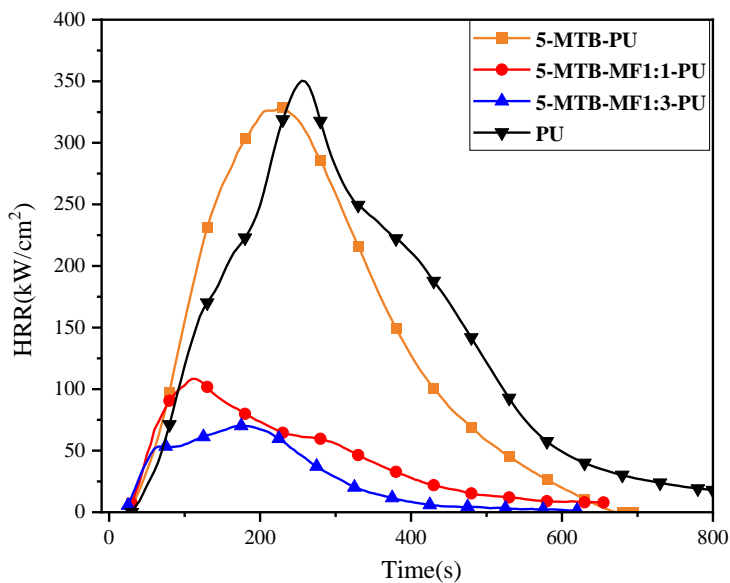


Figure 71. HRR curves of MTB-MF-PU composites.

Figure 72 depicts the HRR curves for MTB@HAp-PU core shell structure at varying content (0 to 20PHR). MTB@HAp-PU composites show smaller PHRR than pure.

PHRR of 5-MTB@HAp-PU is 115 kW/m², which is the smallest peak in MTB@HAp-PU composites. 5-MTB@HAp-PU showed a small peak, which was much lower than that of pure PU. The PHRR values of 10-MTB@HAp-PU, 15-MTB@HAp-PU and 20-MTB@HAp-PU are 136 kW/m², 146 kW/m², 134 kW/m², respectively. Increasing amounts of MTB@HAp in PU changed pPHRR slightly. Accordingly, the PHRR values of the MTB@HAp-PU composites are comparable to those of the MTB-PU. In addition, THE is notably reduced with the inclusion of 5- MTB@HAp according to PU. However, adding more MTB@HAp to PU does not result in a corresponding increase in THE concentration. These results show that the PU degrades by the formation of thin black film and MTB@HAp particles are integrated into the char and increases the barrier effect of the char [115].

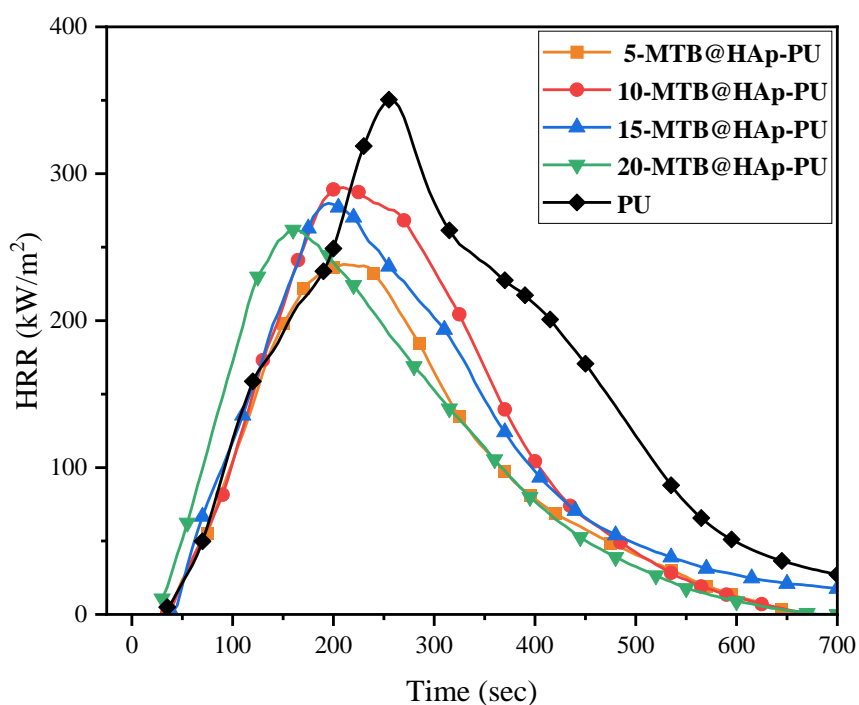


Figure 72. HRR curves of MTB@HAp-PU composites.

Figure 73 depicts HRR curves of 5-MTB@HAp-PU and MTB@HAp-MF composites. PHRR values of 5-MTB@HAp-PU, 5-MTB@HAp-MF (1:1)-PU, and 5-MTB@HAp-MF (1:3)-PU are 238 kW/m², 150 kW/m², and 136 kW/m², respectively. The lowest maximum HRR and THR values are obtained with addition of MF (1:3) encapsulated MTB@HAp containing composite. The maximum HRR decreases from 358 kW/m² to 136 kW/m² and THR decreases from 105 to 37 MJ/m². Besides, the composite of MTB@HAp-PU and PU has the highest burning time and therefore the lowest average HRR value. MF microcapsule composites did not fully combust, but MF protects the underlying matrix of polymer from combustible gas from feeding the flame in gas phase dilution[40]. Moreover, MTB@HAp may synergic effects to integrate into the char and increases the barrier effect of the char in polymer matrix [75]. The appendices section includes conic calorimeter measurements conducted on 10PHR, 15PHR and 20PHR MTB@HAp-MF-PU composites. HRR curves are illustrated in Figure E. 1 and Figure F. 2.

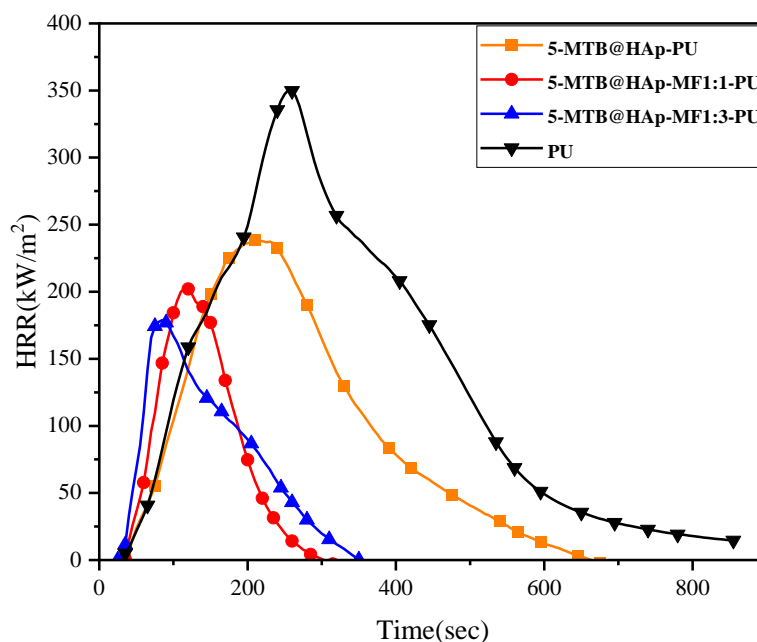


Figure 73. HRR curves of MTB@HAp-MF-PU composites.

To compare burning performances of MTB-MF-PU and MTB@HAp-MF-PU, PHRR and THE values of the composites were investigated. The values for PHRR and THE of MTB-MF-PU are reduced to 40% with respect to MTB@HAp-MF-PU. This phenomenon can be explained by MF content on core materials. According to TGA results given in Figure 44 and Figure 46, encapsulated MF content on MTB is higher than MTB@HAp. By increasing the content of MF microcapsules, the efficiency of flame retardancy in MTB-MF-PU composites can be improved. This is achieved by generating more non-flammable gases, which enhance the fire-resistant properties of the composites.

4.2.3.1 Morphology of Residual chars from Mass Loss Calorimeter

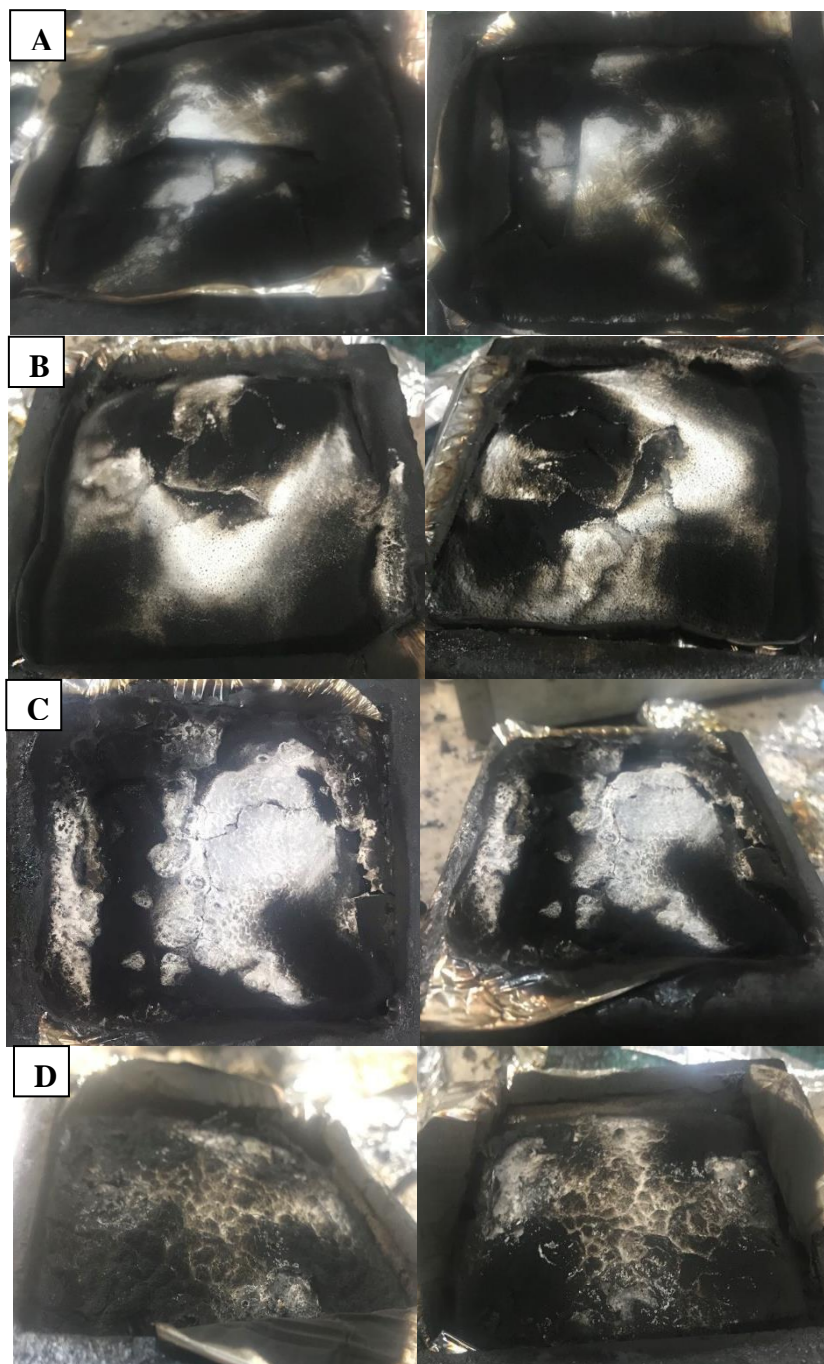


Figure 74. Images of residual chars from PU composites; A:5-MTB-PU, B:10-MTB-PU, C:15-MTB-PU, D: 20-MTB-PU.

To better understand flame retardance mechanism, digital photos and SEM analysis were used to measure microstructures of char layers and morphologies of char residues from samples after mass loss cone calorimetry tests. Figure 75 displays the residual char images of MTB-PU composites after MLC tests. PU decomposed entirely, and only a negligible amount of residual char was generated. The addition of MTB gives a significant raise in the residual char of MTB-PU. For the 10 and 15-MTB-PU composites, the remaining materials show a char layer structure with some cracks. However, when MTB content is increased to 20 PHR, the char structure becomes more compact and uniform. Additionally, the cracks in the residue are narrower compared to those found in the 10 and 15-MTB-PU composites. The compact char layer efficiently slows heat and mass transfer between the gas and condensed phases, which reduced PHRR and prolonged burning time in HRR curve (Figure 70) [116].

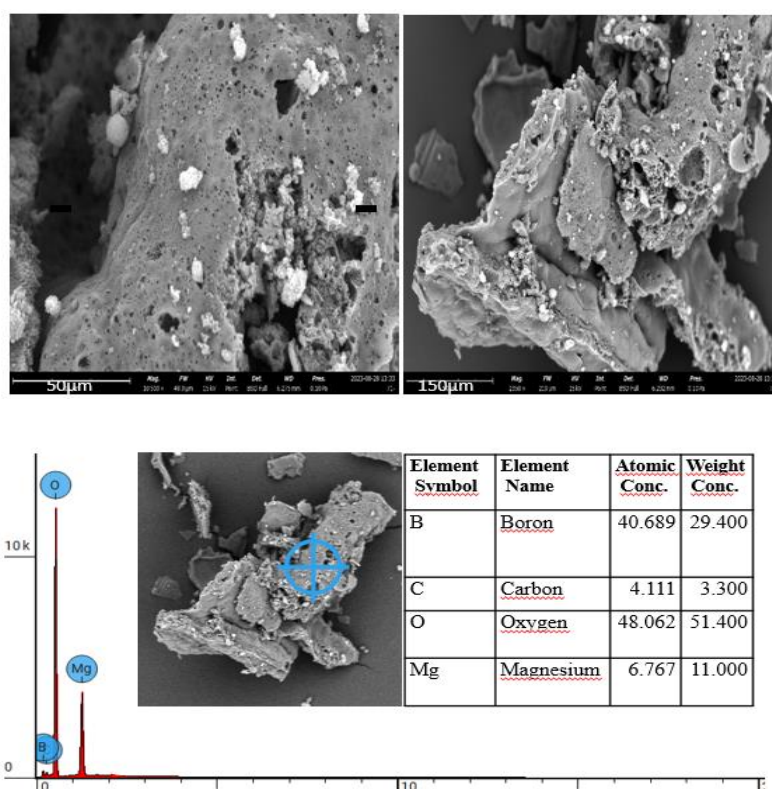


Figure 75. SEM images and EDS results of residual chars from 20-MTB-PU sample.

The SEM was used to investigate the surface and sectional microstructures of the char residue for a 20-MTB-PU composite. Figure 75 shows SEM micrograms of 20-MTB-PU sample. The morphology of residual char is like porous MTB particles. Most of the residue is MTB, as confirmed by EDS elemental analysis in Figure 75. According to the analysis, EDS found residue from MTB containing Mg, B, O and C from burning organic material-PU.

Figure 76 displays the images of char residues of the PU samples containing MTB@HAp after MLC burning. In the case of 5-MTB@HAp-PU composite, the residue presents narrow black char layer structure. When the content of MTB@HAp is increased to 20PHR, the char structure becomes thicker and more uniform while the cracks in the residue become narrower when compared to 5-MTB@HAp-PU. As a result of incorporating the core-shell structure of MTB@HAp into PU, the morphology and char formation ability are found to be quite like that of MTB. However, it is worth noting that MTB still possesses superior flame-retardant ability compared to PU. When examining the char layer of MTB@HAp-PU composites, it is evident that the surface morphology is not uniform and relatively porous illustrated in Figure 77. This structure allows heat and flammable volatiles to enter the flame zone, as the char layer is insufficient for proper combustion. The low flame-retarded ratio prevents the char from forming continuously. EDS analysis reveals that the residue of char contains high amounts of B, Ca, P, Mg, and O from MTB@HAp, as well as C from carbon-containing components.

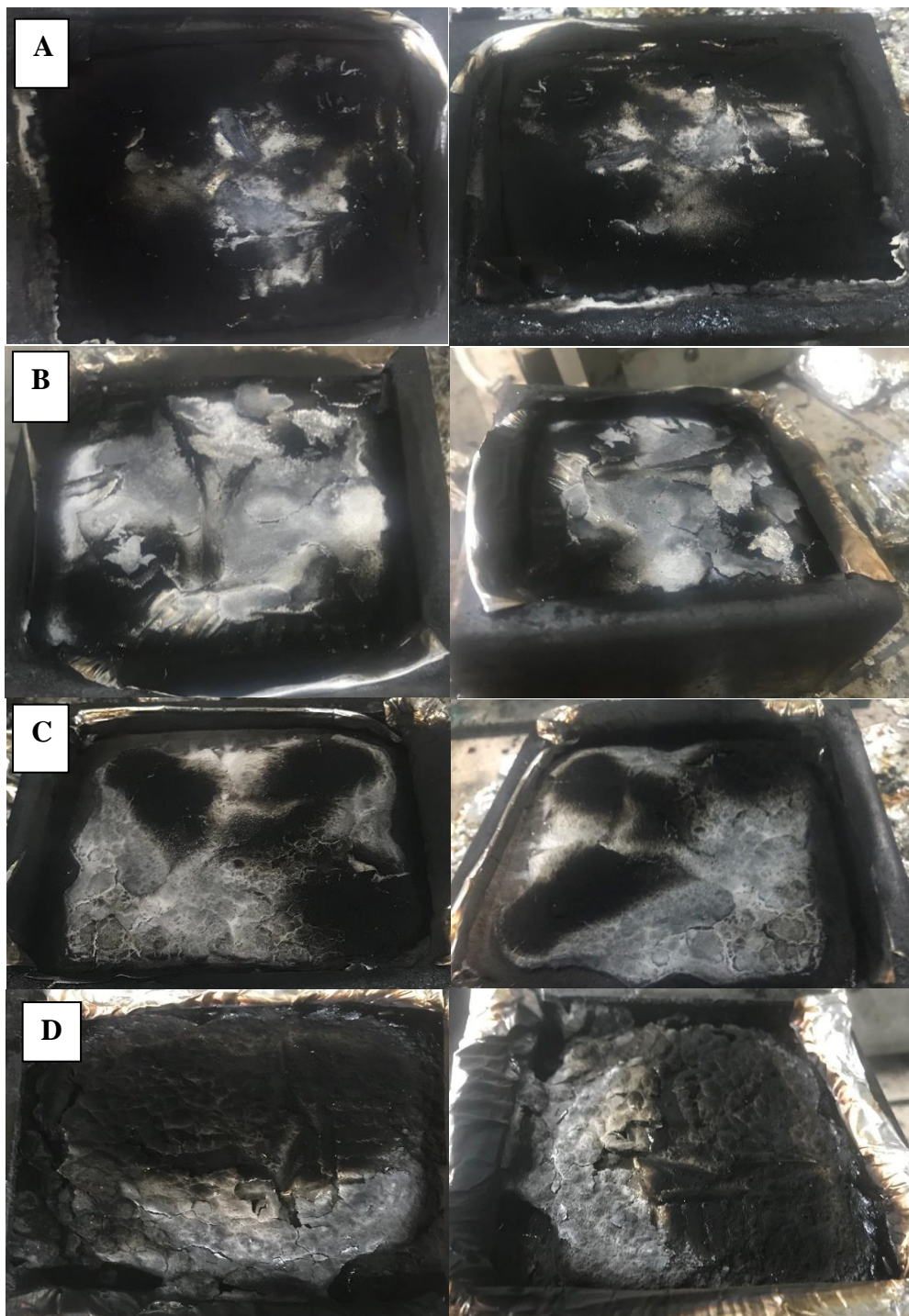


Figure 76. Images of residual chars from PU composites; A:5-MTB@HAp-PU, B:10-MTB@HAp-PU, C:15-MTB@HAp-PU, D: 20-MTB@HAp-PU.

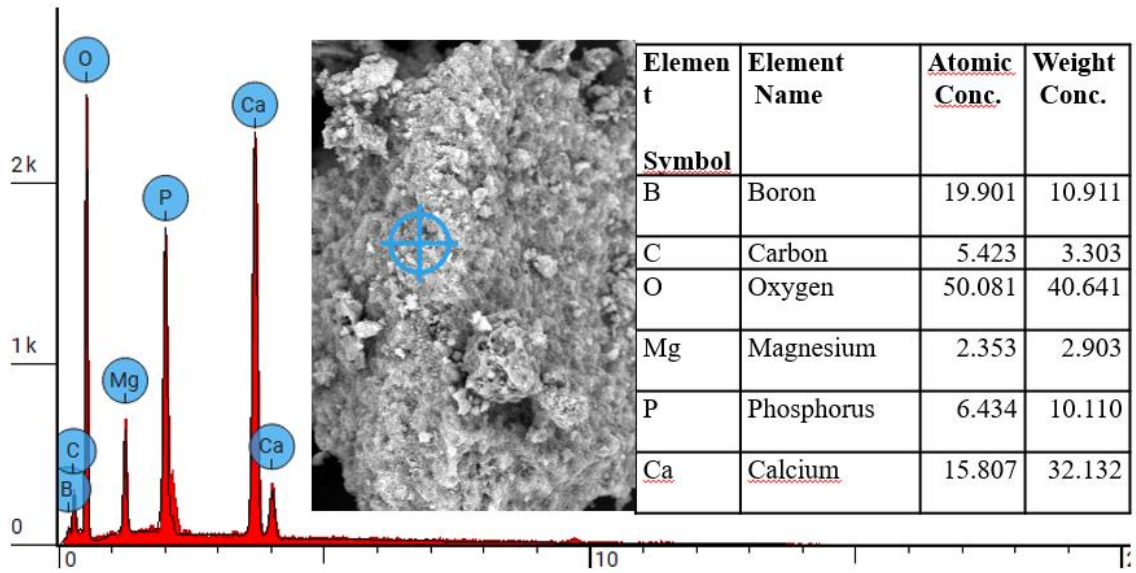
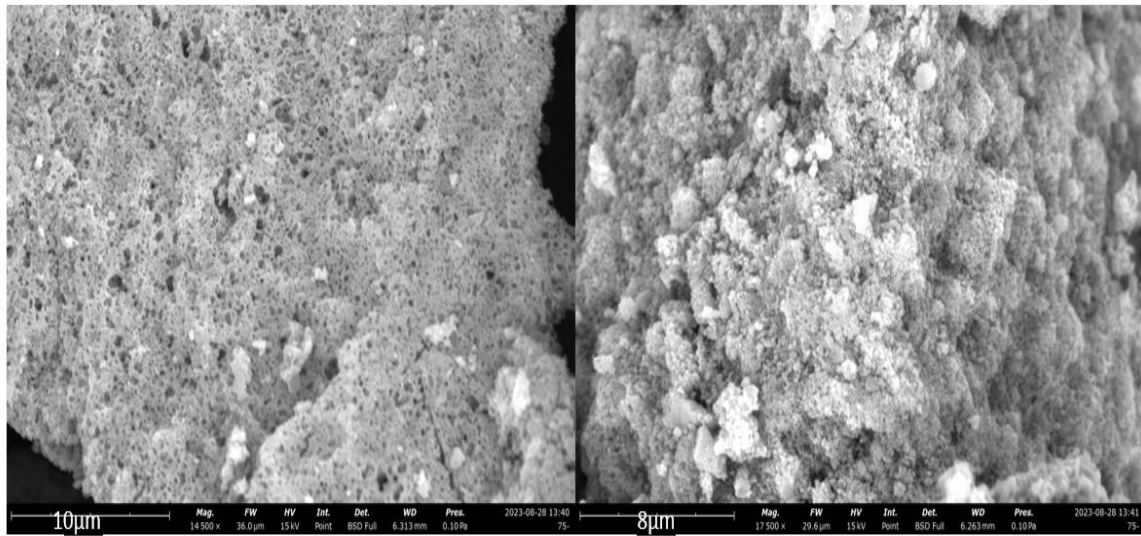


Figure 77. SEM images and EDS results of residual chars from 20-MTB@HAp-PU sample.

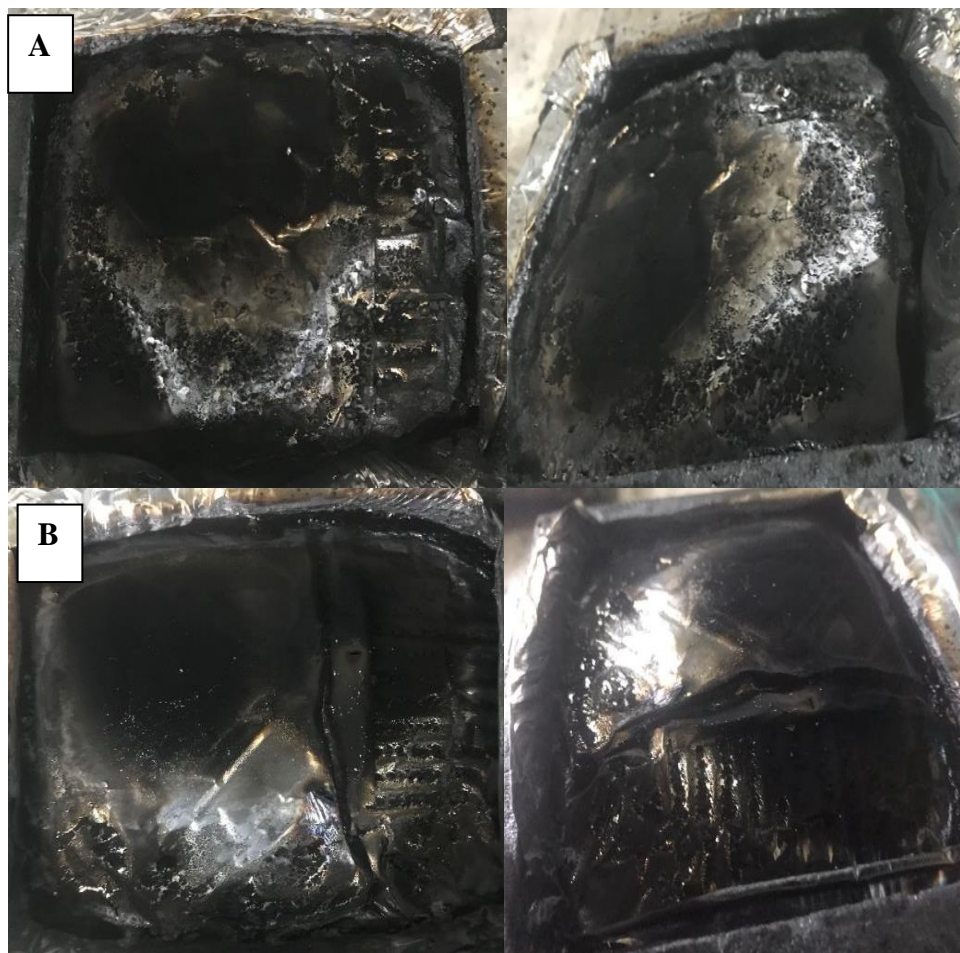


Figure 78. Images of residual chars from PU composites; A:5-MTB@HAp-MF 1:1-PU, B:5-MTB@HAp-MF 1:3-PU.

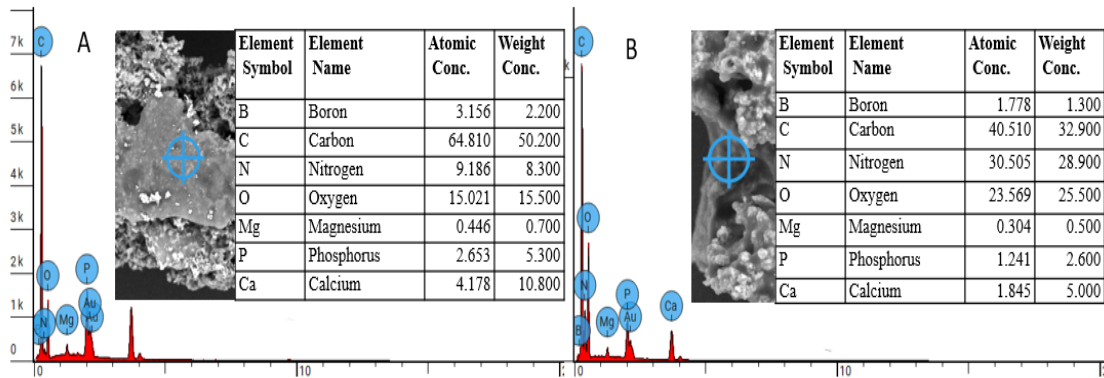
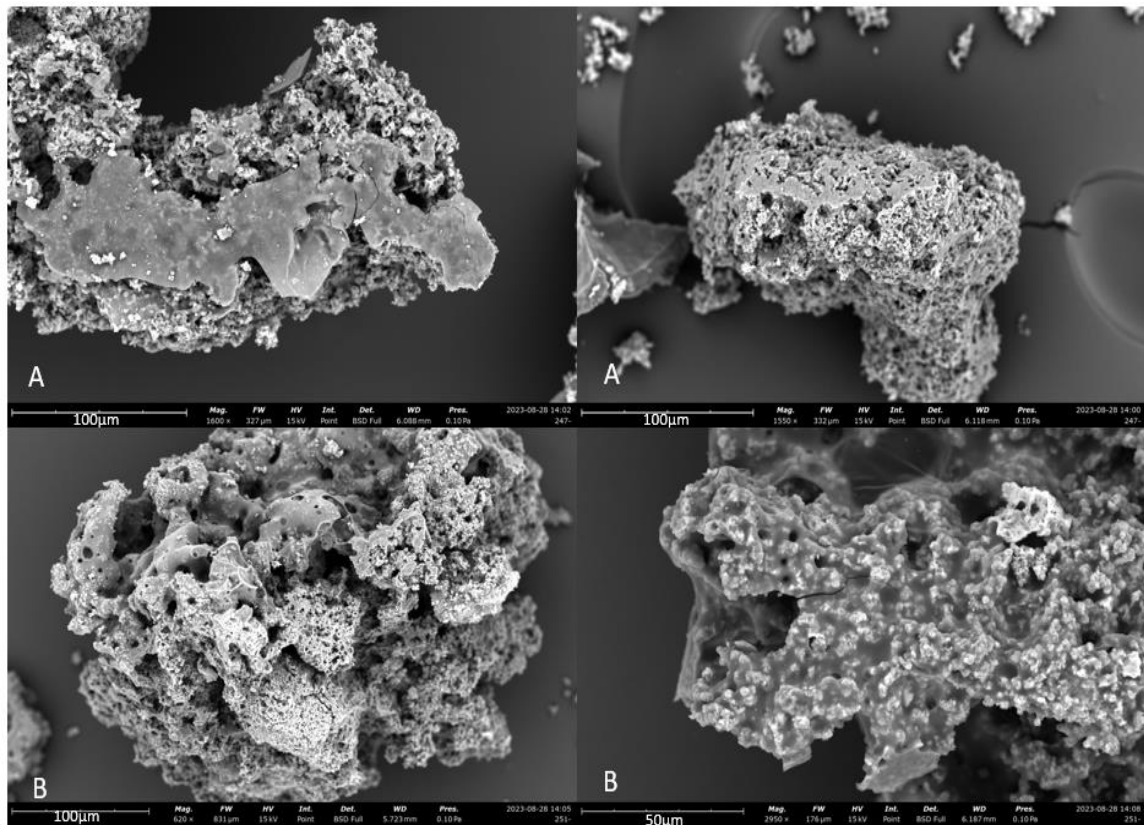


Figure 79. SEM images and EDS results of residual chars from A: 5-MTB@HAp-MF 1:1-PU and B: 5-MTB@HAp-MF 1:3-PU samples.

Figure 78 displays images of residual chars from MTB@HAp-MF-PU composites. Upon the addition of MF encapsulated MTB@HAp, a minor quantity of char is

formed as tin film on aluminum foil and accumulated along the periphery of the aluminum foil, as depicted in Figure 78. Accordingly, the protective function of the char structure is not good. But there was a notable decrease in PHRR and THE values observed in the MTB@HAp-MF-PU samples. The decrease in these values indicates that the additive acts in the gas phase by diluting the fuel and inhibiting the flame.



Figure 80. Images of residual chars from PU composites; A:5%MTB-MF 1:1-PU, B:5%MTB-MF 1:3-PU.

In the gas phase, decomposition of MF produces noncombustible nitrogen oxide, ammonia, carbon dioxide that are able to trap radicals in gas phase [50]. SEM images of char residues of MTB@HAp-MF samples are shown in Figure 79. The residual

char at periphery of aluminum foil was analyzed for SEM imaging. EDS analysis demonstrated that the core shell structure of MTB@HAp-MF particles was preserved while the morphology of microcapsules was distorted during burning.

Figure 80 illustrates the photographs of the MTB-MF-PU composite residues at the end of MLC tests. It is evident that there is a thin layer char left after the MLC test for the composite. Increasing the MF ratio from 1:1 to 1:3 in the MTB-MF-PU composite did not affect the formation of additional char. The formation of char after the MLC test looks the same as that of the MTB@HAp-MF-PU samples. However, the addition of MTB-MF samples reduced the peak heat release rate (PHRR) and total heat evolved (THE) values compared to those of MTB-HAp-MF-PU composites. The amount of encapsulated MF on MTB is higher compared to the amount on the surface of MTB@HA, which is detected in TGA analyses (Figure 44 and Figure 46). It demonstrates that the ratio of MF microencapsulation to MTB-MF-PU at 1:3 promotes the creation of gases that dilute the flame.

The surface and sectional microstructures of the char residue in MTB-MF-PU composites were analyzed using SEM and EDS shown in Figure 81. SEM image of MTB-MF 1:1-PU composite shows nonuniform structures containing carbon, nitrogen, oxygen, and boron elements. The residual char has pores on the surface, which proves noncombustible gas formation from MF during flame process. In this case, there are no wide cracks on the surface for MTB-MF 1:3, microcapsule morphology was distorted due to decomposition of MF. It is important to acknowledge that by increasing the MF content, the resulting char is more tightly packed and has a more fibrous texture [117]. Hence, MTB-MF migrated to the surface and formed highly effective barrier between condensed and gas phases [50].

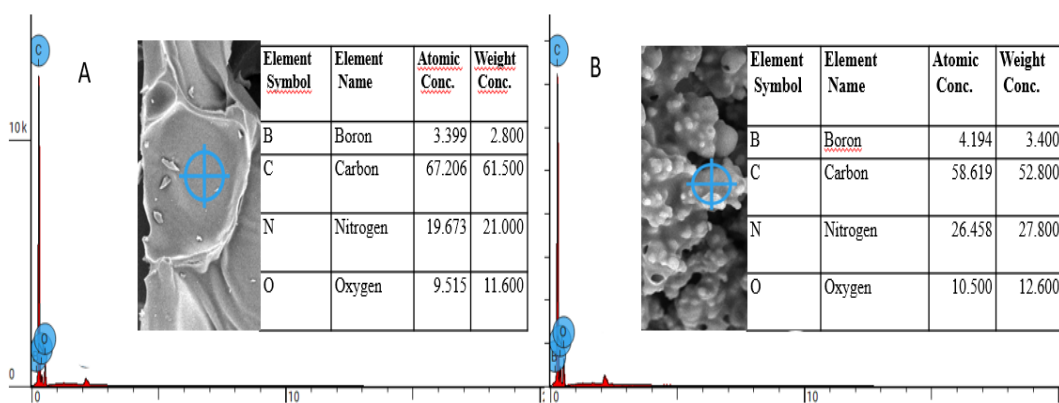
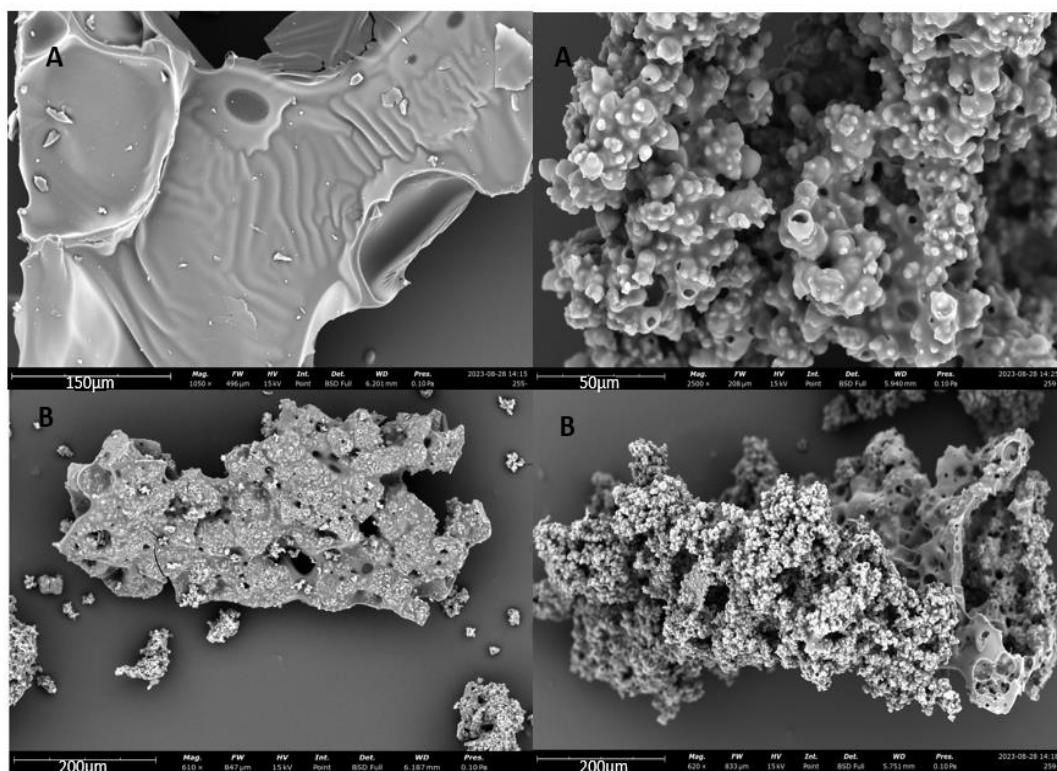


Figure 81. SEM images and EDS results of residual chars from A: 5-MTB-MF 1:1-PU and B: 5-MTB-MF 1:3-PU samples.

4.2.3.2 XRD Analysis of Residual Chars from Mass Loss Calorimeter

XRD was used to analyze the residual char composition after mass loss calorimetry tests. XRD patterns of char residues of MTB-PU and MTB@HAp-PU composites are shown in Figure 82 and Figure 83. The diffraction peaks from the residual chars of MTB-PU composites came from MgB_4O_7 . The peak intensities of MgB_4O_7 increase as the ratio of MgB_4O_7 in PU increases, indicating that most of the added MgB_4O_7 remains unchanged in crystal structure after burning.

In addition, the diffraction peaks from the residual char of MTB@HAp-PU corresponded to hydroxyapatite. In the same way, the peak intensities of MgB_4O_7 @HAp increase as the ratio of MgB_4O_7 @HAp in PU increases. After MLC test, MTB@HAp structure is preserved and most of the char is formed from MTB@HAp and carbon residues, which is endorsed by EDS analysis given in Figure 79.

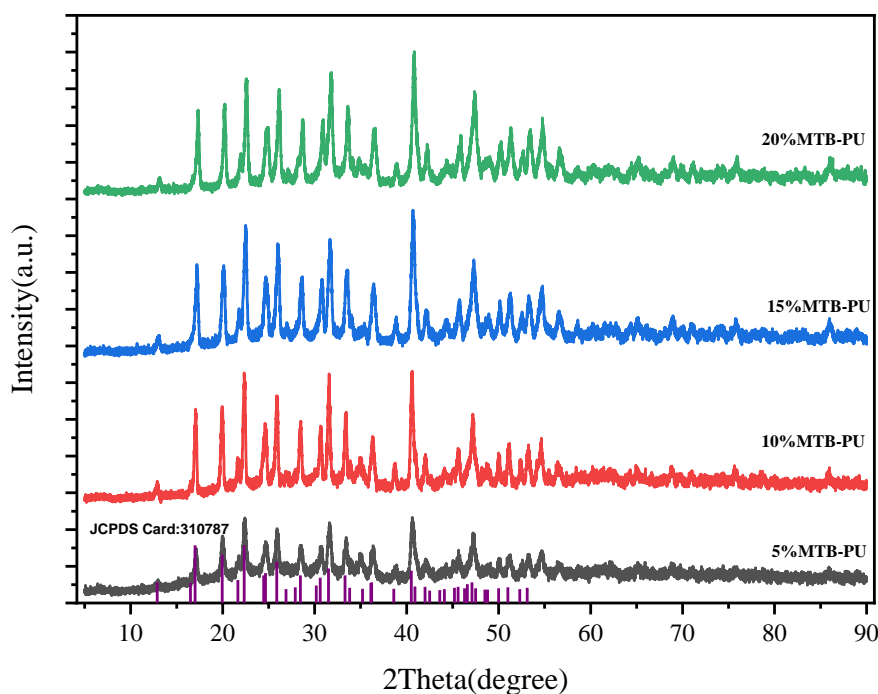


Figure 82. XRD patterns of residual chars from the PU samples.

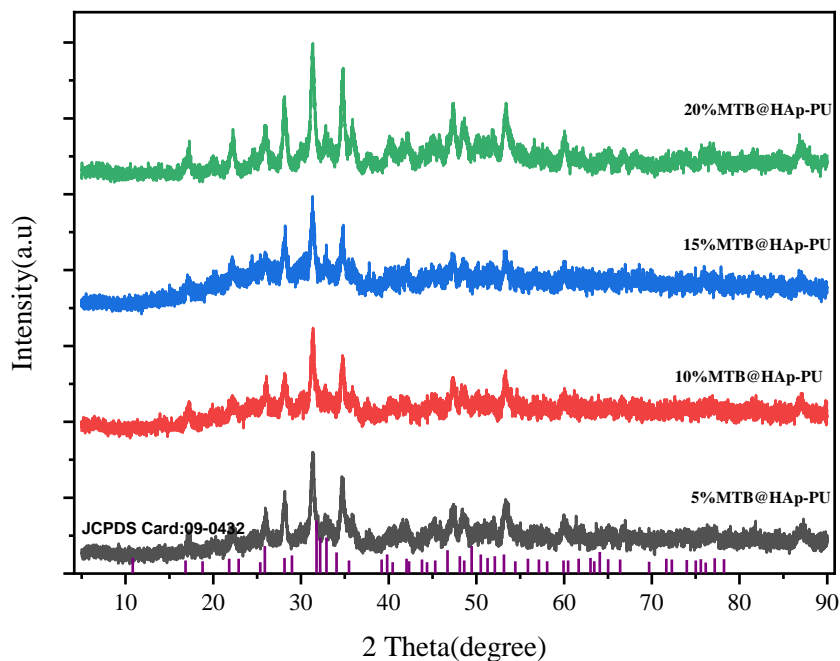


Figure 83. XRD patterns of residual chars from the PU samples.

X-ray diffraction patterns of microencapsulated MTB and MTB@HAp, as well as char residues of PU composites, displayed in Figure 84 and Figure 85. After MLC analyses, XRD patterns belong to MTB-MF microcapsules. XRD patterns of char residues of MTB-MF microcapsules became more amorphous due to containing carbon residues after burning (Figure 84).

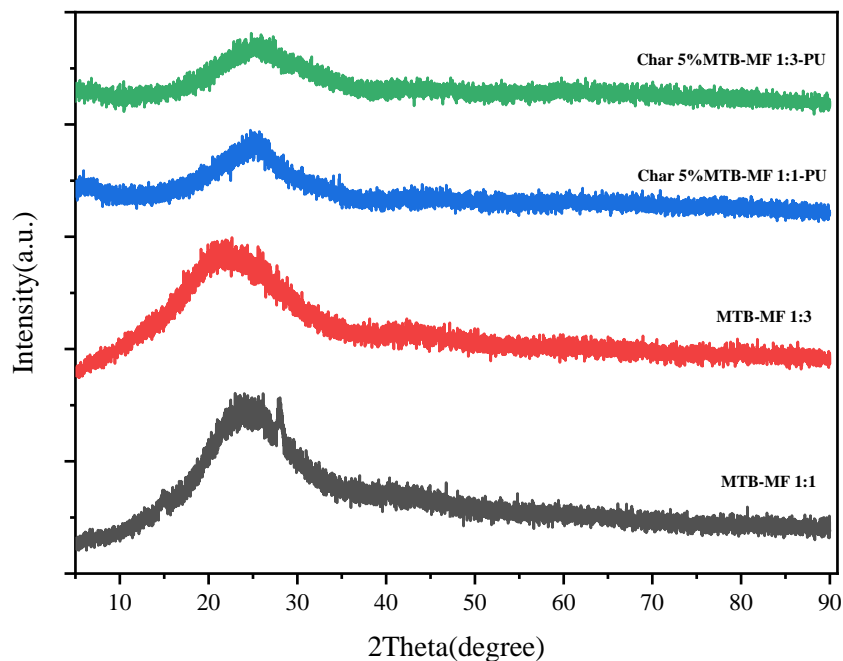


Figure 84. XRD patterns of residual chars from the PU samples.

Figure 85 shows XRD patterns of MTB@HAp-MF-PU samples after conic calorimeter tests. XRD shows that char residues made of MTB@HAp-MF and carbon remaining, which is supported by EDS analysis. However, decomposition of MF microcapsules on MTB@HAp is observed by XRD patterns of MTB@HAp-MF(1:1 and 1:3) samples after CC tests. The MF layer is partially lost after burning. It may be seen that XRD patterns of char residues of MTB@HAp-MF-PU have the diffractions coming from Calcium Phosphate (whitelockite) that dissociates from HAp at 27, 31 ve 34° [91].

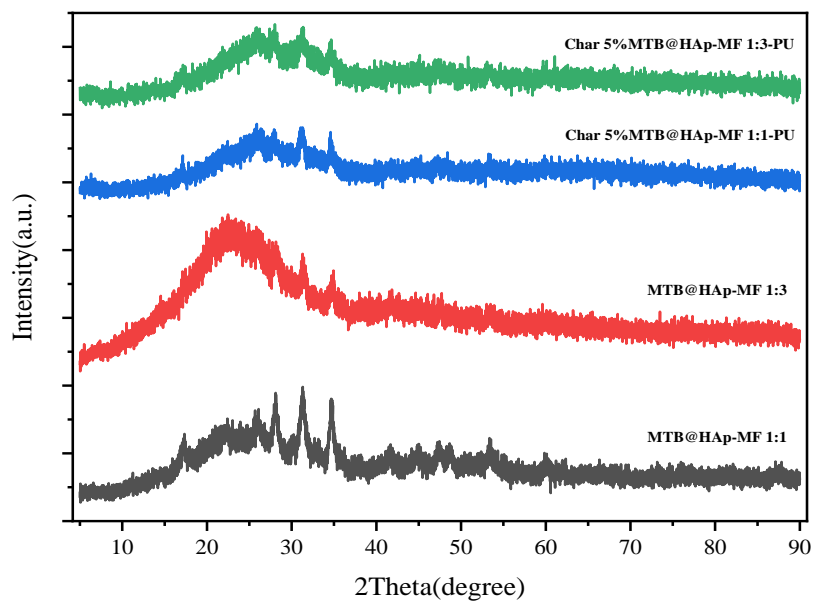


Figure 85. XRD patterns of residual chars from the PU samples.

4.2.3.3 FTIR Analysis of Residual Chars from Mass Loss Calorimeter

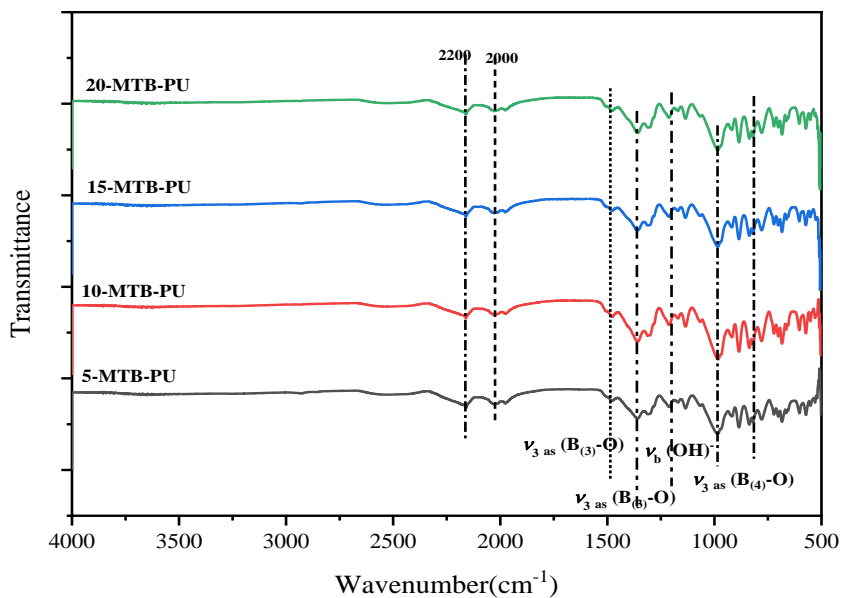


Figure 86. FTIR spectra of residual chars from the PU samples.

Figure 86 and Figure 87 show the FTIR of MTB-PU and MTB@HAp-PU composites, and their residual chars after MLC tests. The FTIR analysis revealed that the residual char contains the MTB structure, which remained intact after the burning process. Characteristic vibration bands of B-O bond in BO_3 and BO_4 are observed in FTIR spectrum of MTB-PU composites. In addition, the peaks at 2000-23000 cm^{-1} stem from Isocyanate (-NCO) due to uncomplete decomposition of polyurethane [64][118]. For MTB@HAp-PU composites, many infrared absorption peaks are found from residual char of MTB@HAp-PU. Therefore, the results suggest that MTB@HAp had retained effective structures even after decomposition of PU composites. Similarly, in MTB-PU composites, the peaks at 2000-23000 cm^{-1} were observed due to incomplete decomposition of PU.

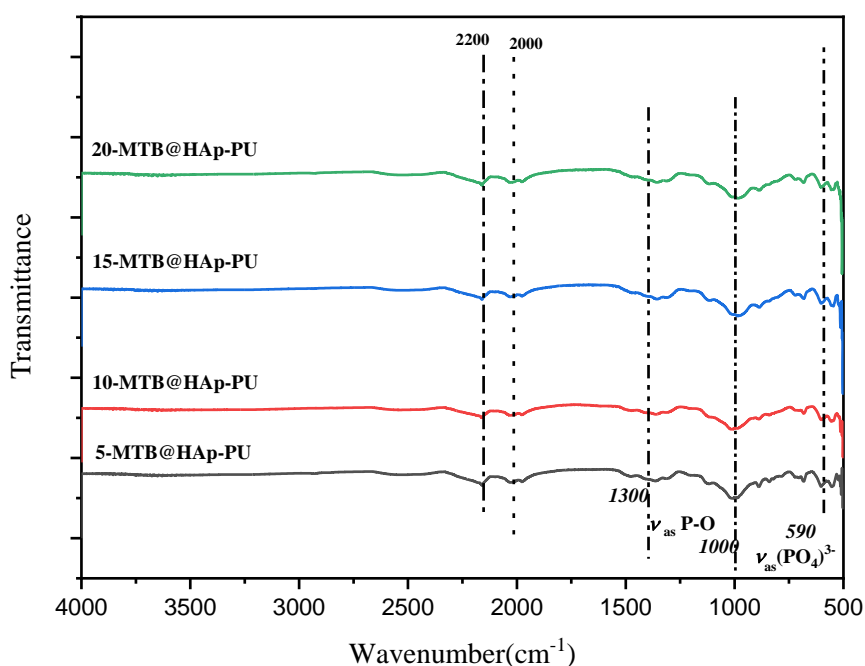


Figure 87. FTIR spectra of residual chars from the PU samples.

Figure 88 and Figure 89 show that FTIR spectra of MF microencapsulated MTB-PU and MTB@HAp-PU composites after MLC analysis. The bands which correspond

to melamine formaldehyde resin peaks disappeared after the burning process. Nevertheless, the peaks at 2000-23000 cm^{-1} arise from isocyanate (-NCO) due to incomplete decomposition of polyurethane. SEM images presented in Figure 78 and Figure 80 endorse evidence of MF microcapsule structure distortion that occurs on both MTB and MTB@HAp following CC analysis. Hence, decomposition of MF structure favored the releasing of noncombustible gases which made the dilution effect in the gas phase.

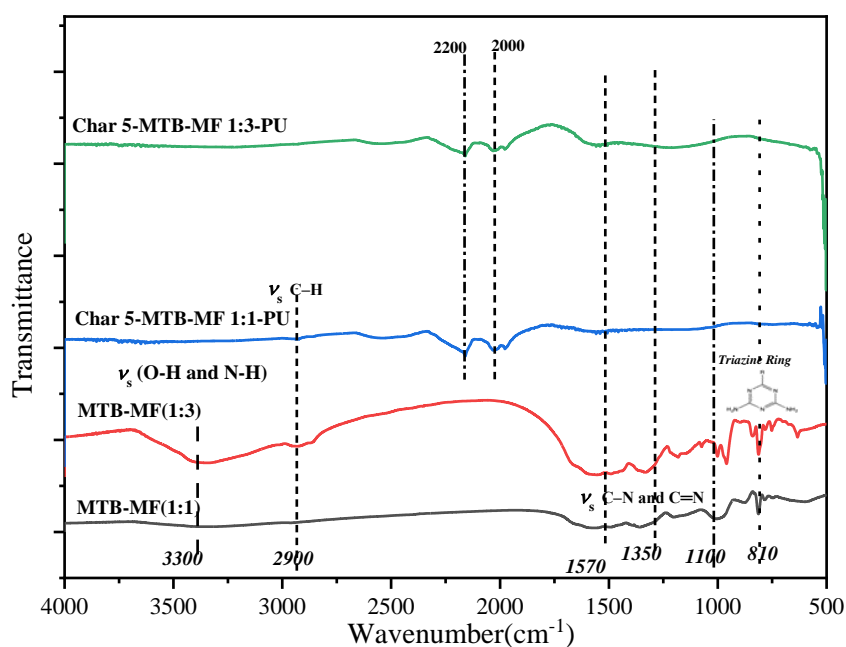


Figure 88. FTIR spectra of residual chars from the PU samples.

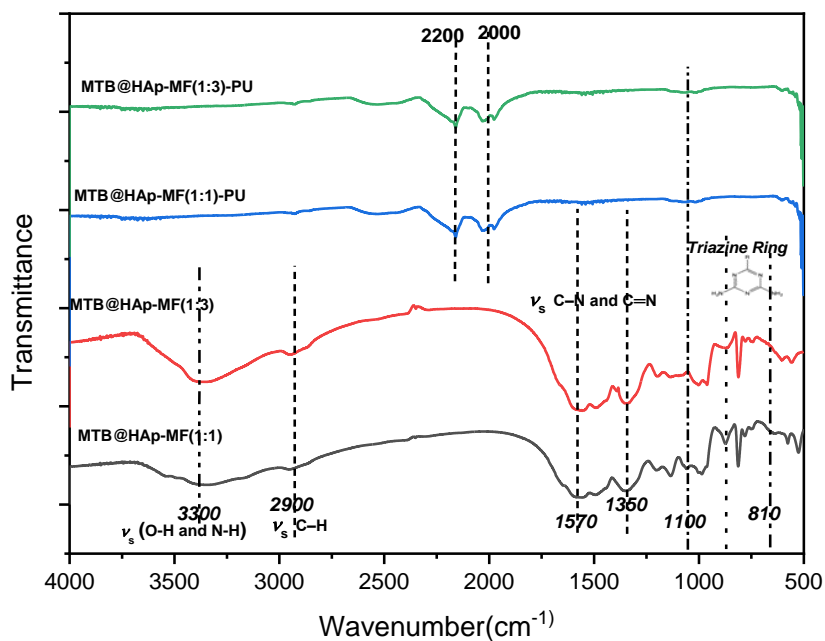


Figure 89. FTIR spectra of residual chars from the PU samples.

4.3 Flame Retardant Mechanisms of PU Composites.

4.3.1 Non-Oxidative Thermal Degradation Mechanism of Neat PU

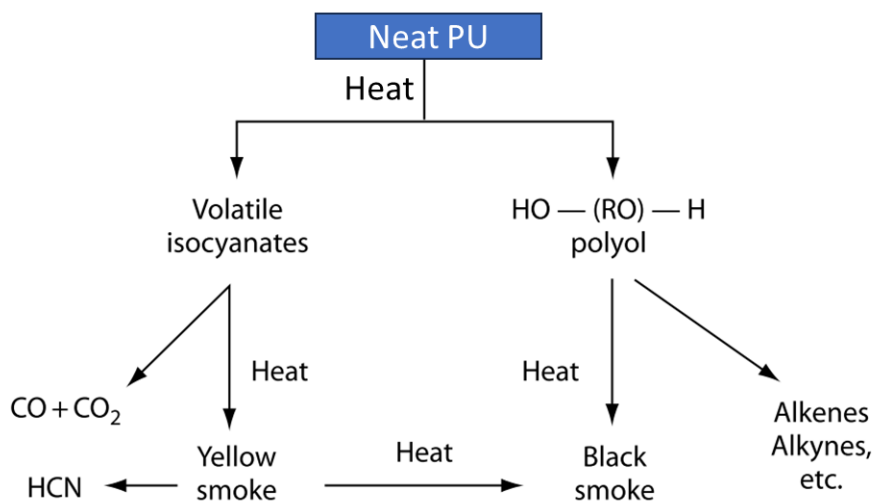


Figure 90. Thermal degradation steps of PU[76].

The neat PU's TGA results indicated a two-step degradation mechanism described in Figure 90, but no information was provided on the specific mechanisms. However, the TGA-FTIR results (as seen in Figure 59) showed that the initial degradation step is linked to the degradation of urethane linkages through two competing mechanisms. The primary mechanism proposed involves the straightforward depolymerization of the urethane bond, resulting in the production of TDI and polyol. However, a competing mechanism is also suggested, which involves the dissociation of the urethane linkages. This mechanism yields diamino toluene (DAT), carbon dioxide, and alkene-terminated polyol chains [74, 24, 113, 108].

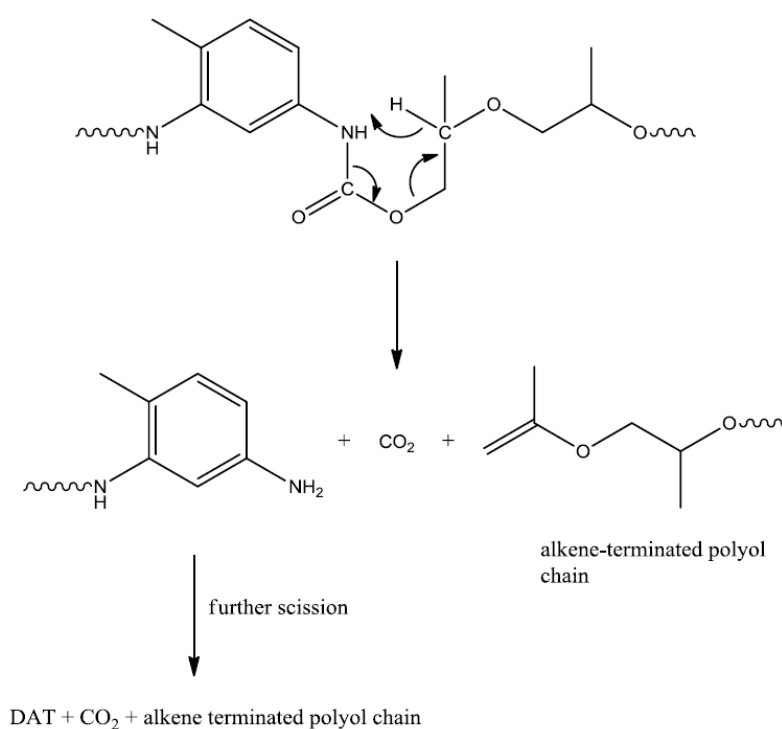


Figure 91. Primary degradation steps of urethane linkage [24].

Upon conducting TGA-FTIR analysis on neat PU, it was noted that peaks appeared at 1634 cm⁻¹, signifying carbonyl stretching, and 1544 cm⁻¹, signifying N-H stretching. The confirmation of carbon dioxide presence further validates the degradation of the urethane linkage, taking place through both depolymerization

reaction that yields TDI and polyol, as well as dissociation reaction that yields DAT, carbon dioxide, and an alkene-terminated polyol chain, as shown in Figure 91.

The secondary degradation stage can be attributed to further degradation reactions, specifically the degradation of the polyol or alkene-terminated polyol chain that was regenerated during the primary degradation processes [24]. TGA-FTIR analysis has identified several major condensable degradation products that form at different temperatures, including carbon dioxide, formaldehyde, and acetaldehyde. These products are all derived from the polyol component of the PU, apart from carbon dioxide, which is produced during the initial degradation stage as previously discussed. It is suggested that the degradation of the polyol occurs through the random scission of C-C and C-O bonds in the polymer backbone, resulting in the formation of the major condensable products.

4.3.2 Proposed Flame Retardant Mechanism of MTB and MTB@HAp

Borates are a class of inorganic additives that have been shown to enhance the performance of polymeric materials during combustion. MTB and MTB@HAp are two types of borates that operate through a physical flame-retardant mechanism in the condensed phase, as opposed to a chemical one. This mechanism forms an inorganic layer on the surface of the polymer, which acts as a protective shield and prevents the development of carbonaceous char [119, 72].

The MTB particles exhibit bulk low density and increased polymer melt viscosity, which significantly alters the thermal conductivity of the material. Consequently, they tend to accumulate near the regressing polymer surface without sinking, thereby forming a barrier that enhances the fire performance of the material compared to the neat matrix. This improvement is achieved by uniformly dispersing the MTB particles in PU. The formation of a protective impermeable coating can effectively reduce the amount of heat transferred to the polymer and hinder the diffusion of oxygen in the area of decomposition [119, 120]. Additionally, it acts as a barrier to

prevent the escape of volatile flammable gases that generate during polymer decomposition [121]. The dispersion of MTB in PU matrix can significantly reduce dripping, even though UL94 rating is still V-2 (in Figure 65). However, upon loading MTB up to 10 PHR, the LOI rating improved from 22% to 25%. This is attributed to the formation of a protective fire residue layer resulting from the well-dispersed MTB particles that alter the melt viscosity. The SEM image confirms the formation of a thin layer of carbonaceous or vitreous material on the polymer surface. (Figure 74). It has been observed that the introduction of 15 or 20 PHR to polyurethane (PU) results in worsen dispersion quality within the PU matrix. This phenomenon is further compounded by the tendency of MTB particles to sink through the PU melt during combustion. Furthermore, it is important to note that the primary contribution of MTB to the flame retardancy of PU is a decrease in the peak heat release rate (pHRR), as demonstrated in Table 22. The results indicate that the addition of MTB led to a reduction in THE, up to 10 PHR. This finding provides support for the proposed mechanism, which is believed to occur in the condensed phase.

Similarly, MTB@HAp is effective in the condensed phase through a physical flame-retardant mechanism, rather than a chemical one. However, after coating MTB with HAp, its flame retardancy performance decreased. This decrease in performance can be attributed to the increase in particle size of MTB@HAp after coating. Consequently, the bulk density of MTB@HAp increased compared to MTB, and the larger particle size also altered the mechanical, mixing, and thermal properties of the material. It has been demonstrated that the homogeneity of the PU matrix can be impaired, resulting in reduced dispersion quality and interactions between the polymer and filler. This, in turn, leads to a decline in thermal and physical properties. During combustion, the high density and low surface area of the filler causes it to sink through the polymer melt, without accumulating near the surface [120, 34]. As such, it is unable to construct a superficial layer and is less effective than MTB in reducing polymer flammability. The reduction in melt viscosity facilitates the flow of molten polymer away from the fire zone, thereby preventing the fuel that sustains the flame. The LOI value for 15 PHR MTB@HAp-PU has been observed to increase

to 26.5%, which is higher in comparison to 10 PHR-MTB-PU. pHRR and THE values in Table 22 support the lower flame retardancy character of MTB@HAp-PU.

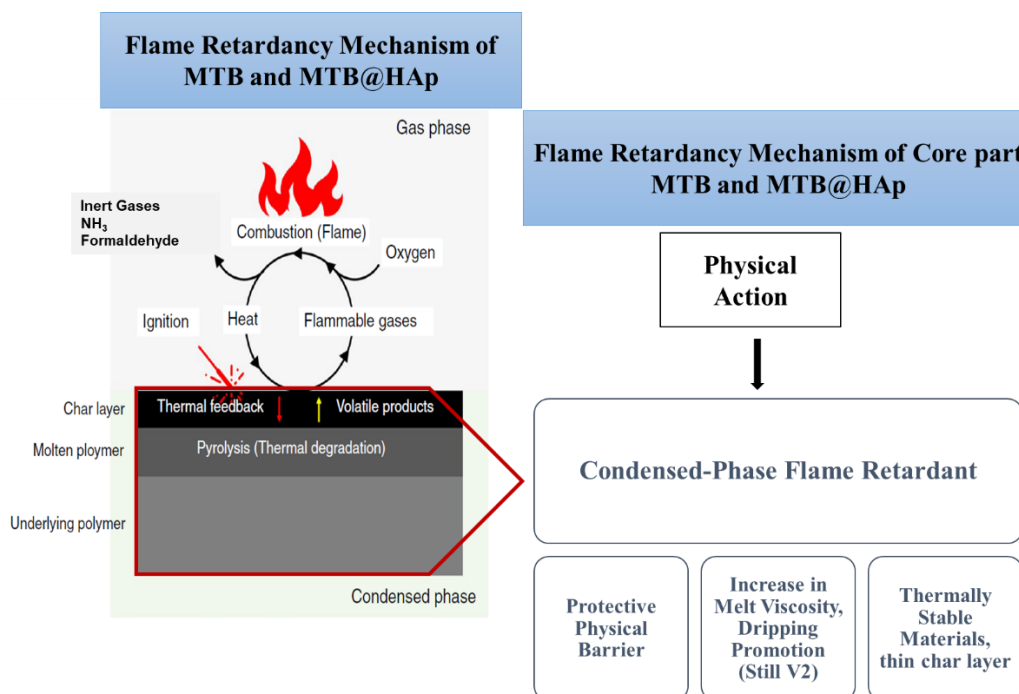


Figure 92. Proposed Flame retardancy mechanism of MTB and MTB@HAp in condensed Phase.

4.3.3 Proposed Flame Retardancy Mechanism of MF encapsulated MTB and MTB@HAp-PU

The flammability properties of the PU composites containing MTB and MTB@HAp are comparable. However, they do not meet the UL-94 V-0 rating with reasonable pHRR and THE. Therefore, there is a need to incorporate additional flame retardants in order to achieve synergy with MTB or MTB@HAp. These flame retardants should operate by inhibiting the oxidation reactions that occur in the gas phase, either by trapping free-radical species or by diluting the flame with inert gases [122, 79].

Melamine-Formaldehyde (MF) encapsulated MTB and MTB@HAp can operate effectively in both condensed and gas phase. In the vapor phase, these encapsulated materials act as multifunctional flame retardants, as they contain both gas phase

active FR (MF) and condensed phase active FR (MTB or MTB@HAp as core). The operating mechanism of MF encapsulated MTB and MTB@HAp is based on the properties of melamine formaldehyde resin, which is a type of nitrogen-containing flame retardant (NFR). Melamine Formaldehyde (MF) is a commonly used flame retardant that operates by initially endothermically dissociating into formaldehyde and melamine. This dissociation is followed by the sublimation of the resultant melamine, which subsequently degrades and releases non-flammable gases like nitrogen and ammonia [97]. These gases absorb heat and cool down the substrate, making it an effective vapor-phase flame retardant [119]. The inert gases produced also dilute the levels of oxygen and flammable gases, further contributing to the retardancy of the flame [77]. Based on the TGA-FTIR analysis presented Figure 48, the flame retardant properties of MF can be attributed to the sublimation (melting with vaporization) of melamine at around 350 °C. This process absorbs a considerable amount of heat, which results in the reduction of the temperature of the polymer's surface that is exposed to fire, thereby preventing degradation. At elevated temperatures, melamine undergoes thermal decomposition and liberates ammonia gas, which diffuses into the surrounding atmosphere and dilutes both oxygen and combustible gases. This process leads to the formation of highly stable compounds known as melem (2,5,8-triamino-1,3,4,6,7,9,9b-heptaazaphenalene), melam ((N-4,6-diamino-1,3,5-triazin-2-yl)-1,3,5-triazine-2,4,6-triamine), and melon (Poly(8-amino-1,3,4,6,7,9,9b-heptaazaphenalene-2,5-diyl)), which serve to increase the melt viscosity and allow for achieving V0 rating for 5-MTB-MF-PU, with a 27% LOI index [119, 77].

Moreover, the heat release rates (pHRR) of the melamine-formaldehyde (1:3) treated 5-MTB-PU and 5-MTB@HAp-PU were successfully reduced by 5 and 3 factors, respectively, which also resulted in a decrease in the total heat evolved (THE) by 8 and 3 factors. This phenomenon can be attributed to the proposed mechanism, wherein the amino group of melamine attacks the isocyanate to form a non-volatile compound (as depicted in Figure 93), which fails to enter the gas phase and fuel the flame. The reduced fuel leads to a lower heat release rate. This suggests that MF's

effectiveness is not solely due to endothermic decomposition and dilution of combustible gases by inert gases, as was previously assumed [77].

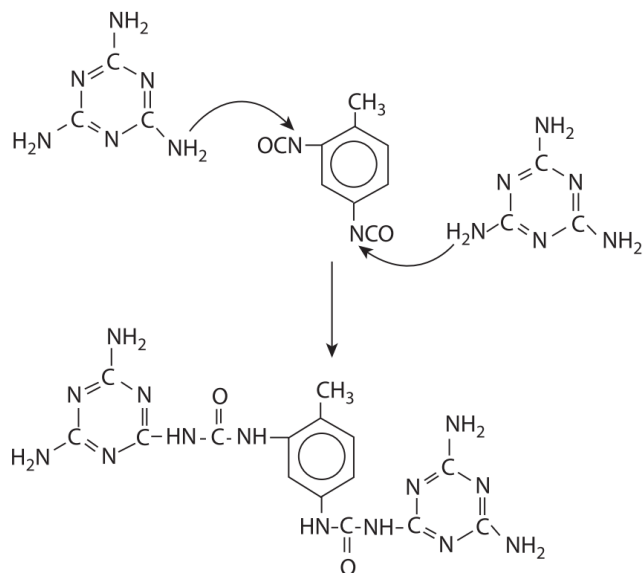


Figure 93. Proposed reaction of amine group and Isocyanide in TDI [77].

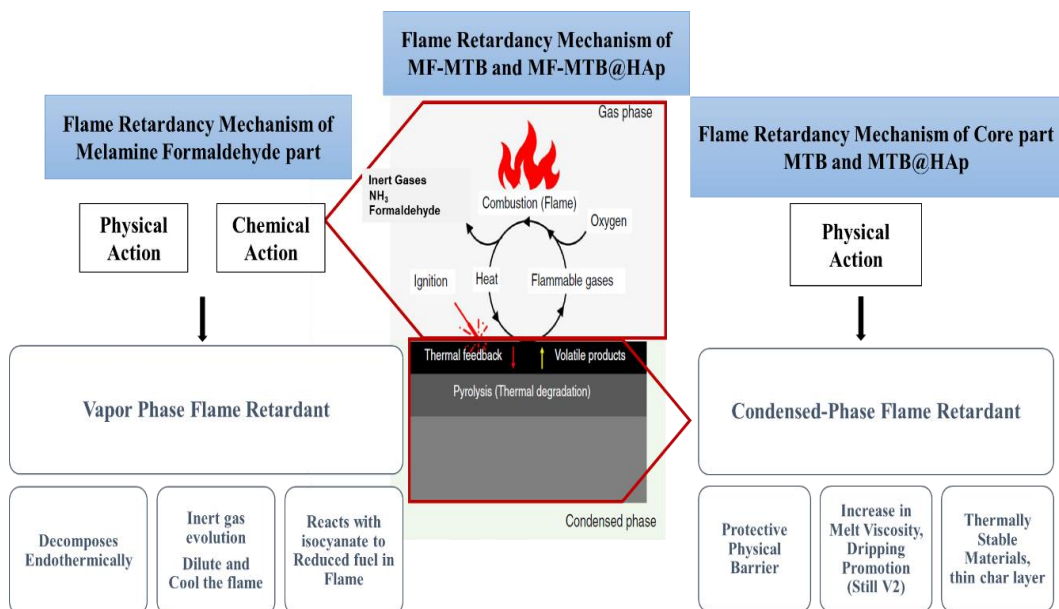


Figure 94. Proposed Flame retardancy mechanisms of MF-MTB and MF-MTB@HAp in condensed and gas phases.

CHAPTER 5

CONCLUSION

This study focuses on developing a new multifunctional flame-retardant system, which uses magnesium tetraborate to enhance the flame resistance of polyurethane. The study has three main parts: the synthesis and characterization of flame-retardant materials, including magnesium tetraborate, hydroxyapatite coated magnesium tetraborate, and melamine formaldehyde encapsulated forms of minerals. The second part involves the synthesis and characterization of polyurethane composite samples, followed by the characterization of the flame retardancy of PU composites.

In the first part of this study, four different boron-containing materials such as Magnesium Tetraborate (MTB), Magnesium Tetraborate-Hydroxyapatite Core/Shell (MTB@HAp), and Melamine Formaldehyde (MF) resin-encapsulated MTB and MF encapsulated MTB@HAp, were used to improve the flame retardancy of Polyurethane (PU). MTB was synthesized using the solid-state (SS) synthesis method. With a shell of HAp, coated MTB is prepared using the wet precipitation method. To enhance the flame retardancy performance of MTB, a combination of boron-based and nitrogen-based compounds, such as MF, can provide synergy. The novel MF microcapsulated MTB-MF and MF encapsulated MTB@HAp with a double shell were prepared by in situ polymerization. XRD and FTIR results prove that the flame retardants were synthesized successfully. Thermal analysis shows that MTB and MTB@HAp samples are stable till 900 °C. According to TGA coupled FTIR gas analysis, MF encapsulated samples release inert gases such as NH₃ and formaldehyde at 300 °C due to decomposition of melamine formaldehyde. At temperatures beyond 331°C, a polycondensation reaction was ensured, leading to the formation of diverse products through independent reactions involving both side chain and ring degradation of triazine ring of melamine.

In the second part of this study, polyurethane composites containing MTB, MTB@HAp, MTB-MF, and MTB@HAp-MF with varying amounts were produced by isocyanate and polyol reaction at 70 °C for 24h. PU composites undergo thermal and flammability tests.

Finally, 10 PHR-MTB and 15 PHR-MTB@HAp core shell containing PU composites achieved 25% and 26.5% LOI values with V-2 of UL-94 rating, respectively. Besides, the peak Heat Release Rate (PHRR) of 10 PHR-MTB and 15 PHR-MTB@HAp containing PU composites were reduced by 28% and 20% with respect to the PHRR of neat PU. 5 PHR-MTB-MF (the mass ratio of MTB: MF-1:3) achieved the maximal LOI value of 27%, V-0 of UL-94 rating, and significantly decreased the peak heat release rate from 350 kW/m² to 70 kW/m² with respect to neat PU. In the same way, 5 PHR MF encapsulated MTB@HAp containing PU showed enhanced flame retardancy. Yet, UL-94 rating was measured V-2 and pHRR of the composite remained higher than MF encapsulated MTB-PU composites. MTB-MF and MTB@HAp exhibit improved flame retardance as a result of the synergistic flame-retardant effect of the core coordination with MF. TGA-FTIR results demonstrate that the exceptional flame cooling effects of MTB-MF and MTB@HAp-MF are linked to the discharge of inert gases, such as NH₃, into the flame. After examining the volatile gases and residues, it is evident that the flame retardance of MTB-MF and MTB@HAp-MF in PU materials is achieved through both gas-phase and condensed-phase mechanisms. This is accomplished by utilizing a combination of varied additives within a single flame retardant. Microencapsulated MTB offers a significant advantage in its effectiveness even at low concentrations with excellent mixing homogeneity. The results obtained demonstrate MTB-MF(1:3) microcapsule prepared with efficiency exhibit remarkable flame retardancy, making them a promising multifunctional composite for usage as a flame retardant in polyurethane applications.

REFERENCES

- [1] E. N. Doyle, *The Development and Use of Polyurethane Products*. New York: McGraw-Hill, **1971**. doi: 10.1016/B978-1-4557-3149-7.00002-4.
- [2] M. A. Garrido and R. Font, “Pyrolysis and combustion study of flexible polyurethane foam,” *J. Anal. Appl. Pyrolysis*, vol. 113, pp. 202–215, **2015**, doi: 10.1016/j.jaap.2014.12.017.
- [3] D. Ahirwar, A. Telang, R. Purohit, and A. Namdev, “Materials Today : Proceedings A short review on polyurethane polymer composite,” *Mater. Today Proc.*, vol. 62, pp. 3804–3810, **2022**, doi: 10.1016/j.matpr.2022.04.481.
- [4] J. C. Quagliano Amado, “Thermal Resistance Properties of Polyurethanes and its Composites: A Short Review,” *J. Res. Updat. Polym. Sci.*, vol. 8, pp. 66–84, **2019**, doi: 10.6000/1929-5995.2019.08.10.
- [5] D. K. Chattopadhyay and D. C. Webster, “Thermal stability and flame retardancy of polyurethanes,” *Prog. Polym. Sci.*, vol. 34, pp. 1068–1133, **2009**, doi: 10.1016/j.progpolymsci.2009.06.002.
- [6] H. Zhang, Y. Chen, Y. Zhang, “Synthesis and Characterization of Polyurethane Elastomers,” *J. Elastomers Plast.*, vol. 40, no. April 2008, pp. 161–177, 2008, doi: 10.1177/0095244307085540.
- [7] N. F. Zaaba, H. Ismail, and A. M. Saeed, “A Review : Metal Filled Thermoset Composites A Review : Metal Filled Thermoset Composites,” *Polym. Technol. Mater.*, vol. 61, no. 1, pp. 13–26, **2022**, doi: 10.1080/25740881.2021.1948058.
- [8] K. Cherednichenko, D. Kopitsyn, E. Smirnov, N. Nikolaev, and R. Fakhrullin, “Fireproof Nanocomposite Polyurethane Foams : A Review,” *Polymers (Basel)*, vol. 15, no. 2314, **2023**.
- [9] T. Gupta and B. Adhikari, “Thermal degradation and stability of HTPB-based

- polyurethane and polyurethaneureas,” *Thermochim. Acta*, vol. 402, pp. 169–181, **2002**, doi: 10.1016/S0040-6031(02)00571-3.
- [10] M. Kirpluks, U. Cabulis, V. Zeltins, L. Stiebra, and A. Avots, “Rigid Polyurethane Foam Thermal Insulation Protected with Mineral Intumescent Mat,” *AUTEX Res. J.*, vol. 14, no. October 2015, pp. 259–270, **2014**, doi: 10.2478/aut-2014-0026.
- [11] C. Bruno, *The International Handbook of Space Technology*. Springer International Publishing, **2014**.
- [12] J. Carlos, Q. Amado, G. Ross, and M. Silva, “Properties of Hydroxyl-Terminal Polybutadiene (HTPB) and Its Use as a Liner and Binder for Composite Propellants : A Review of Recent Advances,” *Propellants, Explos. Pyrotech.*, no. April, **2022**, doi: 10.1002/prop.202100283.
- [13] O. Aslan, T. Atalar, G. Atınç Yılmaz, and N. Özkan, “Enhancing the performance of HTPB-IPDI-based polyurethane composite liner through effective carbon black dispersion,” *Propellants, Explos. Pyrotech.*, vol. 48, no. 12, pp. 1–14, **2023**, doi: 10.1002/prop.202300107.
- [14] E. K. Allcorn, M. Natali, and J. H. Koo, “Composites : Part A Ablation performance and characterization of thermoplastic polyurethane elastomer nanocomposites,” *Compos. PART A*, vol. 45, pp. 109–118, **2013**, doi: 10.1016/j.compositesa.2012.08.017.
- [15] D. C. Gupta, S. S. Deo, D. V. Wast, S. S. Raomre, and D. H. Gholap, “HTPB-Based Polyurethanes for Inhibition,” *J. Appl. Polym. Sci.*, vol. 55, pp. 1151–1155, **1995**.
- [16] M. Mosa, M. Kotb, H. Fouda, and M. Gobara, “Study of Elastomeric Heat Shielding Materials for Solid Rocket Motor Insulation Study of Elastomeric Heat Shielding Materials for Solid Rocket Motor Insulation,” **2022**. doi: 10.1088/1742-6596/2305/1/012037.

- [17] M. A. Daniel, "Polyurethane binder systems for polymer bonded explosives," **2006**. [Online]. Available: <http://nla.gov.au/nla.arc-52839>
- [18] J. Carlos, Q. Amado, P. G. Ross, and N. B. Sanches, "Evaluation of elastomeric heat shielding materials as insulators for solid propellant rocket motors : A short review," *Open Chem.*, pp. 1452–1467, **2020**.
- [19] V. Shahedifar, H. R. Tajik, and A. M. Rezaoust, "Studying the thermal properties of a cotton/epoxy composite inhibitor," *Propellants, Explos. Pyrotech.*, vol. 37, no. 5, pp. 569–574, **2012**, doi: 10.1002/prop.201100005.
- [20] M. S. D. Kakade, M. V Vaidya, D. G. Khangaonkar, P. K. Divekar, and U. B. Kadam, "Polyurethane-Based Inhibition for High Flame Temperature Nitramine-Based Composite Modified Double-Base Propellant," *Def. Sci. J.*, vol. 48, no. 4, pp. 371–377, **1998**.
- [21] W. H. Jolley, "studies on Coning in End-Burning Rocet Motors," *J. Propuls. Power*, vol. 2, no. 3, pp. 223–233, **1986**.
- [22] P. M. Visakh, A. O. Semkin, I. A. Rezaev, and A. V Fateev, "Review on soft polyurethane flame retardant," *Constr. Build. Mater.*, vol. 227, p. 116673, **2019**, doi: 10.1016/j.conbuildmat.2019.116673.
- [23] A. Hejna, "Clays as Inhibitors of Polyurethane Foams Flammability," *Materials (Basel)*, vol. 14, no. 4826, pp. 1–38, **2021**.
- [24] J. J. Allan, D. and Daly, J. and Liggat, "Thermal Volatilisation Analysis of TDI-based Flexible Polyurethane Foam," *Polym. Degrad. Stab.*, vol. 98, pp. 535–541, **2013**. doi: <http://dx.doi.org/10.1016/j.polymdegradstab.2012.12.002>.
- [25] A. Mosawi, *Flammability of composites*. Elsevier Ltd, **2016**. doi: 10.1016/B978-1-78242-325-6.00014-1.
- [26] W. Swan, " Halogenated Flame Retardants," pp. 22–28, **1996**.

- [27] A. Ubowska, “Montmorillonite as a Polyurethane Foams Flame Retardant,” *Arch. Combust.*, vol. 30, no. 4, pp. 459–462, **2010**.
- [28] X. L. Li *et al.*, “Influence of eco-friendly calcium gluconate on the intumescent flame-retardant epoxy resin: Flame retardancy, smoke suppression and mechanical properties,” *Compos. Part B Eng.*, vol. 176, no. June, p. 107200, **2019**, doi: 10.1016/j.compositesb.2019.107200.
- [29] S. M. Mostashari, Y. K. Nia, and F. Fayyaz, “Thermogravimetry of deposited caustic soda used as a flame-retardant for cotton fabric,” *J. Therm. Anal. Calorim.*, vol. 91, no. 1, pp. 237–241, **2008**, doi: 10.1007/s10973-006-8276-9.
- [30] S. Zhang and A. R. Horrocks, “A review of flame retardant polypropylene fibres,” *Prog. Polym. Sci.*, vol. 28, no. 11, pp. 1517–1538, **2003**, doi: 10.1016/j.progpolymsci.2003.09.001.
- [31] K. K. Shen, “Boron-based Flame Retardants in Non-Halogen-Based Polymers,” *Non-Halogenated Flame Retard. Handb.*, pp. 201–241, **2014**, doi: 10.1002/9781118939239.ch6.
- [32] L. Menachem, “Synergistic and Catalytic Effects in Flame Retardancy An Overview of Polymeric Materials,” *J. FIRE Sci.*, vol. 17, pp. 1797–1806, **1999**.
- [33] M. Zanetti, G. Camino, D. Canavese, A. B. Morgan, F. J. Lamelas, and C. A. Wilkie, “Fire retardant halogen-antimony-clay synergism in polypropylene layered silicate nanocomposites,” *Chem. Mater.*, vol. 14, no. 1, pp. 189–193, **2002**, doi: 10.1021/cm011124t.
- [34] K. K. Shen and E. Olson, “Borates as Fire Retardants in Halogen-Free Polymers,” in *In Fire and Polymers IV*, **2005**, pp. 224–236. doi: 10.1021/bk-2006-0922.ch018.
- [35] T. R. Hull, A. Witkowski, and L. Hollingbery, “Fire retardant action of

- mineral fillers,” *Polym. Degrad. Stab.*, vol. 96, no. 8, pp. 1462–1469, **2011**, doi: 10.1016/j.polymdegradstab.2011.05.006.
- [36] A. B. Morgan and D. Ph, “The Future of Flame Retardant Polymers – Unmet Needs and Likely New Approaches,” *Polym. Rev.*, vol. 59, no. 1, pp. 25–54, **2019**.
- [37] B. Xue, R. Qin, J. Wang, M. Niu, Y. Yang, and X. Liu, “Construction of carbon microspheres-based silane melamine phosphate hybrids for flame retardant poly(ethylene terephthalate),” *Polymers (Basel)*, vol. 11, no. 3, **2019**, doi: 10.3390/polym11030545.
- [38] M. Zhang, L. Wang, Y. Jia, and Z. Jiang, “N-Doped Graphene/Melamine Formaldehyde Composite Carbon Foam as a Binder-Free Electrode for Supercapacitors,” *J. Nanosci. Nanotechnol.*, vol. 19, no. 9, pp. 5825–5830, **2019**, doi: 10.1166/jnn.2019.16556.
- [39] S. H. Liu, C. F. Kuan, H. C. Kuan, M. Y. Shen, J. M. Yang, and C. L. Chiang, “Preparation and flame retardance of polyurethane composites containing microencapsulated melamine polyphosphate,” *Polymers (Basel)*, vol. 9, no. 9, **2017**, doi: 10.3390/polym9090407.
- [40] C. L. Chiang and J. M. Yang, *Flame retardance and thermal stability of polymer/graphene nanosheet oxide composites*. Elsevier Ltd, **2015**. doi: 10.1016/B978-0-08-100079-3.00010-7.
- [41] T. Guler, U. Tayfun, E. Bayramli, and M. Dogan, “Effect of expandable graphite on flame retardant, thermal and mechanical properties of thermoplastic polyurethane composites filled with huntite&hydromagnesite mineral,” *Thermochim. Acta*, vol. 647, pp. 70–80, **2017**, doi: 10.1016/j.tca.2016.12.001.
- [42] X. Yue, C. Li, Y. Ni, Y. Xu, and J. Wang, “Flame retardant nanocomposites based on 2D layered nanomaterials: a review,” *J. Mater. Sci.*, vol. 54, no. 20, pp. 13070–13105, **2019**, doi: 10.1007/s10853-019-03841-w.

- [43] Ü. Tayfun and M. Doğan, “Flame-retardant properties of fullerene and nanodiamond-based polymer nanocomposites,” in *Flame Retardant Nanocomposites: Emergent Nanoparticles and Their Applications*, **2023**, pp. 263–277.
- [44] S. Semenzato, “A novel phosphorus polyurethane foam/montmorillonite nanocomposite: Preparation, characterization and thermal behaviour,” *Appl. Clay Sci.*, vol. 44, no. 1–2, pp. 35–42, **2009**, doi: 10.1016/j.clay.2009.01.003.
- [45] S. Furtana, A. Mutlu, and M. Dogan, “Thermal stability and flame retardant properties of calcium- and magnesium-hypophosphite-finished cotton fabrics and the evaluation of interaction with clay and poss nanoparticles,” *J. Therm. Anal. Calorim.*, vol. 139, no. 6, pp. 3415–3425, **2020**, doi: 10.1007/s10973-019-08751-2.
- [46] Z. Li, B. Shao, Y. Huang, X. Li, and Z. Zhang, “Effect of Core – Shell Zinc Hydroxystannate Nanoparticle – Organic Macromolecule Composite Flame Retardant Prepared by Masterbatch Method on Flame-Retardant Behavior and Mechanical Properties of Flexible Poly (vinyl chloride),” *Polym. Eng. Sci.*, vol. 54, pp. 15–19, **2014**.
- [47] M. Dogan and S. Murat Unlu, “Flame retardant effect of boron compounds on red phosphorus containing epoxy resins,” *Polym. Degrad. Stab.*, vol. 99, no. 1, pp. 12–17, **2014**, doi: 10.1016/j.polymdegradstab.2013.12.017.
- [48] K. K. Shen, *Chapter 11 - Review of Recent Advances on the Use of Boron-based Flame Retardants*. Elsevier B.V., **2014**. doi: 10.1016/B978-0-444-53808-6.00011-1.
- [49] S. M. Unlu, S. D. Dogan, and M. Dogan, “Comparative study of boron compounds and aluminum trihydroxide as flame retardant additives in epoxy resin,” *Polym. Adv. Technol.*, vol. 25, no. 8, pp. 769–776, **2014**, doi: 10.1002/pat.3274.
- [50] M. Dogan, S. D. Dogan, L. A. Savas, G. Ozcelik, and U. Tayfun, “Flame

- retardant effect of boron compounds in polymeric materials rew,” *Compos. Part B Eng.*, vol. 222, no. June, p. 109088, **2021**, doi: 10.1016/j.compositesb.2021.109088.
- [51] K. K. Shen, *Review of Recent Advances on the Use of Boron-based Flame Retardants*. Elsevier B.V., **2014**. doi:10.1016/B978-0-444-53808-6.00011-1.
- [52] S. M. Unlu, U. Tayfun, B. Yildirim, and M. Dogan, “Effect of boron compounds on fire protection properties of epoxy based intumescent coating,” **2016**, pp. 17–28, 2017, doi: 10.1002/fam.2360.
- [53] K. Shen, Kocfahani, and F. Jouffet, “Zinc borates as multifunctional polymer additives,” *Polym. Adv. Technol.*, vol. 19, pp. 469–474, **2008**.
- [54] R. E. Myers, E. D. Dickens, E. Licursi, and R. E. Evans, “Ammonium pentaborate: An intumescent flame retardant for thermoplastic polyurethanes,” *Journal of Fire Sciences*, vol. 3, no. 6. pp. 432–449, **1985**. doi: 10.1177/073490418500300604.
- [55] J. Green, *Mechanisms for flame retardancy and smoke suppression - A review*, vol. 14, no. 6. **1996**. doi: 10.1177/073490419601400602.
- [56] T. Ishii, H. Kokaku, A. Nagai, T. Nishita, and M. Kakimoto, “Calcium Borate Flame Retardation System for Epoxy Molding Compounds,” *Polym. Eng. Sci.*, pp. 799–806, **2006**.
- [57] N. A. Isitman, M. Dogan, E. Bayramli, and C. Kaynak, “Fire Retardant Properties of Intumescent Polypropylene Composites Filled With Calcium Carbonate,” *Polym. Eng. Sci.*, pp. 875–883, **2011**, doi: 10.1002/pen.
- [58] F. Tugce Senberber Dumanli, “Magnesium Borates: The Relationship between the Characteristics, Properties, and Novel Technologies,” *Curr. Trends Magnes. Res.*, pp. 1–18, **2022**, doi: 10.5772/intechopen.104487.
- [59] J. Yongzhong, G. Shiyang, J. Yan, Z. Yuan, and X. Shuping, “FTIR spectroscopy of magnesium tetraborate solution,” *Chemical Papers*, vol. 55,

no. 3. pp. 162–166, **2001**.

- [60] T. M. Oliveira, A. F. Lima, M. G. Brik, S. O. Souza, and M. V. Lalic, “Electronic structure and optical properties of magnesium tetraborate: An ab initio study,” *Comput. Mater. Sci.*, vol. 124, pp. 1–7, **2016**, doi: 10.1016/j.commatsci.2016.07.007.
- [61] A. S. Dike, U. Tayfun, and M. Dogan, “Influence of zinc borate on flame retardant and thermal properties of polyurethane elastomer composites containing huntite-hydromagnesite mineral,” *Fire Mater.*, vol. 41, no. 7, pp. 890–897, **2017**, doi: 10.1002/fam.2428.
- [62] Z. Liu, “Molten-salt assisted synthesis and characterization of $Mg_2B_2O_5$ and $Al_{18}B_4O_{33}$ whiskers,” *J. Asian Ceram. Soc.*, vol. 9, no. 3, pp. 1298–1309, **2021**, doi: 10.1080/21870764.2021.1972591.
- [63] S. H. Chen, D. F. Zhang, and G. Sun, “In situ synthesis of porous ceramics with a framework structure of magnesium borate whiskers,” *Mater. Lett.*, vol. 121, pp. 206–208, **2014**, doi: 10.1016/j.matlet.2014.01.064.
- [64] G. Ozcelik, O. Elcin, S. Guney, A. Erdem, F. Hacioglu, and M. Dogan, “Flame-retardant features of various boron compounds in thermoplastic polyurethane and performance comparison with aluminum trihydroxide and magnesium hydroxide,” *Fire Mater.*, pp. 1–14, **2022**, doi: 10.1002/fam.3050.
- [65] X. Wang, Y. Shi, and Y. Liu, “Recycling of waste melamine formaldehyde foam as flame-retardant filler for polyurethane foam,” **2019**.
- [66] M. Baginska, N. R. Sottos, and S. R. White, “Core – Shell Microcapsules Containing Flame Retardant Tris(2- chloroethyl phosphate) for Lithium-Ion Battery Applications,” pp. 3–7, **2018**, doi: 10.1021/acsomega.7b01950.
- [67] F. Salau and I. Vroman, “Polymer Influence of core materials on thermal properties of melamine – formaldehyde microcapsules,” vol. 44, pp. 849–860, **2008**, doi: 10.1016/j.eurpolymj.2007.11.018.

- [68] C. Cheng, S. Du, and J. Yan, "Review on the preparation and modified technologies of microencapsulated red phosphorus Review on the Preparation and Modified Technologies of," *2nd Int. Conf. Mater. Sci. Resour. Environ. Eng. (MSREE 2017)*, pp. 1–6, **2017**.
- [69] A. K. Nayak, "Hydroxyapatite Synthesis Methodologies : An Overview," *Int. J. ChemTech Res.*, vol. 2, no. 2, pp. 903–907, **2010**.
- [70] Q. Dong *et al.*, "Thermal Properties and Flame Retardancy of Polycarbonate / Hydroxyapatite Nanocomposite," *J. Appl. Polym. Sci.*, vol. 109, pp. 659–663, **2008**, doi: 10.1002/app.
- [71] A. Yasemin, "Improvement Of Mechanical And Flame Retardancy," **2015**.
- [72] Y. Kim and S. Lee, "Fire-Safe Polymer Composites : Flame-Retardant Effect of Nanofillers," *Polymers (Basel)*., vol. 13, no. 540, **2021**.
- [73] ASTM D3801, "Standard Test Method for Measuring the Comparative Burning Characteristics of Solid Plastics in a Vertical Position".
- [74] D. Allan, J. H. Daly, and J. J. Liggat, "Oxidative and non-oxidative degradation of a TDI-based polyurethane foam: Volatile product and condensed phase characterisation by FTIR and solid state ¹³C NMR spectroscopy," *Polym. Degrad. Stab.*, vol. 161, pp. 57–73, **2019**, doi: 10.1016/j.polymdegradstab.2018.12.027.
- [75] S. Murat Unlu, U. Tayfun, B. Yildirim, and M. Dogan, "Effect of boron compounds on fire protection properties of epoxy based intumescent coating," *Fire Mater.*, vol. 41, no. 1, pp. 17–28, **2017**, doi: 10.1002/fam.2360.
- [76] Wilkie Charles A., *Fire Retardancy of Polymeric Materials*, Second. CRC Press, **2009**.
- [77] M. Alexander and M. Klatt, "Nitrogen-Based Flame Retardants," in *Non-Halogenated Flame Retardant Handbook*, **2022**, pp. 240–250.

- [78] Y. Aydogan, L. Atabek Savas, A. Erdem, F. Hacıoglu, and M. Dogan, “Performance evaluation of various phosphorus compounds on the flammability properties of short carbon fiber-reinforced polyamide 6 composites,” *Fire Mater.*, no. April 2022, pp. 837–847, **2022**, doi: 10.1002/fam.3126.
- [79] A. B. Morgan, *Non-Halogenated Flame Retardant Handbook*, Second. Wiley, **2022**.
- [80] L. F. Souza *et al.*, “Dosimetric properties of $\text{MgB}_4\text{O}_7:\text{Dy,Li}$ and $\text{MgB}_4\text{O}_7:\text{Ce,Li}$ for optically stimulated luminescence applications,” *Radiat. Meas. J.*, vol. 106, pp. 196–199, **2017**.
- [81] V. Zheltova *et al.*, “ $\text{Fe}_3\text{O}_4@\text{HAp}$ core–shell nanoparticles as MRI contrast agent: Synthesis, characterization and theoretical and experimental study of shell impact on magnetic properties,” *Appl. Surf. Sci.*, vol. 531, no. July, p. 147352, **2020**, doi: 10.1016/j.apsusc.2020.147352.
- [82] M. Murugesan, “Nano-hydroxyapatite (HAp) and hydroxyapatite/platinum (HAp/Pt) core shell nanorods: Development, structural study, and their catalytic activity,” *Can. J. Chem. Eng.*, vol. 99, pp. 268–280, **2020**.
- [83] M. Neumeier, L. A. Hails, S. A. Davis, S. Mann, and M. Epple, “Synthesis of fluorescent core-shell hydroxyapatite nanoparticles,” *J. Mater. Chem.*, vol. 21, no. 4, pp. 1250–1254, **2011**, doi: 10.1039/c0jm02264k.
- [84] W. Pon-On, S. Meejoo, and I. M. Tang, “Substitution of manganese and iron into hydroxyapatite: Core/shell nanoparticles,” *Materials Research Bulletin*, vol. 43, no. 8–9, pp. 2137–2144, **2008**. doi: 10.1016/j.materresbull.2007.09.004.
- [85] S. İflazoğlu, A. Yılmaz, V. E. Kafadar, M. Topaksu, and A. N. Yazıcı, “Neutron+Gamma response of undoped and Dy doped MgB_4O_7 thermoluminescence dosimeter,” *Appl. Radiat. Isot.*, vol. 147, no. October **2018**, pp. 91–98, 2019, doi: 10.1016/j.apradiso.2019.02.014.

- [86] H. Wang, Y. Yuan, M. Rong, and M. Zhang, "Microencapsulation of styrene with melamine-formaldehyde resin," *Colloid Polym. Sci.*, vol. 287, no. 9, pp. 1089–1097, **2009**, doi: 10.1007/s00396-009-2072-6.
- [87] K. Wu, L. Song, Z. Wang, and Y. Hu, "Preparation and characterization of double shell microencapsulated ammonium polyphosphate and its flame retardance in polypropylene," *J. Polym. Res.*, vol. 16, no. 3, pp. 283–294, **2009**, doi: 10.1007/s10965-008-9228-9.
- [88] A. R. Doieh Ali, Pour Mohammed Farajollah, Movahed Sogand Ghafari, Pizzi Antonio, Selakjani Peyman Pouresmaeel, Kiamahalleh Mohammed Valizadeh, Hatefnia Hamid, Shahavi Mohammed Hassan, "A review of recent progree in melamine-formaldehyde resin based nanocomposites as coating materials," *Prog. Org. Coatings*, vol. 165, no. 106768, pp. 1–16, **2022**.
- [89] J. Xu, H. Yang, Z. Luo, D. Wu, and G. Cao, "Synergistic effects of core@double-shell structured magnesium hydroxide microcapsules on flame retardancy and smoke suppression in flexible poly(vinyl chloride)," *RSC Adv.*, vol. 12, no. 5, pp. 2914–2927, **2022**, doi: 10.1039/d1ra09030e.
- [90] H. G. Hammon, "A Mixing Procedure for Adiprene L-315/Polyol Adhesive," **1973**.
- [91] G. Montes-hernandez, "Nucleation of Brushite and Hydroxyapatite from Amorphous Calcium Phosphate Phases Revealed by Dynamic In Situ Raman Spectroscopy," **2020**, doi: 10.1021/acs.jpcc.0c04028.
- [92] N. Goel, N. Sinha, and B. Kumar, "Growth and properties of sodium tetraborate decahydrate single crystals," *Mater. Res. Bull.*, vol. 48, no. 4, pp. 1632–1636, **2013**, doi: 10.1016/j.materresbull.2013.01.007.
- [93] J. Chen, M. Jiang, J. Han, K. Liu, M. Liu, and Q. Wu, "Syntheses of magnetic GO @ melamine formaldehyde resin for dyes adsorption," *Mater. Res. Express*, vol. 6, no. 8, **2019**, doi: 10.1088/2053-1591/ab1ba6.

- [94] D. N. S. Luiza Freire de Souzaa, Linda V.E. Caldasb, Danilo O. Junota, Anderson M.B. Silvaa, “Thermal and structural properties of magnesium tetraborate produced by solid state synthesis and precipitation for use in thermoluminescent dosimetry,” *Radiat. Phys. Chem. J.*, p. 164, **2019**.
- [95] İ. Uysal, B. Yılmaz, and Z. Evis, “Boron doped hydroxyapatites in biomedical applications,” *J. Boron*, vol. 5, no. 4, pp. 199–208, **2020**, doi: 10.30728/boron.734804.
- [96] S. B. Leskovsek Mirjam, Kortnik Joze, Elesini Urska Stankovic, “Characterisation of melamine formaldehyde microspheres synthesised with prolonged microencapsulated reaction time,” *J. Poymer Enginerring*, vol. 42, no. 4, pp. 288–297, **2022**.
- [97] S. Ullah, M. A. Bustam, M. Nadeem, M. Y. Naz, W. L. Tan, and A. M. Shariff, “Synthesis and Thermal Degradation Studies of Melamine Formaldehyde Resins,” *Sci. World J.*, vol., **2014**.
- [98] D. J. Merline, S. Vukusic, and A. A. Abdala, “Melamine formaldehyde: Curing studies and reaction mechanism,” *Polym. J.*, vol. 45, no. 4, pp. 413–419, **2013**, doi: 10.1038/pj.2012.162.
- [99] T. R. Manley and D. A. Higgs, “Thermal stability of melamine formaldehyde resins,” *J. Polym. Sci.*, vol. 1382, no. 42, pp. 1377–1382, **1973**.
- [100] L. Krishnan, B. K. Kandola, D. Deli, and J. R. Ebdon, “Thermal Stability , Flammability and Mechanical Performances of Unsaturated Polyester – Melamine Resin Blends and of Glass Fibre-Reinforced Composites Based on Them,” *Polymers (Basel)*., vol. 14, no. 4885, pp. 1–21, **2022**.
- [101] D. Wang, X. Zhang, S. Luo, and S. Li, “Preparation and Property Analysis of Melamine Formaldehyde Foam,” *Advences Mater. Phys. Chem.*, vol. 2, no. December, pp. 63–67, **2012**, doi: 10.4236/ampc.2012.24B018.
- [102] M. M. Ferra, M. Ohlmeyer, M. Mendes, N. Costa, and L. H. Carvalho,

- “International Journal of Adhesion & Adhesives Evaluation of urea-formaldehyde adhesives performance by recently developed mechanical tests,” *Int. J. Adhes. Adhes.*, vol. 31, pp. 127–134, **2011**, doi: 10.1016/j.ijadhadh.2010.11.013.
- [103] Y. Ma, W. Zhang, C. Wang, Y. Xu, S. Li, and F. Chu, “Preparation and characterization of melamine modified urea-formaldehyde foam,” *Int. Polym. Process.*, vol. 28, no. 2, pp. 188–198, **2013**, doi: 10.3139/217.2684.
- [104] F. Luo, K. Wu, H. Zhu, X. Li, and M. Lu, “Intrinsically flame retarded foams based on melamine – formaldehyde condensates: thermal and mechanical properties,” *Polym. Int.*, vol. 66, no. 6, pp. 779–786, **2017**, doi: 10.1002/pi.5314.
- [105] I. Vitkauskiene, R. Makuška, U. Stirna, and U. Cabulis, “Thermal properties of polyurethane-polyisocyanurate foams based on poly(ethylene terephthalate) waste,” *Mater. Sci.*, vol. 17, no. 3, pp. 249–253, **2011**, doi: 10.5755/j01.ms.17.3.588.
- [106] M. Maminski, W. Jaskolowski, and P. Parzuchowski, “Thermal stability of novel polyurethane adhesives investigated by TGA,” *Mediterr. J. Chem.*, vol. 3, no. 3, pp. 877–882, **2014**, doi: 10.13171/mjc.3.3.2014.17.05.13.
- [107] E. Dominguez-Rosado, J. J. Liggat, C. E. Snape, B. Eling, and J. Pichtel, “Thermal degradation of urethane modified polyisocyanurate foams based on aliphatic and aromatic polyester polyol,” *Polym. Degrad. Stab.*, vol. 78, no. 1, pp. 1–5, **2002**, doi: 10.1016/S0141-3910(02)00086-1.
- [108] E. Govorčin Bajsic and V. Rek, “Thermal stability of polyurethane elastomers before and after UV irradiation,” *J. Appl. Polym. Sci.*, vol. 79, no. 5, pp. 864–873, **2001**, doi: 10.1002/1097-4628(20010131)79:5<864::AID-APP110>3.0.CO;2-D.
- [109] R. Becker, P. Scholz, C. Jung, and S. Weidner, “Thermal desorption gas chromatography-mass spectrometry for investigating the thermal degradation

- of polyurethanes,” *Anal. Methods*, pp. 1979–1984, **2023**, doi: 10.1039/d3ay00173c.
- [110] Y. Liu, M. F. Liu, D. Xie, and Q. Wang, “Thermoplastic polyurethane-encapsulated melamine phosphate flame retardant polyoxymethylene,” *Polym. - Plast. Technol. Eng.*, vol. 47, no. 3, pp. 330–334, **2008**, doi: 10.1080/03602550701870099.
- [111] H. H. G. Jellinek and K. Takada, “Toxic Gas Evolution From Polymers: Evolution of Hydrogen Cyanide From Polyurethanes,” *J Polym Sci Polym Chem Ed*, vol. 15, no. 9, pp. 2269–2288, **1977**, doi: 10.1002/pol.1977.170150917.
- [112] D. Rosu, N. Tudorachi, and L. Rosu, “Investigations on the thermal stability of a MDI based polyurethane elastomer,” *J. Anal. Appl. Pyrolysis*, vol. 89, no. 2, pp. 152–158, **2010**, doi: 10.1016/j.jaap.2010.07.004.
- [113] X. Chen, L. Huo, C. Jiao, and S. Li, “Journal of Analytical and Applied Pyrolysis TG – FTIR characterization of volatile compounds from flame retardant polyurethane foams materials,” *J. Anal. Appl. Pyrolysis*, vol. 100, pp. 186–191, **2013**, doi: 10.1016/j.jaap.2012.12.017.
- [114] Y. Jiang, M. Jiang, P. Liu, and J. Xu, “Flame retardant study of formalized polyvinyl alcohol fiber coated with melamine formaldehyde resins and synergistic effect of copper ions,” *Polym. Degrad. Stab.*, vol. 144, pp. 331–343, **2017**.
- [115] M. Dogan and E. Bayramlı, “Effect of Boron Phosphate on the Mechanical , Thermal and Fire Retardant Properties of Polypropylene and Polyamide-6 Fibers,” *fires Polym.*, vol. 14, no. 10, pp. 1595–1601, **2013**, doi: 10.1007/s12221-013-1595-0.
- [116] N. Wu, Z. Xiu, and J. Du, “Preparation of microencapsulated aluminum hypophosphite and flame retardancy and mechanical properties of flame-retardant ABS composites,” *J. Appl. Polym. Sci.*, vol. 134, no. 33, pp. 1–14,

2017, doi: 10.1002/app.45008.

- [117] M. M. Velencoso, M. J. Ramos, R. Klein, A. De Lucas, and J. F. Rodriguez, “Thermal degradation and fire behaviour of novel polyurethanes based on phosphate polyols,” *Polym. Degrad. Stab.*, vol. 101, no. 1, pp. 40–51, **2014**, doi: 10.1016/j.polymdegradstab.2014.01.012.
- [118] A. Bayu, D. Nandiyanto, R. Oktiani, and R. Ragadhita, “Indonesian Journal of Science & Technology How to Read and Interpret FTIR Spectroscopy of Organic Material,” no. 1, pp. 97–118, **2019**.
- [119] P. Kiliaris, “Polymers on Fire,” in *Polymer Green Flame Retardants*, **2014**, pp. 29–30.
- [120] P. Hornsby, “Fire-Retardant Fillers,” in *Fire Retardancy of Polymeric Materials*, **2009**, pp. 165–168.
- [121] J. Li, “Recent advances in metal family flame retardants: a review,” *R. Soc. Chem.*, vol. 13, **2023**.
- [122] J.-M. Lopez-Cuesta and F. Laoutid, “Multicomponent FR Systems: Polymer Nanocomposites Combined with Additional Materials,” in *Fire Retardancy of Polymeric Materials*, **2009**, pp. 303–305.

APPENDICES

A. Flame Retardancy Performance of HAp-PU Composite

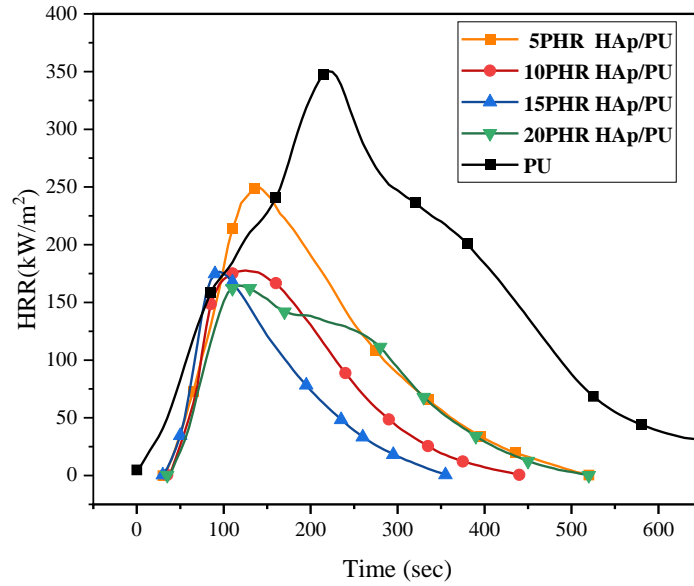


Figure A. 1. HRR Curves of HAp-PU composites.

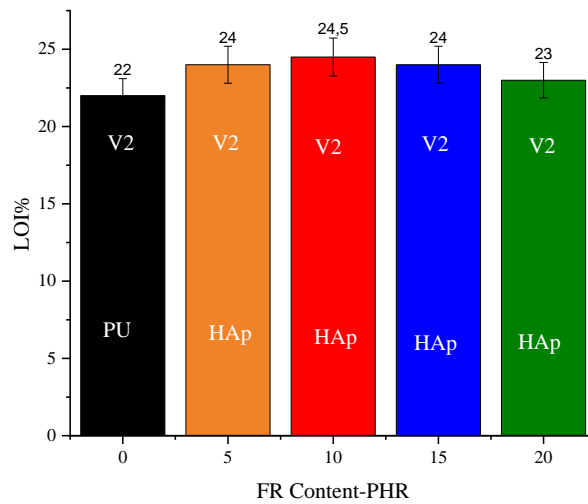


Figure A. 2. LOI% and UL-94 rating of HAp-PU composites.

B. Flame Retardancy Performance of B-HAp-PU Composites

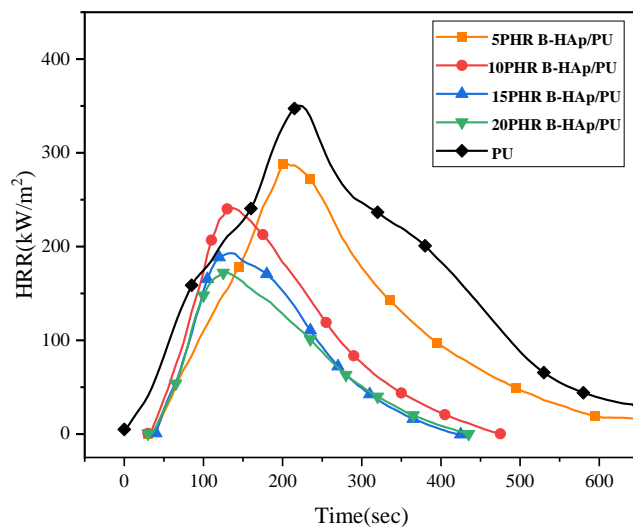


Figure B. 1 HRR Curves of Boron doped-HAp-PU composites.

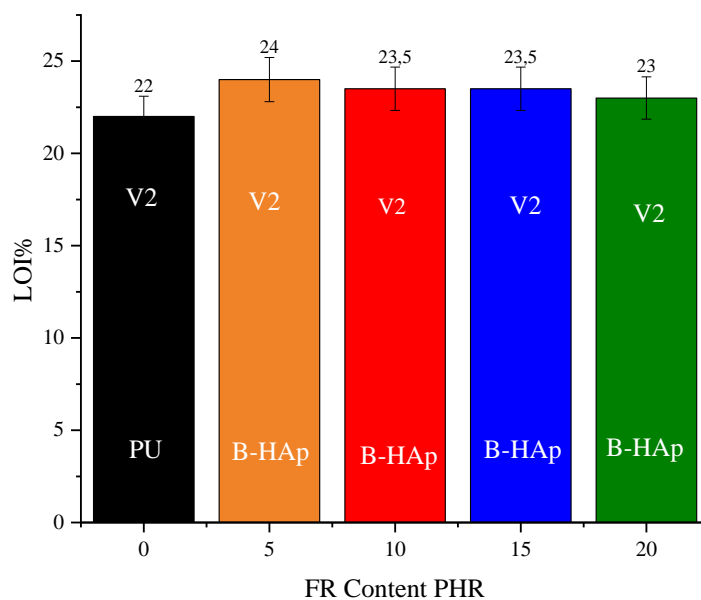


Figure B. 2. LOI% and UL-94 rating of Boron doped-HAp-PU composites.

C. Flame Retardancy Performance of MTB-MF1:1-PU Composites

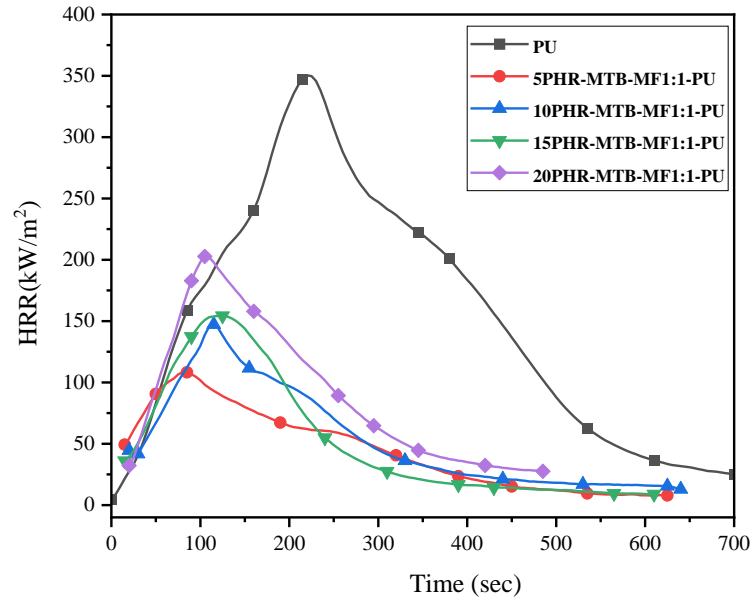


Figure C. 1. HRR Curves of MTB-MF1:1-PU composites.

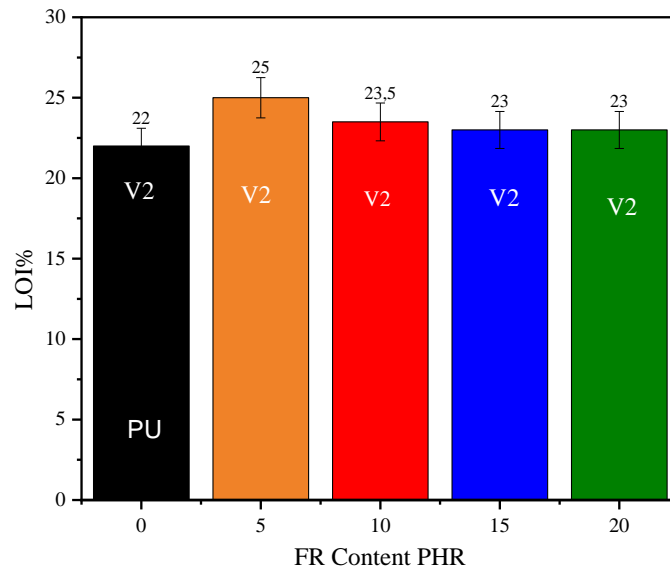


Figure C. 2. LOI% and UL-94 rating of MTB-MF1:1-PU composites.

D. Flame Retardancy Performance of MTB-MF1:3-PU Composites

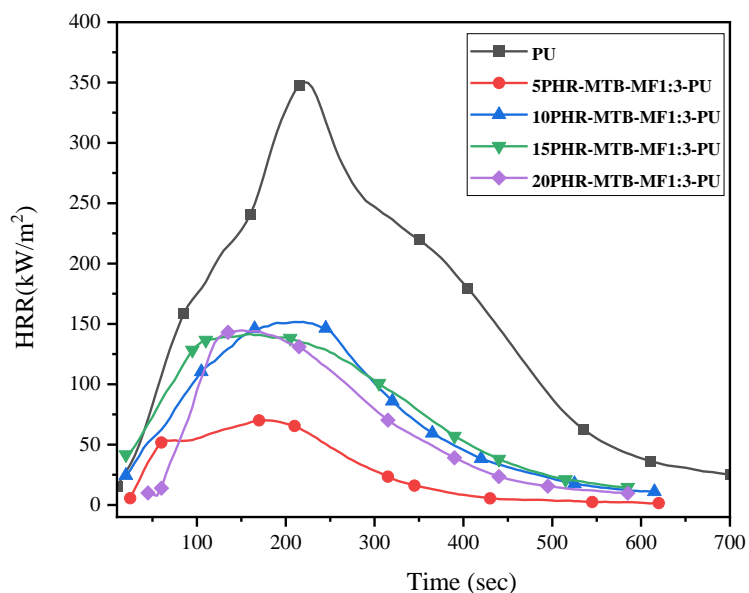


Figure D. 1. HRR Curves of MTB-MF1:3-PU composites.

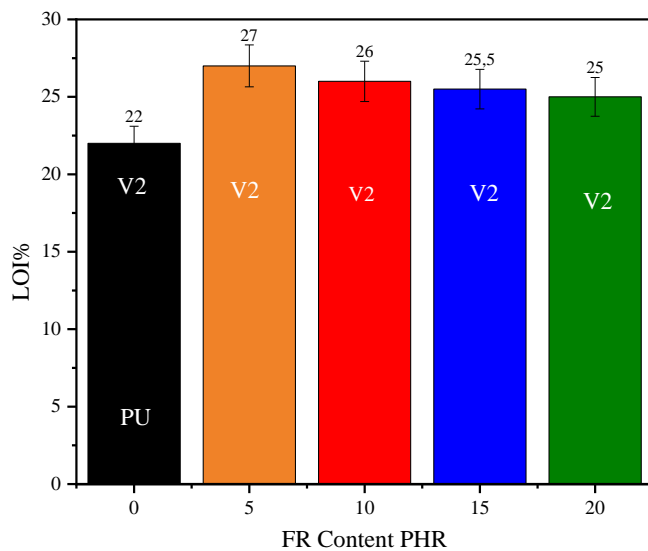


Figure D. 2. LOI% and UL-94 rating of MTB-MF1:3-PU composites.

E. Flame Retardancy Performance of MTB@HAp-MF1:1-PU Composites

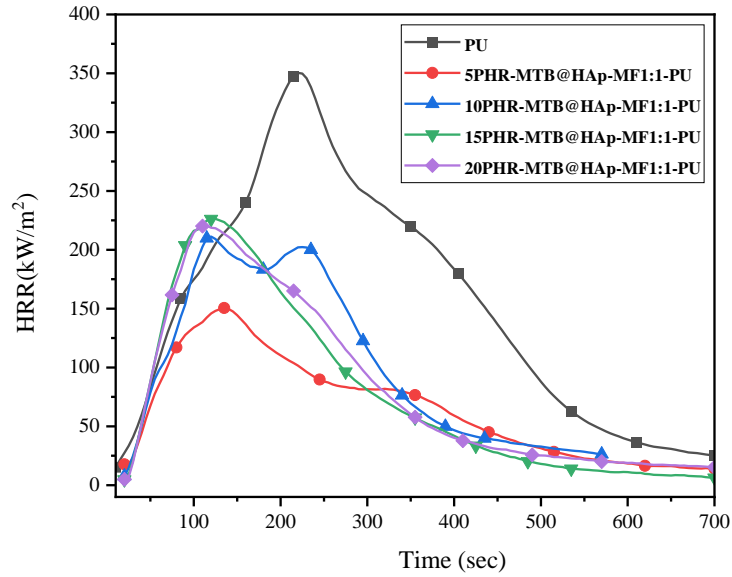


Figure E. 1. HRR Curves of MTB@HAp-MF1:1-PU composites.

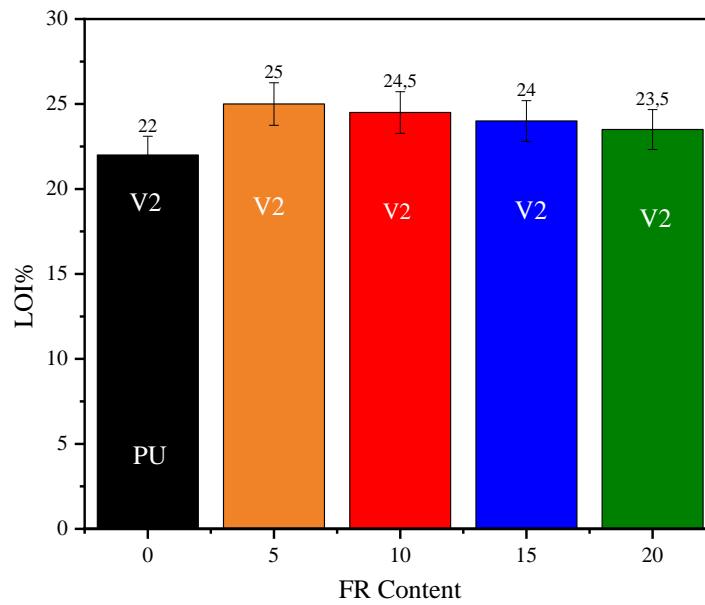


Figure E. 2. LOI% and UL-94 rating of MTB@HAp-MF1:1-PU composites.

F. Flame Retardancy Performance of MTB@HAp-MF1:3-PU Composites

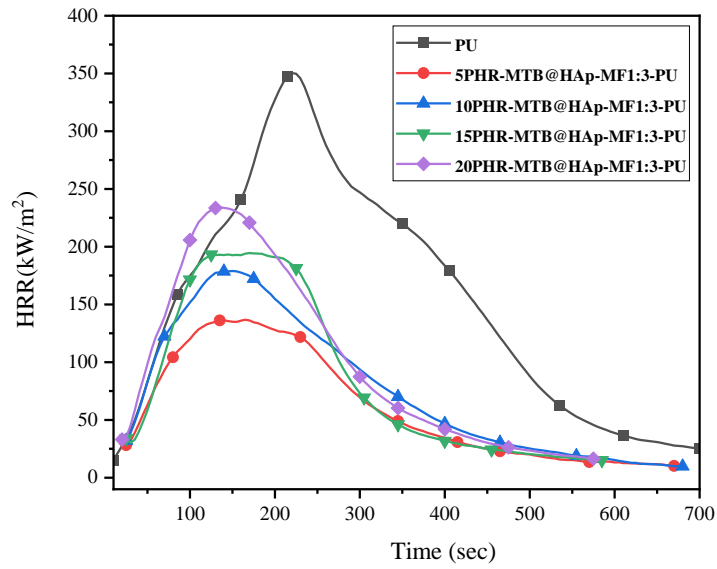


Figure F. 1. HRR Curves of MTB@HAp-MF1:3-PU composites.

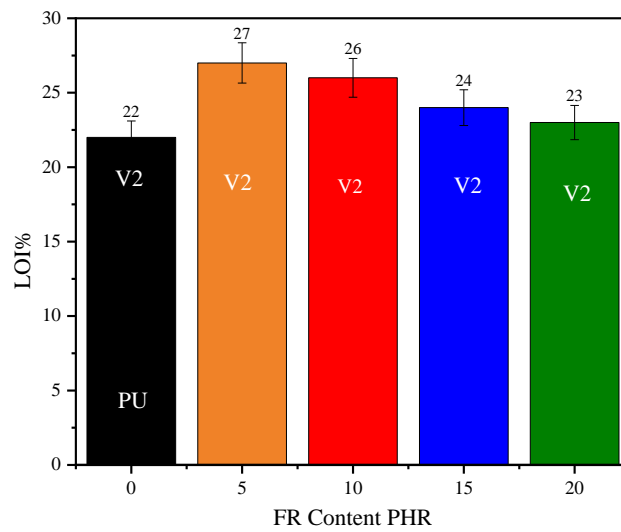


Figure F. 2. LOI% and UL-94 rating of MTB@HAp-MF1:3-PU composites.

CURRICULUM VITAE

Surname, Name: Çelik, Muzaffer Gençay
Nationality: Turkish (TC)
Date and Place of Birth: 16 September 1987, Elazığ
Marital Status: Married
Phone:
email:

EDUCATION

Degree	Institution	Year of Graduation
MS	METU Chemistry	2016
BS	METU Chemistry	2013
High School	Balagazi High School, Elazığ	2004

WORK EXPERIENCE

Year	Place	Enrollment
2019-Present	Roketsan Missiles Inc.	Engineer
2016-2019	METU Dept. of Chemistry	Research Assistant

FOREIGN LANGUAGES

Advanced English

PUBLICATIONS

M.G.Celik, A. Yilmaz, and A. N. Yazici, "Synthesis and thermoluminescence characterization of lithium tetraborate ($\text{Li}_2\text{B}_4\text{O}_7$) doped with copper and silver metals," *Radiat. Meas.*, vol. 102, pp. 16–26, 2017, doi: 10.1016/j.radmeas.2017.06.002.